A Critical Examination of Seyfert 1 X-ray Spectroscopy

by

Kirsten Bonson

A Dissertation Submitted to Saint Mary's University, Department of Astronomy & Physics
in Partial Fulfillment of the Requirements for the Degree of Doctor of Philosophy in Astronomy
August 2017, Halifax, Nova Scotia

Approved: Dr. Luigi Gallo
Supervisor

Approved: Dr. Robert Thacker
Examiner

Approved: Dr. Philip Bennett
Examiner

Approved: Dr. Dirk Grupe
External Examiner

Date: August 8^{th}, 2017

"Because it's there."

$\sim$ George Mallory 1923

Acknowledgements

This work would not have been possible without the support of my family, in Vermont and elsewhere, who tolerated my working vacations most of the time and were able to drag me into the world for some much-needed sunshine for the other. Big thanks to Al especially for keeping me going with a steady stream of unsolicited joke drafts for the last year or so. I will always remain eternally grateful for the love and strength of my partner, Jillian, who happened to stumble into the midst of this and yet saw it through with me to the end – I would not have finished without her. Much thanks must be given to my fellow astro-clan and officemates for all the adventures, dog-related and otherwise, we've had these last six years. Finally, I must thank my supervisor Luigi for putting his faith in me years ago in agreeing to embark on this journey and never once rescinding his offer, as tempting as it might have been.

Contents

List of Figures

List of Tables

Abstract

A Critical Examination of Seyfert 1 X-ray Spectroscopy

by Kirsten Bonson

The field of high-energy AGN astrophysics is about to be transformed as data of unprecedented quality and quantity will be arriving from the next-generation of X-ray observatories. With the advancement of technology, we must remain critical of our methodologies to ensure the limits of particular techniques are well-defined. For example, the spin of supermassive black holes is of great interest for understanding the physics of accretion and black hole-host galaxy co-evolution. However, consistency and reproducibility of spin constraints have been a challenge even when the observable bandpass is increased with the launch of *NuStar*. We therefore begin by systematically evaluating the ability of X-ray modelling methods to measure known reflection parameters, like black hole spin, under standard conditions often seen in the literature. We created and fit over 4000 simulated Seyfert 1 spectra each with 375,000$\pm$1,000 counts and assessed the success of fits for a range of fixed parameters, reflection fractions, and bandpasses. We discover that most parameters are over-estimated when spectroscopy is restricted to the 2.5 – 10.0 keV regime and that models are insensitive to ionization unless the bandpass is extended. In all cases, we find the spin parameter is only well measured for the most rapidly rotating supermassive black holes (i.e. $a > 0.8$ to about $\pm$0.10). With this knowledge in-hand, we next turned to empirical data by examining the complex short-term X-ray variability of narrow-line Seyfert 1 galaxy Mrk 493 in depth. We first utilized model-independent techniques such as timing studies and PCA as a way to guide the detailed spectroscopy. We were able to isolate two distinct periods in which the spectral variability of Mrk 493 shifts from one dominated by changes in the primary component to one dominated by changes in disk ionization. In addition, both spectroscopic analysis and model-independent tests point to an additional source of variability that is unaccounted for. Different scenarios including spallation, disk hot spot, and hot annulus are tested and discussed.

August 8, 2017

Chapter 1

Introduction

1.1 A History

Planted firmly at the intersection between the regimes ruled by Quantum Mechanics and General Relativity, black holes are both exotic and scientifically valuable but no longer considered a science-fiction fantasy. In fact, we now know that the most massive black holes ($> 10^5 M_\odot$) are essentially classical objects depending on the scales involved. Since their existence was first proposed by John Michell in 1783 (Murdin, 2000), mathematical theory has been confirmed with observations (e.g. Bolton, 1972; Harms et al., 1994; Broderick et al., 2009; Abbott et al., 2016) and detailed, multi-wavelength analyses are advancing our understanding of these objects at a rapid pace. Black holes challenge current laws of physics by being extremely massive ($\sim$3 – $10^{10} M_\odot$) while existing on Planck scale (1.6×10^{-35} m) and they can influence their surroundings on extragalactic scales (e.g. Fabian, 2012; Kormendy and Ho, 2013; Harrison et al., 2014). Their mere existence offers valuable insight to the evolution of stars (e.g. Belczynski et al., 2012; Chatterjee et al., 2016), galaxies (e.g. Ho et al., 1997; Reines et al., 2013; Werner et al., 2013), galaxy clusters (e.g. Ruszkowski et al., 2003; Dunn and Fabian, 2006; McNamara and Nulsen, 2007), and the Universe as a whole (e.g. Rovelli and Vidotto, 2014; Shapiro, 2004; Schaye et al., 2014; Dubois et al., 2014). Indeed, black holes are an integral part of the cosmos.

Figure 1.1: Radio galaxy Hercules A is an example of the kpc-scale jets indicating an AGN at the host galaxy's centre. Credit: NASA, ESA, S. Baum & C. O'Dea (RIT), R. Perley & W. Cotton (NRAO/AUI/NSF), and the Hubble Heritage Team (STScI/AURA).

Active supermassive black holes are the largest members of the black hole family to be observed at $\gtrsim 10^6 M_\odot$. Known as Active Galactic Nuclei (AGN), these objects reside at the centres of galaxies and can be seen when accreting the material around them. The most obvious signature of an AGN comes in the form of giant radio jets that can stretch far beyond the galactic central engine (Fig. 1.1), although one of the defining characteristics of these objects is their strong ($\gtrsim 10^{40}\,\mathrm{erg\,s^{-1}}$) bolometric luminosity that spans from the radio all the way up to gamma frequencies (Elvis et al., 1994). Rather conveniently for observers, different structures of the AGN anatomy can emit at different wavelengths and so one can select a particular band in which to study AGN in order to focus on an area of interest. Material closest to the central supermassive black hole radiates at the highest energies due to the extreme forces involved and thus, by observing in the high-energy regime, we are able to probe the AGN central engine itself (Fig. 1.2).

X-ray astronomy began with the launch of proportional counters on sounding rockets (see

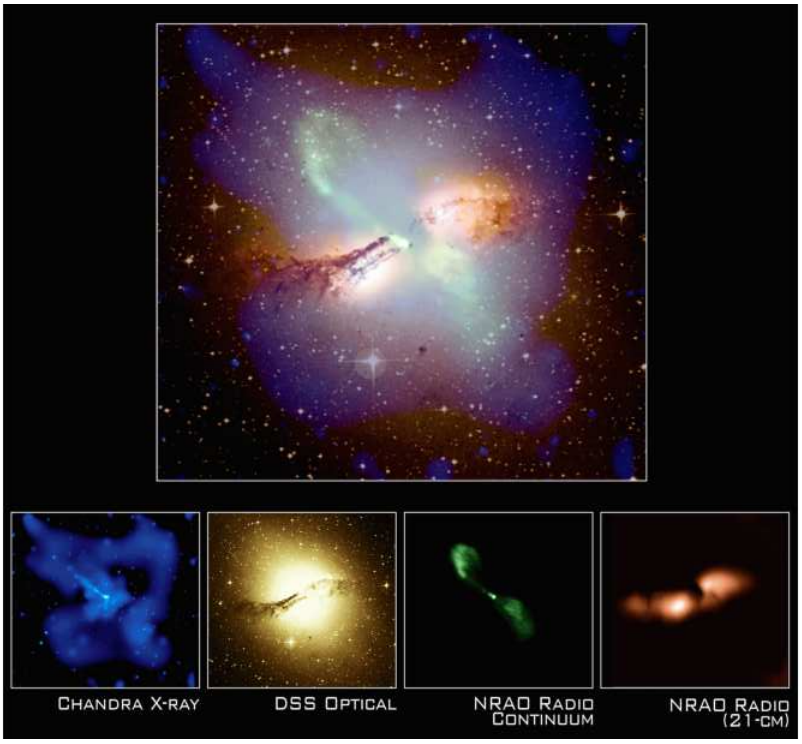

Figure 1.2: Centaurus A is shown as both a composite image (Top) and the image's multi-band components (Bottom). The image composits consist of X-ray (blue), optical (yellow), continuum radio (green), and 21-cm radio (orange) features. Credit: X-ray (NASA/CXC/M. Karovska et al.); Radio 21-cm image (NRAO/VLA/J.Van Gorkom/Schminovich et al.), Radio continuum image (NRAO/VLA/J. Condon et al.); Optical (Digitized Sky Survey U.K. Schmidt Image/STScI).

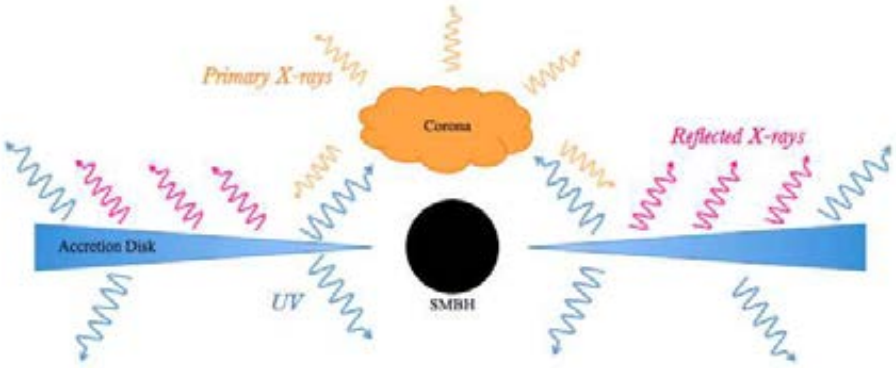

Figure 1.3: Illustration of the three main bodies comprising the region closest to the supermassive black hole: the black hole (black), its surrounding accretion disk (blue), and a corona (yellow). This schematic shows a lamppost geometry of the corona as an example.

Bradt et al., 1992, for review). The rockets were required to carry the X-ray detectors above the shield of Earth's atmosphere. The discovery of Sco X-1, the first persistent X-ray source ever detected outside of the solar system (e.g. Giacconi et al., 1962; Sandage et al., 1966) quickly advanced the field of high-energy astronomy which made further strides with the discovery of the diffuse cosmic X-ray background (from the same rocket observation as that of Sco X-1!) and the discovery of extended X-ray emission in the Crab Nebula (Bowyer et al., 1964). The launch of *Uhuru* (Giacconi et al., 1971), the first X-ray satellite successfully flown into orbit, greatly extended observing time and resulted in the first astronomical X-ray catalog. The field was revolutionized once again with the use of grazing incidence optics (see Giacconi et al., 1969, for review), giving X-ray telescopes imaging capabilities for the first time. The *Einstein* observatory (Giacconi et al., 1979) was the first to launch with the new technology and produced the first spectral surveys of the brightest AGN (Wilkes and Elvis, 1987; Kruper et al., 1990). Today, after a golden era in AGN X-ray astronomy with the longevity of successful missions like *Suzaku*, *Chandra*, and *XMM-Newton*, researchers are breaking new ground with the next generation of observations from *NuStar* (e.g. Risaliti et al., 2013; Zoghbi et al., 2014; Keck et al., 2015; Fabian et al., 2015), *Hitomi* (Hitomi Collaboration, 2017), and in the next decade *ATHENA*.

AGN taxonomy includes a wide variety of active supermassive black hole types, classified in part by their line-of-sight to the observer (e.g. Merloni et al., 2013; Mateos et al., 2016). While individual objects may have more or less complicated geometries, the region closest to the black hole is commonly accepted to contain three main components: the supermassive black hole itself, a surrounding accretion disk, and a corona of hot electrons in some orientation above the two (Fig. 1.3). The exact nature of the corona is still open to speculation; the base of a jet (e.g. Raginski and Laor, 2016; King et al., 2017), extended disk atmosphere (e.g. Done et al., 2012; Rozanska et al., 2015), and transient hot flares due to magnetic reconnection events (e.g. Czerny and Goosmann, 2004) have all been proposed. As technology has advanced and data quality improves it appears likely that the corona may be an evolving combination of all of the above (Wilkins and Gallo, 2015a; Wilkins, 2016; Wilkins et al., 2016). The accretion disk extends as close to the black hole as the innermost stable circular orbit (ISCO), defined as $R_{\rm ISCO}$= 3 $R_{\rm s}$ for non-spinning or Schwarzschild black holes (where $R_{\rm s}$ = $\frac{2GM_{\rm BH}}{c^2}$), and stretches hundreds of $R_{\rm s}$ from there.

Further out, at scales of around 0.1 – 1 pc, is the Broad Line Region (BLR), so named because of the broadened optical emission lines produced due to the fast (thousands $\rm km\,s^{-1}$) rotational motion of the source material. Influenced by both the gravitational well of the central black hole as well as the ionizing radiation from the central engine, the exact size of the BLR has been shown to be directly proportional to AGN luminosity (e.g. Kaspi et al., 2000; Bentz et al., 2013) and the kinematics of this system are useful probes of black hole mass and other properties (e.g. Ho and Kim, 2015; Mejía-Restrepo et al., 2016; Sanfrutos et al., 2016).

Once at $\sim$1pc from the supermassive black hole, a torus of dusty gas can be found encircling the BLR. The torus may be an extension of the accretion disk itself (Elitzur and Shlosman, 2006; Gallimore et al., 2016; Collinson et al., 2017) and plays a key role in the classic Unified Model of AGN by differentiating between Type I and Type II objects: those that are observed close to the plane of the torus are heavily absorbed and are designated Type II. Type I objects are observed along a shallower line-of-sight, between $\sim$0 – 60°, and offer a potentially unobstructed view to the

innermost regions Fig. 1.4.

The last area of the host galaxy observed to be directly influenced by the AGN central engine is the Narrow Line Region (NLR). The NLR is located $\sim$100 – 1000 pc from the central engine and material here is no longer virially bound to the black hole, although it continues to experience radiation pressure and ionization from the central engine continuum. Forbidden lines from the NLR can assist in classifying AGN via emission-line ratios (e.g. Jin et al., 2012; Stern and Laor, 2013; Oh et al., 2017) and potentially strong forbidden lines such as [O III] can be used as a surrogate for stellar velocity dispersion, σ_*, in estimating supermassive black hole mass through the $M_{\rm BH}$- σ_* relationship (e.g. Nelson and Whittle, 1996; Nelson, 2000; Wu, 2009).

As mentioned above, Type I galaxies can offer the ideal orientation for studying regions closest to the supermassive black hole. There are several kinds of AGN that fall into the Type I class, including Seyfert I galaxies (Fig. 1.4). Named for their discoverer Carl Seyfert in 1943 (Seyfert, 1943), Seyfert galaxies were first identified by their abnormally bright nuclear emission and broad optical emission lines which did not resemble those of other "spiral nebulae". Unlike more luminous Type I objects, the host galaxy of Seyfert I AGN can still often be resolved, providing the opportunity to study properties of both a central supermassive black hole along with its host, an opportunity that is key for understanding black hole–host galaxy co-evolution. In addition, Seyfert galaxies usually – but not always (e.g. Yuan et al., 2008; Abdo et al., 2009; Doi et al., 2012; Berton et al., 2016) – lack the kpc-scale jet emission and are deemed 'radio-quiet' (Fig. 1.5) where radio loudness, R, is assessed as $R = \frac{F_{5\,\rm GHz}}{F_{\rm B}}$ and $F_{5\,\rm GHz}$ is the flux density at 5 GHz while $F_{\rm B}$ is the B-band flux density at 4400 Å (Kellermann et al., 1989). Objects with $R > 10$ are considered radio-loud.[1] Thus, the X-ray emission from the innermost regions of Seyfert galaxies will not be washed out by the much more luminous jet.

Narrow-line Seyfert I galaxies (NLS1) are a sub-class of Seyfert galaxies known for their more extreme properties. In general, they possess narrow(er) emission lines from the BLR, have the most

[1] It is important to note that while 'radio-quiet' Seyfert galaxies do not have observable jet structures, they continue to have significant radio emission and it is thought that at least some of these objects may have aborted jet activity (e.g. Ghisellini et al., 2004; Dadina et al., 2005; Giustini et al., 2017).

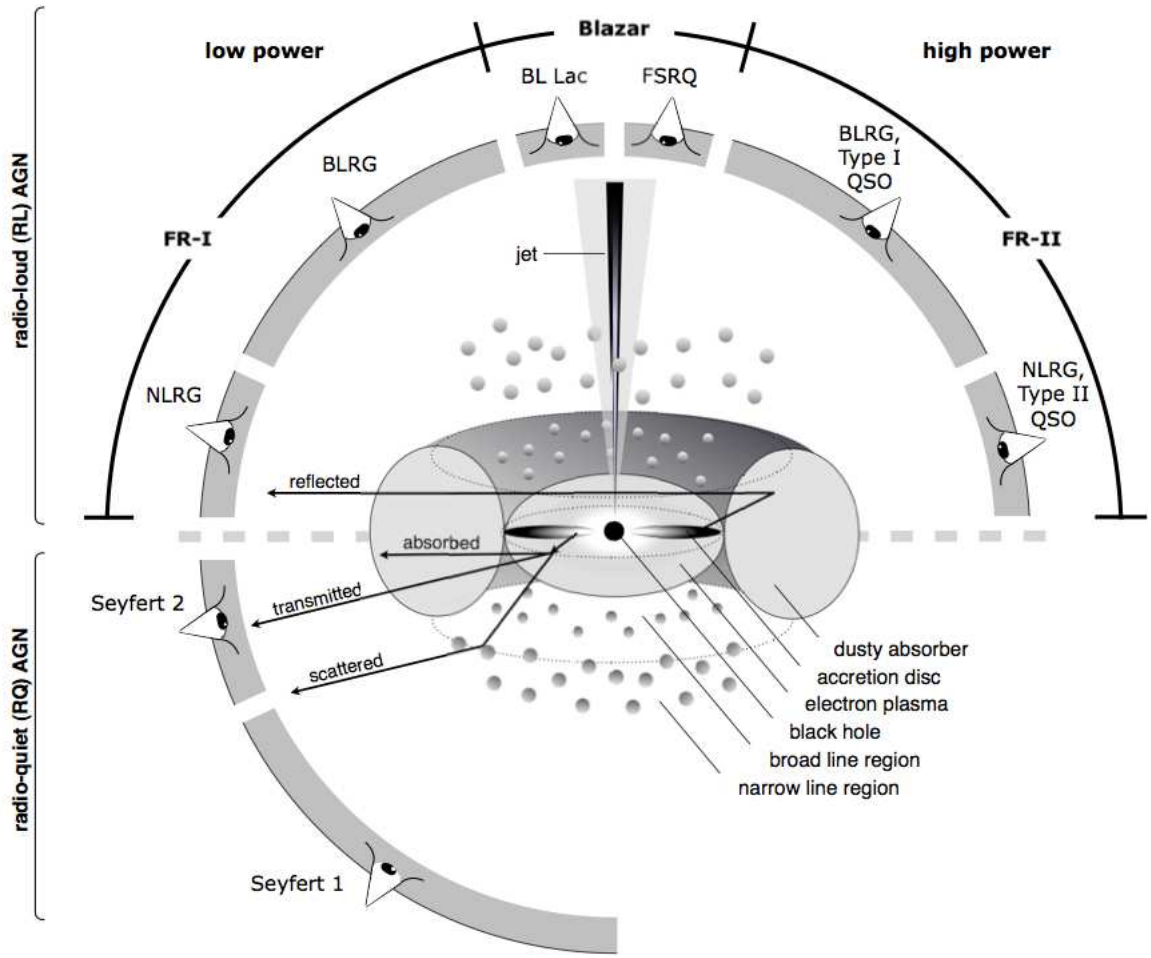

Figure 1.4: Labelled illustration of the geometry of the AGN central engine and how it influences the classical unification model. An example line-of-sight for a Type I Seyfert (i.e. Seyfert 1) galaxy is shown. Credit: Beckmann and Shrader (2012).

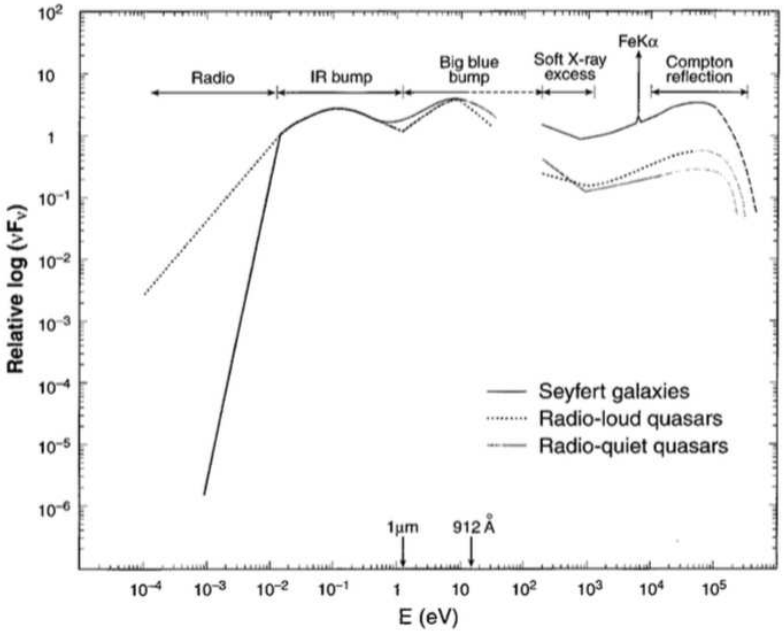

Figure 1.5: Illustration of the broadband spectra of three different Type I classes of AGN. Note that although Seyfert galaxies and radio-quiet quasars are not 'radio-loud' by definition, they do have radio emission. Credit: Koratkar and Blaes (1999).

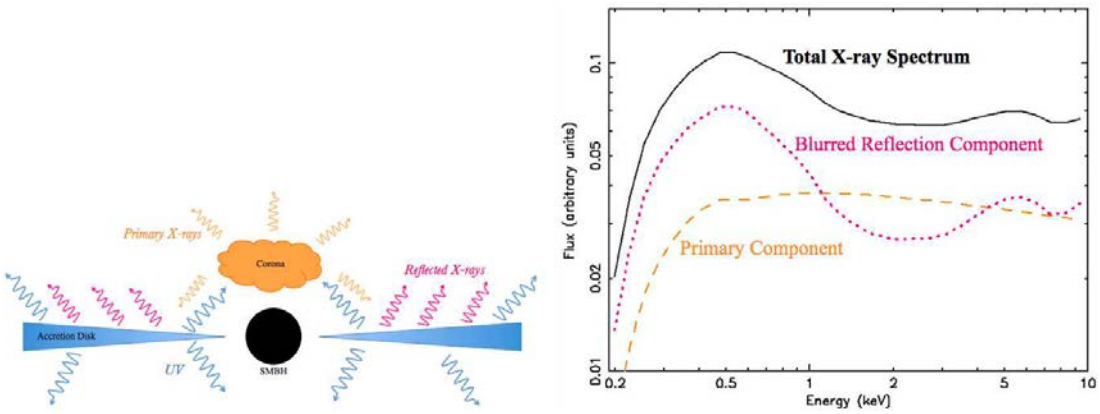

Figure 1.6: The innermost region of the central engine (Left) and the primary X-ray spectral components that originate from it (Right).

rapid (∼hours) short-term X-ray variability, and accrete at high Eddington rates (where $\dot{M}_{\rm Edd}$ = $2.2 \times 10^{-8}(\frac{M_{\rm BH}}{\rm M_\odot})\,{\rm M_\odot\,yr^{-1}}$, assuming greatest efficiency). Observational evidence suggests that NLS1s may be AGN in a particularly young evolutionary state in which supermassive black hole mass is intermediate ($\sim$ 10^6 – $10^7 M_\odot$) and activity is complex (e.g. Grupe, 2004; Mathur et al., 2012; Järvelä et al., 2015; Gallo et al., 2007; Done et al., 2012). The spectra of NLS1s can also be ideally suited for studying regions closest to the supermassive black hole because they tend to have a high amount of reflected emission from the accretion disk.

1.2 AGN X-ray Spectra

The main components of Type I AGN X-ray spectra originate from the black hole accretion disk and corona. While the accretion disk does have its own intrinsic radiation, the temperature of the disk is inversely proportional to black hole mass ($T \propto {\rm M_{BH}}^{-\frac{1}{4}}$) and so for the supermassive black holes imbedded in AGN, disk temperatures result in the intrinsic radiation peaking in the UV as the Big Blue Bump. Unfortunately for AGN astronomers, the UV band is heavily absorbed by Galactic dust and gas and therefore direct observation of the full intrinsic disk spectrum is impossible (Fig. 1.5). However, the accretion disk can be indirectly observed by the isotropic coronal emission, some of which is reprocessed by the disk by combinations of fluorescence, bremsstrahlung, and Compton

scattering. Therefore, the total X-ray spectrum of a Type I galaxy like a NLS1 would appear as the sum of the primary X-ray continuum from the corona and reflected X-ray emission from the disk.

Theoretically, the reflected disk spectrum is distinguishable from the power law continuum by its profile shape: peaking in the softer X-ray bands below $\sim$1 keV, dipping in the intermediate bands around 2 keV, and increasing in flux once again above $\sim$10 keV as Compton scattering dominates forming a 'Compton Hump' peaking $\sim$30 keV (Fig. 1.5). The last decade or so of detailed X-ray spectroscopy has been dominated by observations between 0.3 – 10 keV, above galactic absorption and below the high-energy turnover (Fig. 1.6). This bandpass was ideal for analyzing the primary X-ray continuum (Fig. 1.6, dashed yellow line) and potential blurred reflection from the accretion disk (Fig. 1.6, dotted pink line) while maintaining optimum performance of the instruments. While the 0.3 – 10 keV regime does not include the Compton Hump, it does include X-ray atomic transition energies which play an important role at characterizing AGN spectra.

Intrinsic atomic features such as an emission line peak at their respective transition energies and have negligible width (Fig. 1.7, Top, black). However, an emission source located on a rotating accretion disk will have an emission line with a double-peaked profile as the Doppler effect blueshifts emission heading towards the observer and redshifts that moving away (Fig. 1.7, Left, green). If that same emission source were then moved closer to the central black hole, special relativistic effects would further shift the line peaks away from the central energy while also boosting/reducing the blue/red peak of the line due to relativistic beaming (Fig. 1.7, Top, red). Finally, an emission source located at regions of the disk closest to the central black hole would also experience general relativistic effects, smearing the double-peaked profile further and reducing the overall line flux as the light loses energy climbing out of the black hole's gravitational potential well (Fig. 1.7, Top, blue). Atomic features in an accretion disk reflection spectrum will also experience thermal broadening which increases as ionization increases (Fig. 1.7, Bottom).

Due to both the strength and number of atomic disk features below 1 keV, individual features are smoothed out and the blurred reflection spectrum appears in the soft band as a continuous excess of flux compared to the continuum. This soft-excess is ubiquitous in Type I AGN and appears to

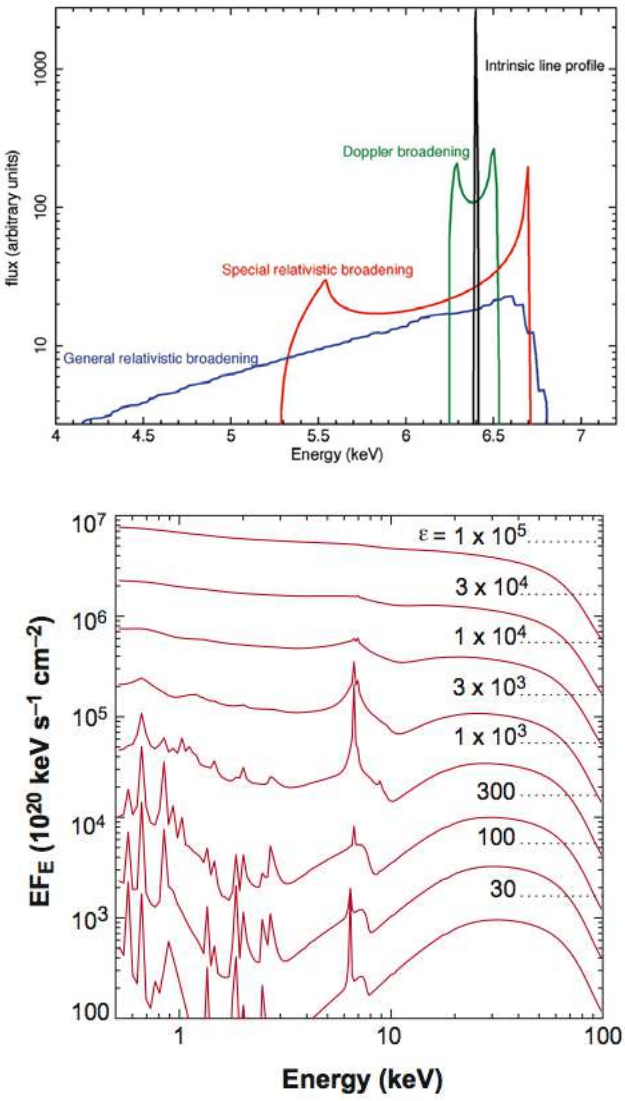

Figure 1.7: Top: illustration of the combined effects that act to blur an intrinsic Fe Kα line (black) as the source moves closer to the central black hole. Doppler broadening (green) produces a double-peaked line, special relativistic broadening (red) widens the double-peaked profile and creates asymmetry, and general relativistic broadening (blue) broadens the line further and reduces flux. Credit: Gallo (2011). Bottom: the simulated effects of disk ionization on the blurred reflection spectrum of an accretion disk. Credit: Miller (2007).

be especially strong in NLS1s (Gondoin et al., 2002, and references therein). Illumination of the accretion disk by an ionizing source also produces significant Fe Kα emission, owing to the high cosmic abundance and fluorescent yield of iron. Unlike the features that make up the soft-excess, a broadened Fe Kα line can be resolved and well-constrained when the source is strong. This is important, as the Fe Kα line can act as a probe of the innermost regions of the accretion disk by measuring disk inclination angle and supermassive black hole spin.

The spin of the black hole is defined by a dimensionless spin parameter as $a = \frac{Jc}{GM_{\rm BH}^2}$ where J is angular momentum, c is the speed of light, G is the gravitational constant, and $M_{\rm BH}$ is the mass of the black hole. Black hole spin in a Kerr or spinning black hole can be constrained by the Fe Kα line by accurately modelling the broadened line profile, as described above and shown in Fig. 1.7. As the spin of a black hole increases, the spacetime around it becomes increasingly warped into an ergosphere or a region of spacetime that spins along with the black hole. The effect of dragging the spacetime into rotation, called frame dragging, results in the ISCO being pulled in to closer radii than it would have been in the classical (i.e. Schwarzschild) scenario – nearly $5\times$ as close to be specific: $R_{\rm ISCO}$= 1.25$R_{\rm g}$ for maximally-spinning black holes where $R_{\rm g}$ = 1/2 $R_{\rm s}$ (Fig. 1.8, Left). If a black hole spin is retrograde or opposite that of the disk, the ISCO can be pushed out to further distances (Fig. 1.8, Right). As the Fe Kα line profile shape is dependent upon the radius of the source from the black hole, we can estimate black hole spin assuming the broadest component of the Fe Kα line is in fact originating from the ISCO. Black hole spin will be discussed in greater detail in Chapter 2.

1.3 Methodology

1.3.1 Dawn of a New Era

To keep progressing, science must be ever-evolving: consistently pushing the envelope of possibility through the balance of theory and observation. High-energy astronomers today are fortunate to be on the cusp of another leap in observational technology brought about through the advent of new

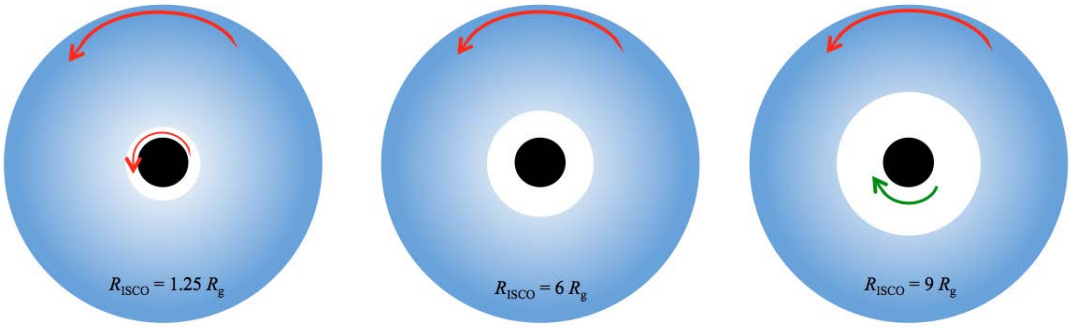

Figure 1.8: Illustration of how black hole spin affects the location of the ISCO for a maximum prograde (Left), non- (Middle), and maximum retrograde (Right) spinning black hole in units of R_g. Gravitational radii are not shown to scale.

optics and detectors. Several missions have led the way, each offering their own unique advantages over past systems.

The Nuclear Spectroscopic Telescope Array (*NuStar*) satellite is a collaboration between Caltech, National Aeronautics and Space Administration (NASA), and NASA's Jet Propulsion Laboratory (JPL) and was launched into a low-Earth orbit on 13 June 2012 employing the first high-energy observatory with a fully-extendable boom (Harrison et al., 2013). The telescope mirrors utilize a modern approach to high-energy optics design, slumped-glass optics: made out of standard commercial glass, the mirrors are melted over quartz moulds to achieve the ideal shape while retaining smoothness. The mirrors are then coated in a multilayer reflective material combining elements suited for reflecting both higher-energy radiation (such as silicon and carbon) and those for lower-energy radiation (such as tungsten and platinum), allowing *NuStar* to observe between 3 – 79 keV while retaining a resolution of < 1 keV throughout the entire bandwidth. In the context of AGN astrophysics, *NuStar* allows the iron line band and that of the Compton Hump to be observed simultaneously with the same instruments – a feat that had not been possible before *NuStar*.

The *Hitomi* mission is a collaboration of over 70 institutions across Japan, Europe, Canada, and the U.S. led by the Institute of Space and Astronautical Sciences (ISAS) of the Japan Aerospace Exploration Agency (JAXA) (Takahashi et al., 2014). Successfully launched into its low-Earth orbit on 17 February 2016, *Hitomi* carried with it a collection of instruments that allowed it to observe an

unprecedented bandwidth, 0.3 – 600 keV, while also obtaining 0.7 eV resolution in the 0.3 – 10 keV bandpass. The observatory utilized new high-energy detector technology, a CdTe double-sided strip detector (DSSD) for the Hard X-ray Telescope (HXT) and a stacked Si + CdTe Compton camera for the Soft Gamma-ray Detector (SGD), as well as reimagined heritage technology in the form of the microcalorimeter in the Soft X-ray Spectrometer (SXS) – originally flown on *Suzaku*. The *Hitomi* technology had vast potential for AGN science, as atomic features more subtle than the Fe Kα line could potentially be resolved (e.g. Furui et al., 2016; Tombesi, 2016; Reynolds, 2016) and the continuum turnover could be robustly measured. The power of the *Hitomi* science was proven with the first-look observation of the Perseus cluster (Hitomi Collaboration, 2017). Unfortunately, the satellite was lost shortly after and a current joint effort between JAXA and NASA is underway to launch a replacement, which will also serve as technological preparation for the *ATHENA* mission.

The Advanced Telescope for High-Energy Astrophysics (*ATHENA*) observatory began as a merger of the European Space Agency's (ESA) *XEUS* and NASA's *Contellation-X* missions and has a current planned launch date of 2028. Unlike the high-energy missions that came before it, *ATHENA* will be placed at Sun-Earth Lagrange Point 2 (L2) allowing for continuous observing field-of-view and more thermal stability. *ATHENA* will also utilize silicon pore optics for its mirror technology, allowing for good angular resolution ($\sim 5''$ at < 7 keV) across a wide field-of-view ($> 40'$). Onboard will be an X-ray Integral Field Unit (X-IFU) (Barret et al., 2016) containing a microcalorimeter for detailed (~ 2.5 eV at 6 keV) 0.3 – 10 keV imaging spectroscopy as well as a Wide Field Imager (WFI) (Meidinger et al., 2017) with count rate capabilities up to $\sim 10^{-8}$ $\mathrm{erg\,cm^{-2}\,s^{-1}}$ between 2 – 10 keV. The combined power of the X-IFU and WFI will allow observers to alternate between pure spectroscopy (X-IFU), pure timing (WFI), and spectral-timing (X-IFU/WFI combined) modes – ideal for variable and spectrally complex objects like AGN. *ATHENA* also offers a balance of higher soft-end spectral resolution than both *Chandra* and *XMM-Newton* while having a greater spatial resolution than *Hitomi* in the same energy band (Fig. 1.9).

The advent of the next generation of high-energy observatories are ushering in not only an

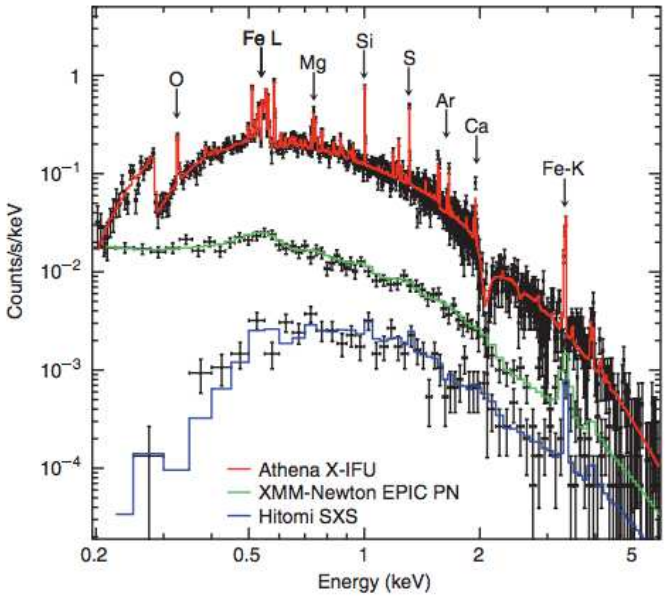

Figure 1.9: A comparison between simulated X-ray spectra of a galaxy group as seen by *XMM-Newton*, *Hitomi*, and *ATHENA* observatories in the same 0.2 – 6 keV band. Credit: Barcons (2017).

unprecedented ability to observe AGN X-ray spectra in greater detail, but also observe them across a much wider band. Researchers will be able to test more complex and physically accurate spectral models, perhaps taking into account details such as disk inhomogeneity, magnetohydrodynamic (MHD) effects, or transient Comptonizing features that were either averaged-out over probable timescales or simply ignored altogether until now. Along with this advancement comes the challenge to be able to handle these new data appropriately and not fall victim to old habits that may skew results before we have even began.

1.3.2 Limits of Classical Approach

While the standard X-ray spectra of Seyfert galaxies appear well-constrained with a simple model (Section 1.2), nature is rarely as obliging. In addition to the components from the accretion disk and corona, AGN spectra can present signatures of absorption as material of various sizes, densities, and temperatures pass along the line-of-sight (Reynolds et al., 1997; Miller et al., 2008; Turner and Miller, 2009). Depending on the scenario, partial covering clouds can preferentially

attenuate the softer X-ray bands: dragging down the primary component so that a soft-excess-like bump below 1 keV appears and scattering emission redward of an Fe Kα line to resemble the red wing of blurred reflection (Fig. 1.10, Right-side illustrations). Signatures of absorption have been identified in well-studied objects like MCG-6-30-15 (e.g. Turner et al., 2004; Miller et al., 2008, 2009) and NGC 1365 (e.g. Parker et al., 2014b; Rivers et al., 2015) and it is likely that absorbing material is common even in Type I sources as the environment surrounding an active supermassive black hole is a violent one. Outflows in the form of disk winds have been observed at near relativistic velocities (e.g. Tombesi et al., 2010; Gofford et al., 2013) and infalling material from the BLR may also be present (e.g. Yaqoob et al., 2003; Giustini et al., 2017). It is common for AGN spectra to be modelled equally well in the 0.3 – 10 keV regime by both a blurred reflection and partial covering absorption scenario.

The degeneracy between the blurred reflection scenario and partial covering absorption may potentially be broken by extending the bandpass observed. As stated previously, AGN are known for having strong bolometric emission and exhibit broadband spectra that can range from the radio band through to gamma-rays (Fig. 1.5). The shape of the X-ray spectrum above the standard observing range of 0.3 – 10 keV is dependent upon the scenario being considered. By extending the observable bandpass to include the Compton Hump and high-energy turnover (Fig. 1.10, Top Right) the true source of emission may be determined using current models, although this is not guaranteed – see the progression of NGC 1365 analysis in Risaliti et al. (2013); Miller and Krolik (2013); Risaliti (2016) for example.

Another challenge high-energy observers must face is constraining key central engine parameters. Black holes are themselves quite simple in their properties, described completely by only their mass and spin[2], therefore much can be derived about the surrounding material through standard X-ray spectral modelling such as disk ionization, line-of-sight inclination, corona opacity or temperature, and more. With the era of *Chandra* and *XMM-Newton*, spectroscopy expanded

[2]In the mathematical paradigm black holes are also described by electromagnetic charge, however those in nature do not appear to require this additional parameter.

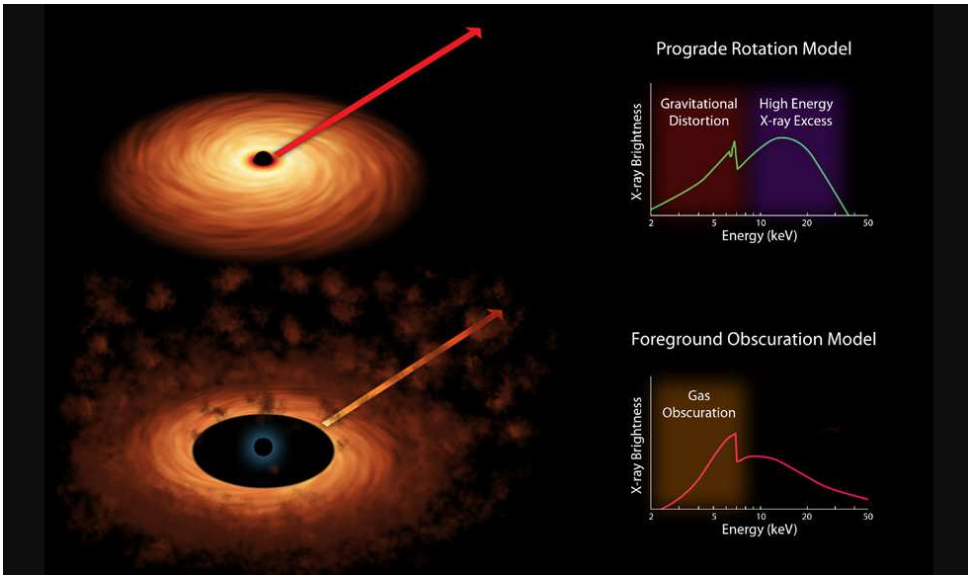

Figure 1.10: An illustration comparing the X-ray spectra produced by blurred reflection and partial covering absorption scenarios. Left column: disk orientation for a Kerr black hole that is un-absorbed vs. that of a Schwarzschild black hole in the presence of absorbing clouds. Right column: spectral profiles of the Fe Kα line which appear very similar for both cases when only observed within the standard 2 – 10 keV regime. Credit: NASA/JPL-Caltech.

from describing not only the potential X-ray components present in AGN spectra, but also detailed descriptions of source geometry and conditions of central engine material. The first detection of an iron line lag in 1H0707-495 – a time delay between the primary component and disk reflection – allowed observers to constrain light travel time and thus physical distance between corona and inner regions of the disk for the first time (Fabian et al., 2009; Zoghbi et al., 2010). Advanced ray-tracing simulations have led to further understanding of the disk emissivity profile which in turn allows the shape and orientation of the corona to be constrained like never before (e.g. Wilkins and Fabian, 2012; Wilkins, 2016; Wilkins et al., 2016; Gonzalez et al., 2017). Such studies are great strides in the advancement of AGN astrophysics. However, as the saying goes: "with great power there must also come great responsibility" (Lee, 1962) and not all objects nor data lend themselves to fine scrutiny.

Supermassive black hole spin has been a parameter of great interest since the potential for observing relativistically broadened Fe Kα lines in AGN was first postulated (e.g. Laor and Netzer,

1989; Reynolds et al., 1999; Reynolds and Nowak, 2003). In principle, constraining black hole spin from an iron line (assuming it is truly broadened by relativistic effects) is as simple as accurately modelling the line profile itself, as discussed above. As more and more AGN were discovered with broad (EW $\gtrsim 1$ eV) Fe Kα features, more spin measurements have been made (e.g. Brenneman and Reynolds, 2006, 2009; Patrick et al., 2011b,a; Reynolds, 2014). Sampling more than one hundred AGN observed by *XMM-Newton*, Guainazzi et al. (2006) found that as many as 50% of Type I objects may have measurable broad lines if an ideal exposure of $\sim$200,000 counts is achieved with the strongest relativistic profiles detected in low-luminosity ($L_{\rm X} < 10^{43}\,{\rm erg\,s^{-1}}$) AGN. This exposure threshold can more easily be broken by the next-generation of observatories like *ATHENA* and the ability to estimate supermassive black hole spin will likely be commonplace in the near future. Yet, despite the increase in relativistic iron line observations, the methodology employed to constrain spin measurements has continued to vary, with individual works using different spectral models, alternative starting assumptions, or different constraints even when examining the same object (Fig. 1.1). Nor are spin measurements limited to fitting relativistic broad lines: Done et al. (2013) employed a continuum fitting technique, Mohan and Mangalam (2014) took advantage of potential quasi-periodic oscillations (QPOs), and Li (2012) used TeV flux variability in radio-loud sources.

There have been several works that discuss the systematics of spin measurements from relativistic Fe Kα lines (Reynolds, 2014; Volonteri et al., 2013; Vasudevan et al., 2016) and a further effort must be made to quantify the limits imposed by common scenarios already seen in literature: attempting spin estimates on lower-luminosity objects, with a single epoch of observation, on a limited bandwidth, and using the standard spectral models. We cannot hope to achieve better results in the coming era if we cannot first identify the blind spots within today's work.

1.3.3 A More Conservative Approach

It is highly likely that a conscientious effort involving both expanding the observable regime as well as implementing model-independent analyses must be done in order to address the challenges

Table 1.1: Examples of various supermassive black hole spin measurements of the same object from different works.

Object	Walton et al. (2013)	Patrick et al. (2011)	Other
3C 120	...	...	< -0.10 / 0.95^{*}
Ark 120	$0.81^{+0.10}_{-0.18}$	< 0.24	$\sim 0.74^{**}$
Fairall 9	> 0.64	$0.60^{+0.19}_{-0.62}$	$0.52^{+0.19}_{-0.15}{}^{***}$
MCG-06-30-15	0.97 ± 0.03	$0.49^{+0.20}_{-0.10}$	$> 0.98^{\dagger}$
Mrk 79	...	< 0.80	$0.70 \pm 0.01^{\ddagger}$
Mrk 335	$0.83^{+0.10}_{-0.13}$	$0.7^{+0.09}_{-0.13}$	$0.93^{+0.04}_{-0.02}$ / $> 0.99^{\S}$
NGC 3783	$0.92^{+0.07}_{-0.03}$	< 0.24	$< 0.88^{\S\S}$
NGC 7469	< 0.96	0.69 ± 0.09	...
IRAS 00521-7054	> 0.84	...	$0.97^{+0.03}_{-0.13}{}^{\P}$

*Cowperthwaite and Reynolds (2012) **Nardini et al. (2011) ***Lohfink et al. (2012) †Brenneman and Reynolds (2006)

‡Gallo et al. (2011) §Gallo et al. (2015) §§Brenneman et al. (2011) ¶Tan et al. (2012)

imposed in Section 1.3.2. Researchers must rise to the occasion now by developing a more conservative approach, tested with current data, in preparation for the next generation of AGN high-energy data that is already upon us.

Within this work, we strive to meet the following goals:

1. To identify and quantify the limits of current practices in measuring key AGN X-ray spectral parameters such as supermassive black hole spin.

2. To apply the knowledge gained to empirical data in order to conservatively estimate the results currently possible.

3. To successfully demonstrate how various other methods, e.g. model-independent analysis and timing studies, can drive spectral modelling in order to fill in the gaps discovered in Point 1.

The first objective will be addressed in Chapter 2 by simulating the average X-ray spectra of Seyfert I galaxies in general, assuming perfect initial conditions such as high count rate, a strong reflection component, and high sample size. For each of the simulated spectra, a variety of key

parameters will be randomly varied within given limits. The number and combination of parameters varied will be chosen to highlight various modelling tests. For each test performed, the simulated spectra will be fit autonomously by a different spectral model than that used to generate the data in order to simulate the blind conditions observers face when fitting true AGN spectra manually. The ability of the spectral models to reproduce the known input parameters will be assessed for a variety of tests focusing on key aspects of AGN spectroscopy, including the ability to constrain supermassive black hole spin.

Chapter 3 will apply the knowledge gained from the critical examination of the spectral fitting process in Chapter 2 to a deep, multi-epoch analysis of NLS1 galaxy Mrk 493. Instead of the more traditional method of relying on the spectral modelling of this object to drive the direction of the exploratory analysis, we rely on model-independent tests and timing studies to direct the X-ray spectroscopy. By adjusting the focus of the analysis in this way, we are able to continue to explore the complex short-term variability in Mrk 493 with less than ideal signal-to-noise. The multi-pronged approach allows us to work around the limits imposed on the spectral fitting process, as elucidated in Chapter 2, and focus on the unique features of Mrk 493 that make it a prime candidate for future observation.

Chapter 4 builds on the analysis of Mrk 493 by investigating an additional source of variability that remains unexplained by the single blurred reflection scenario adopted in Chapter 3. Attempts to spectroscopically identify the source of the $4 - 5$ keV variability seen in the time-resolved PCA include flux-resolved analysis and disk line modelling. A phenomenological discussion of various scenarios such as spallation, disk winds, and disk hot spots follows the analysis.

This collection of works is designed to illustrate both the strengths and limitations of current methodologies used to determine ever-finer details of AGN central engines. The potential for discovery in the field of high-energy AGN astrophysics is enormous, most especially with advances in X-ray optics and computational power. That being said, data analysis of any kind means nothing without knowledge of limits and systematic error to put measurements in context. With a firm grasp of where the boundaries lie, we may approach the next-generation of high-energy data with

confidence and assurance that our methods are sound and conclusions robust.

Chapter 2

How well can we measure supermassive black hole spin?

This chapter was originally published in 2016 in the
Monthly Notices of the Royal Astronomical Society, Volume 458, pp 1927-1938.

2.1 Introduction

It is believed that most black holes will be "born" with some amount of angular momentum, J, instilled in them their progenitors (Kerr, 1963). This angular momentum can change over time, spinning up the black hole through prograde accretion of matter or spinning down through mergers (e.g. Volonteri et al., 2013; King and Pringle, 2006, 2007; King, 2008). Black hole spin, defined by the dimensionless spin parameter: $a = Jc/GM^2$ with theoretical values ranging -0.998 $< a <$ 0.998, is a parameter of extreme interest. It should be noted that this classical Thorne limit (Thorne, 1974) does not include modern magnetohydrodynamic (MHD) accretion theory. If MHD is considered, the limit reduces to $a \sim 0.95$ (e.g. Reynolds et al., 2006). For the last decade or so, sophisticated spectral models and high quality data make it possible to measure the black hole spin parameter in active galactic nuclei (hereafter AGN) for the first time (e.g. Brenneman and Reynolds, 2006).

Supermassive ($M_{\rm BH} \geq 10^6\ M_{\odot}$) black hole spin in particular may have powerful implications on a wide range of scales, from close to the black hole itself out to the host galaxy, due to its direct influence on how mass is accreted in these objects (e.g. Cappi, 2006; Davis and Laor, 2011; Gabor and Bournaud, 2014; Bourne et al., 2014). Studies have shown that accretion flow can significantly affect mass ejection from the central engine of AGN, potentially in the form of high-velocity ($\sim 0.1\ c$) winds (e.g. Gofford et al., 2015) and/or radio jets (e.g. Blandford and Znajek, 1977; Turner and Shabala, 2015; King et al., 2015). These different forms of mechanical AGN feedback, along with intense radiation emitted from the central engine, appear to influence star formation in the host galaxy by means of galaxy self-regulation (Martizzi et al., 2013; Taylor and Kobayashi, 2015). Evidence of such feedback effects may be observed in host-black hole virial relations such as the M-σ relation (Gebhardt et al., 2000) and black hole fundamental plane (Merloni et al., 2003) and may provide the key to supermassive black hole-host galaxy co-evolution. In addition to the cosmological implications, environmental conditions in the innermost regions of Kerr black holes are some of the most extreme in the Universe with evidence of light-bending (e.g. Miniutti and Fabian, 2004; Wilkins and Fabian, 2012; Gallo et al., 2013) and reverberation delays

(Fabian et al., 2009; Zoghbi et al., 2010).

Although the average spin value and total fraction of spinning supermassive black holes are still unknown, the vast majority of current spin measurements from supermassive black holes are high ($a > 0.8$) (Brenneman and Laura, 2013; Reynolds, 2014; Vasudevan et al., 2016). However, large-scale survey analyses are limited due to sampling bias (Vasudevan et al., 2016) and many questions remain as to the true distribution of AGN spin.

Spin measurements are becoming more commonplace as the number of quality spectra from AGN continues to grow. While black hole spin can, in theory, be constrained in a variety of ways such as continuum fitting (e.g. Done et al., 2013), analysis of the broad Fe Kα line (e.g. Walton et al., 2013; Gallo et al., 2015), and potentially via quasi-periodic oscillations or QPOs in stellar-mass black holes (e.g. Mohan and Mangalam, 2014), our most robust measurements from AGN to date rely on our ability to detect a strong reflection component in the X-ray spectra. The Fe Kα line, at 6.4 keV in the source rest-frame, can act as a probe of the innermost regions of the AGN accretion disk: its profile containing information on disk ionization and abundances (e.g. Reynolds et al., 2012; Bonson et al., 2015), inclination and reflection strengths (e.g. Walton et al., 2013), and disk emissivity (e.g. Wilkins and Fabian, 2012; Wilkins et al., 2014).

As with any technique, there are assumptions that go into constraining spin using the Fe Kα line. It is assumed that the emission we observe from the broadest component of the line is coming from the innermost stable circular orbit (ISCO) and that there is a negligible radiative contribution from within the ISCO[1]. The accretion disk is considered to be the standard Shukura-Sunyaev disk – i.e. thin, ionized, and isothermal (Shakura and Sunyaev, 1973) – and that gravitational forces from the central black hole dominates above all. These assumptions seem reasonable for all but the most extreme scenarios and do well to model what is in reality a very complex region.

The X-ray instruments on-board *XMM-Newton* and *Suzaku* are ideal for constraining spin in the manner described above because of their superior sensitivity in the 2 – 10 keV band. Indeed,

[1]While material will continue to emit from within the ISCO, as it falls closer to the event horizon it will no longer be able to make a complete orbit around the black hole, significantly reducing shearing and decreasing the total emission to a negligible amount compared to the rest of the accretion disk.

most supermassive black hole spin measurements in the literature today utilize *XMM-Newton* and *Suzaku* data. Now, with *NuStar* extending observations into the hard X-ray regime up to 80 keV, even more of the reflection spectrum can be resolved and analyzed for more accurate modelling and, thus, spin constraints. However, as measurements are repeated, we find in some cases inconsistent spin measurements for a given AGN. The case of MCG-06-30-15 is a prime example: this broad-line Seyfert 1 galaxy has been studied thoroughly and its spin has been measured multiple times (e.g. Walton et al., 2013; Patrick et al., 2012; Brenneman and Reynolds, 2006). However, spin measurements of MCG-06-30-15 have varied from an extreme limit of $a > 0.98$ to being low-to-moderate at $0.49^{+0.20}_{-0.10}$. Spin analysis for the broad-line radio galaxy 3C 120 is even more contradictory: a prograde spin (a = 0.95) being just as likely as a retrograde ($a < 0.10$) in the same study (Cowperthwaite and Reynolds, 2012; Lohfink et al., 2013).

There are known difficulties in modelling AGN spectra and constraining spin. For example, disk ionization, iron abundance, and reflection fraction can all influence the strength of the Fe Kα line compared to the continuum. The contrast between the line and the continuum will decrease with increasing spin as general relativistic effects begin to dominate, broadening and redshifting an intrinsically narrow feature. Including further intrinsic spectral complexities like partial covering absorbers, outflows, and distant reflection to the already-challenging fits process and it is easy to see why it can be difficult to constrain spin with even the highest-quality data. In addition, we have no standardized procedure for spin measurements using the Fe Kα line – understandable considering the variation and complexity exhibited in the range of objects we observe. There have been several reviews published over the years, which provide some guidance on how best to approach measuring spin (Brenneman and Laura, 2013; Reynolds, 2013). Clearly good data are required. For example, Guainazzi et al. (2006) found that an observation of 200k counts or higher in the 2 – 10 keV band and a broad line equivalent width of at least 100 eV were required for robust detection of a relativistically-blurred Fe Kα feature. These predictions appear to be supported by the current literature.

In this work, we test how reliably we can measure spin and other spectral parameters,

themselves important in constraining a. We test the influence of bandpass in our measurements, specifically looking at the Compton hump regime and its effect on modelling the reflection component. The key questions we will be asking ourselves include: Under which conditions can we be the most confident in our parameter fits, spin or otherwise? Which energy bands are most conducive to model fitting? Are there any steps we can take to limit parameter degeneracies?

This chapter is organized as follows: Section 2.2 describes how the simulated spectral data were autonomously produced and fit, including a detailed review of the different analysis tests performed for reflection fraction, bandpass, and retrograde spin. Section 2.3 provides a step-by-step description of the test results for a reflection fraction of R = 1, including both 2.5 – 10 keV and 2.5 – 70 keV spectral fitting, and Section 2.4 repeats the process for the R = 5 scenario. The results of our retrograde spin tests are discussed in Section 2.5. Section 2.6 discusses the implications of this work, including caveats and limitations, and conclusions are stated in Section 2.7 along with future work.

2.2 Simulations

Ideally one would use a control with known parameters in order to examine the accuracy of a computational model. Unfortunately, we cannot place an AGN in a laboratory and determine its intrinsic properties to use as a baseline. It is possible, however, to simulate a simple X-ray spectrum having the expected characteristics of an average AGN and then fit the simulated spectrum using common techniques in order to examine the reproducibility of model parameters such as spin.

We simulated AGN spectra in the 0.01 – 300.0 keV band with *XMM-Newton* pn response using the model RELXILL: a combination of the reflection model XILLVER (Garcia et al., 2013) and the RELLINE code (Dauser et al., 2013) for relativistic blurring. In order to ensure that data quality and signal-to-noise were not limiting factors, analysis was performed on high quality spectra ($350,000 \pm 1,000$ counts in both the 2.5 – 10 keV and 10 – 70 keV bands) in order to mimic the best observational data currently in hand. At this stage, we did not include more complicated model

components such as Galactic absorption, warm absorbers, partial covering absorbers, or distant reflectors. Galactic absorption would influence the SED below 1 keV, a regime that is not addressed at this time, and additional reflectors or absorbers – as common as they are empirically – would only serve to complicate the simulated spectra further. We must begin by assessing the performance of AGN spectral modelling in the simplest of scenarios to be most conservative.

The following key parameters were varied during the creation of the spectral simulations: photon index (Γ, where $N(E) \propto E^{-\Gamma}$ is the incident flux), inner emissivity index (q_1), black hole spin (a), disk inclination angle (θ), ionization ($\xi = 4\pi F/n$ where F is flux and n is the hydrogen number density), and iron abundance (A_{Fe}) in solar units (see Table 2.1 for details). Inner emissivity index, q_1, describes the emission profile of the innermost region of the accretion disk and is expected to be larger than the classical value of 3 if gravitational light bending is accounted for (see Wilkins 2012 for review).

Varying all six parameters at once, a random number generator produced values within a given range for each parameter for a specified number of spectra. Running error calculations on each key parameter is time consuming for the number of spectra analyzed and we therefore rely on the sampling statistics to reasonably represent the random error in the fitting parameters. The influence of individual error checks and the effect of local minima are discussed further in Section 2.6.3.

Once produced, the simulated spectra were then fit with the REFLIONX model (Ross and Fabian, 2005). Key parameters set at default starting values before allowing to vary in a step-wise fashion mimicking manual fitting procedures. The potential scope of this study is vast. To focus the analysis and provide ourselves with a baseline from which to expand work in the future, we considered four primary model fitting tests: Test A allowed all six key parameters to vary, Test B kept ξ fixed at $75\,\mathrm{erg\,cm\,s^{-1}}$, Test C kept q_{in} fixed at 3, and Test D kept both ξ and q_{in} fixed at the aforementioned values.

We also considered what effect an extended spectral band would have by utilizing *NuStar* response matrices for the FPMA and FPMB detectors (Harrison et al., 2013). In the reflection scenario, the Compton hump illustrates the balance between photon scattering and absorption in

Table 2.1: Model details for simulated spectral analysis. Parameters that are permitted to vary are emboldened. Simulated spectra were created with all key parameters generated randomly within the given ranges. The simulated spectra were then fit with a model whose default parameters were based off of those for average Seyfert 1 AGN. The key parameters were allowed to vary during the fitting process, while both q_1 and ξ were fixed for different fit tests. Parameter values that do not change from the initial Test A are denoted by dashes. All four tests were performed for reflection fractions of R = 1 and again for R = 5.

Parameter	Input Range	Fit Default				Units
		Test A	Test B	Test C	Test D	
inner emissivity (q_1)	**3 – 9**	**3.0**	—	3.0	3.0	
outer emissivity (q_2)	3.2	3.0	—	—	—	
break radius ($R_{\rm br}$)	4.8	6.0	—	—	—	$R_{\rm g} = \frac{GM}{c^2}$
BH spin (a)	**0 - 0.998**	**0.5**	—	—	—	
inclination (θ)	**20 – 70**	**30**	—	—	—	deg
inner disk radius ($R_{\rm in}$)	1	1	—	—	—	$R_{\rm ISCO}$
outer disk radius ($R_{\rm out}$)	400	400	—	—	—	$R_{\rm g}$
redshift (z)	0.05	0.05	—	—	—	
photon index (Γ)	**1.7 – 2.2**	**2.0**	—	—	—	
ionization (ξ)	**50 – 500**	**75**	75	—	75	erg cm s^{-1}
iron abundance (A_{Fe})	**0.5 – 5.0**	**3.0**	—	—	—	solar

the accretion disk: at energies below $\sim$10 keV, any scattered light is absorbed by metals in the disk. Photoelectric absorption diminishes above 10 keV and scattering dominates, appearing in the reflected spectrum as a hump which peaks between 30 – 40 keV. Around 40 keV, the reflected spectrum turns over due to Compton recoil. By extending our analysis into the Compton Hump regime, we are providing more information on the reflected spectrum and thus should be able to better constrain reflection parameters (see Vasudevan et al., 2014, and references therein for review).

The simulated spectra that were initially fit between 2.5 – 10 keV were then refit between 2.5 – 70 keV. It should be emphasized that this does not fully simulate an actual *XMM-NuStar* simultaneous observational analysis, nor was that the intent; we wanted to examine how inclusion of the Compton hump feature influenced our ability to constrain black hole spin. This continues to keep the analysis as instrument-independent as possible and allows us to remain conservative in our approach. In effect, the data were not allowed to overlap. The *XMM*-made spectra were used for $E < 10$ keV, the *NuStar*-made data were used for $E > 10$ keV. Spectra were normalized to the same flux and cross-calibration effects were not considered.

In addition, the influence of the reflection fraction (R) was examined. Reflection fraction is defined as the ratio of reflected flux over primary flux (Dauser et al., 2013). The blurred reflection interpretation of AGN spectra suggests that our ability to measure disk parameters – spin, inclination, ionization, and emissivity – should improve as reflection fraction increases. As more of the total X-ray flux is reprocessed off the accretion disk, dominating the illuminating power law continuum, key features such as the Fe Kα line will be stronger and more of the overall broadband reflection profile is available to be modelled. In order to test this theory, the procedure outlined above for the R = 1 scenario was repeated for simulated spectra with R = 3 and R = 5. Reflection fractions as high as 10 have been reported in the literature (Gallo et al., 2015) and it is not unusual for more exotic AGN, such as Narrow-line Seyfert 1s, to present R-values larger than 5. Thus, in an effort to remain consistent with our average Seyfert galaxy spectra and still simulate significantly higher reflection fractions, our range of R-values appears to be a reasonable choice. In the end, the results of R = 3 were consistently representative of the intermediary between those of R = 1 and 5

and thus will not be discussed further.

Lastly, we expect measurements to be sensitive to the possibility of retrograde spin and so some basic retrograde spin analyses are performed for each reflection fraction. Empirical studies have suggested that it is reasonable to suspect that the vast majority of supermassive black holes have prograde spin, due to the spin-up affect of accretion. That said, there can indeed be cases where a retrograde spinning black hole could be found – such as the immediate aftermath of a supermassive black hole binary merging event (e.g. Hughes and Blandford, 2003; Miller and Krolik, 2013). In the case of a retrograde spin, the ISCO recedes from the event horizon and can be found at $\sim 9R_{\rm g}$. Therefore, there is some justification for allowing the fit model to extend into the retrograde regime and see how that may, or may not, influence our ability to analyze these data overall.

In summary, we created four fit tests (A, B, C, and D) in the 2.5 – 10 keV regime, which we ran for cases of R = 1 and R = 5. We repeated this procedure for an extended energy band of 2.5 – 70 keV to explore the importance of the Compton Hump. We lastly also repeated the broadband fits to examine the influence of allowing the fits to search for retrograde spin.

2.3 Results from a Reflection Fraction of 1

All plot results show a comparison of measured parameter values versus simulated input values (i.e. "intrinsic" spectral values). In order to quantify a model's ability to return the input parameters, one can compare the spread in input values for a given measured value. For example, in Fig. 2.1 the plot of photon index shows that a measured value of Γ = 1.90 indicates a possible input (i.e. intrinsic) value of between Γ_{in} = 1.86 – 1.90, giving a range of $\sim$ 0.04 in Γ_{in}. It is this *input value spread* that we use to visualize how well an AGN parameter can be reproduced.

2.3.1 R = 1: 2.5 – 10 keV spectral fits

The results of the simulated spectral analysis from the 2.5 – 10 keV fitting of Test A are shown in Fig. 2.1. The measured vs. input parameter values are plotted in comparison to the 1:1 dashed

line denoting a "correct" measurement. Dotted vertical lines indicate the ranges in which the random input parameters were generated. Each black point is a simulated AGN spectrum that was autonomously modelled as described in Section 2.2 and has a chi-squared fit statistic $\chi^2_\nu < 1.1$. To better visualize the results, the data were then binned by input value and overplotted (Fig. 2.2). The centre points of these binned data are illustrated by the solid lines with the corresponding shaded bands showing the 1σ error.

Trends are immediately apparent through simple visual inspection of the coloured bands in each panel. For example, the photon index is measured with the most precision (spread in Γ_{in} ranging ~ 0.05), but is consistently overestimated by a few percent of the correct value. Inclination is measured reasonably well (θ_{in} ranging $\sim 10^\circ$) and iron abundance is also well constrained ($A_{Fe,in}$ ranging ~ 1.6 solar), if slightly overestimated. Spin parameter initially appears to be more difficult to measure for AGN with R = 1 using a limited bandpass. Measured values only begin to converge for $a > 0.9$. The fit model seems insensitive to both ξ and q_1. A detailed discussion of spin will be saved for Section 2.6.

Lastly, there are few differences between the model fit tests. Test A, B, C, and D all appear to have similar results and none provides a clear advantage over the others with regards to accurately measuring spectral parameters.

2.3.2 R = 1: 2.5 – 70 keV spectral fits

The binned results of the extended energy band fitting are shown in Fig. 2.3. We can visually confirm that photon index is now both accurately measured and tightly constrained. Iron abundance results are also consistent with those of the 2.5 – 10 keV band, although when the ionization parameter, ξ, is kept fixed (Test B, large green hexes) the measured values are systematically over-estimated. Inclination angle remains well constrained, especially for input values $\theta < 30^\circ$ and $> 60^\circ$ where θ_{in} ranges $\sim 8^\circ$, for an improvement over the narrower spectral analysis (Section 2.3.1) by $\sim 2^\circ$. Inner emissivity and ionization continue to be unconstrained parameters. Once again, there is no significant difference between the model fit tests.

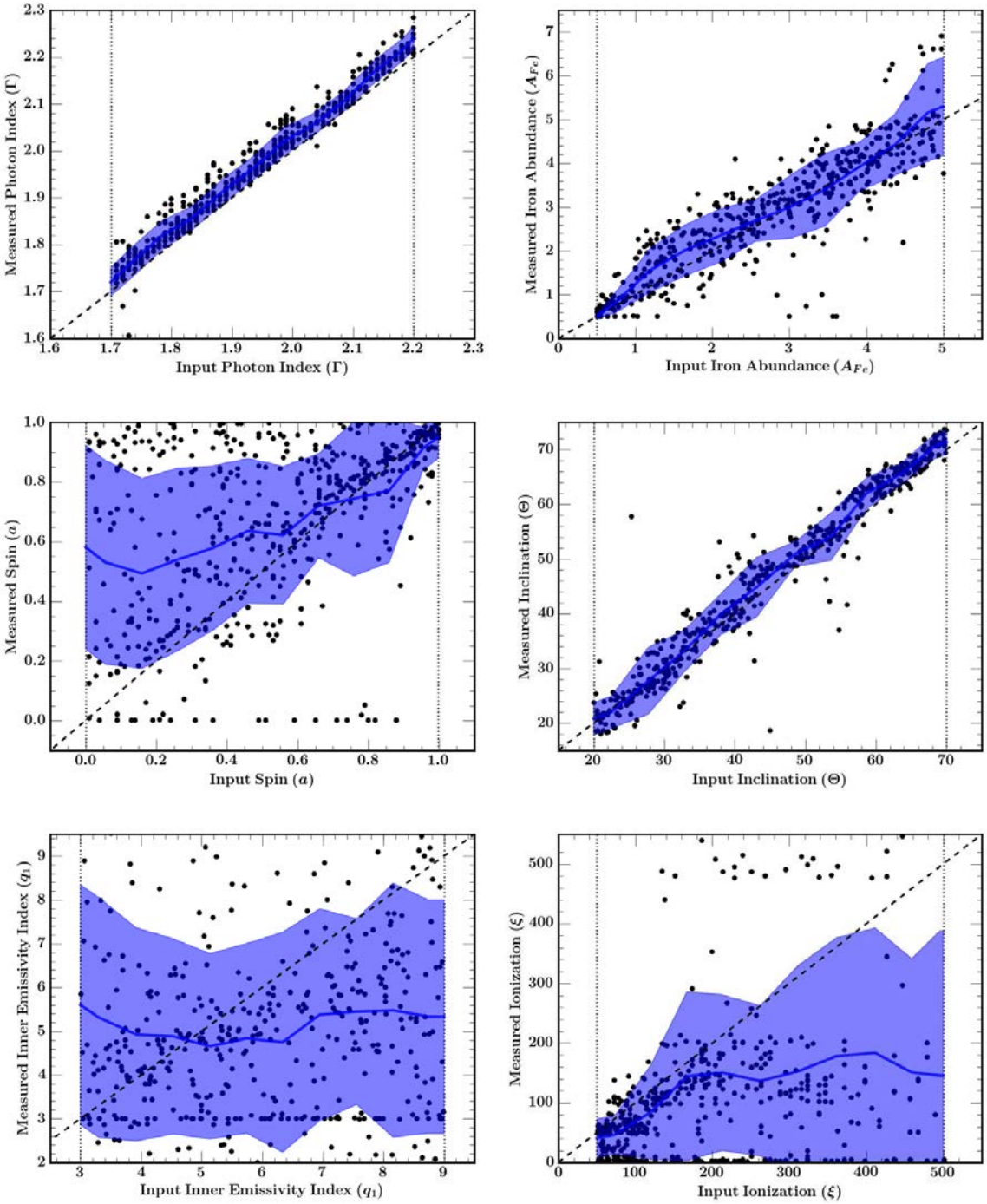

Figure 2.1: The results of the $R = 1$ simulated spectral fitting from Test A, where all 6 parameters were free to vary. Plots show input parameter values on the abscissa and the measured values on the ordinate. The dashed 1:1 line represents a perfect measurement and the dotted lines denote allowed input ranges. Simulated spectra were produced using the *XMM-Newton* pn response and fit from 2.5 – 10 keV using the XSPEC model RELXILL for a collection of randomly-generated input parameters. Each data point corresponds to a modelled spectrum with $\chi^2_\nu < 1.1$. The data were binned by input value and overplotted as blue bands, the widths of which represent 1σ error.

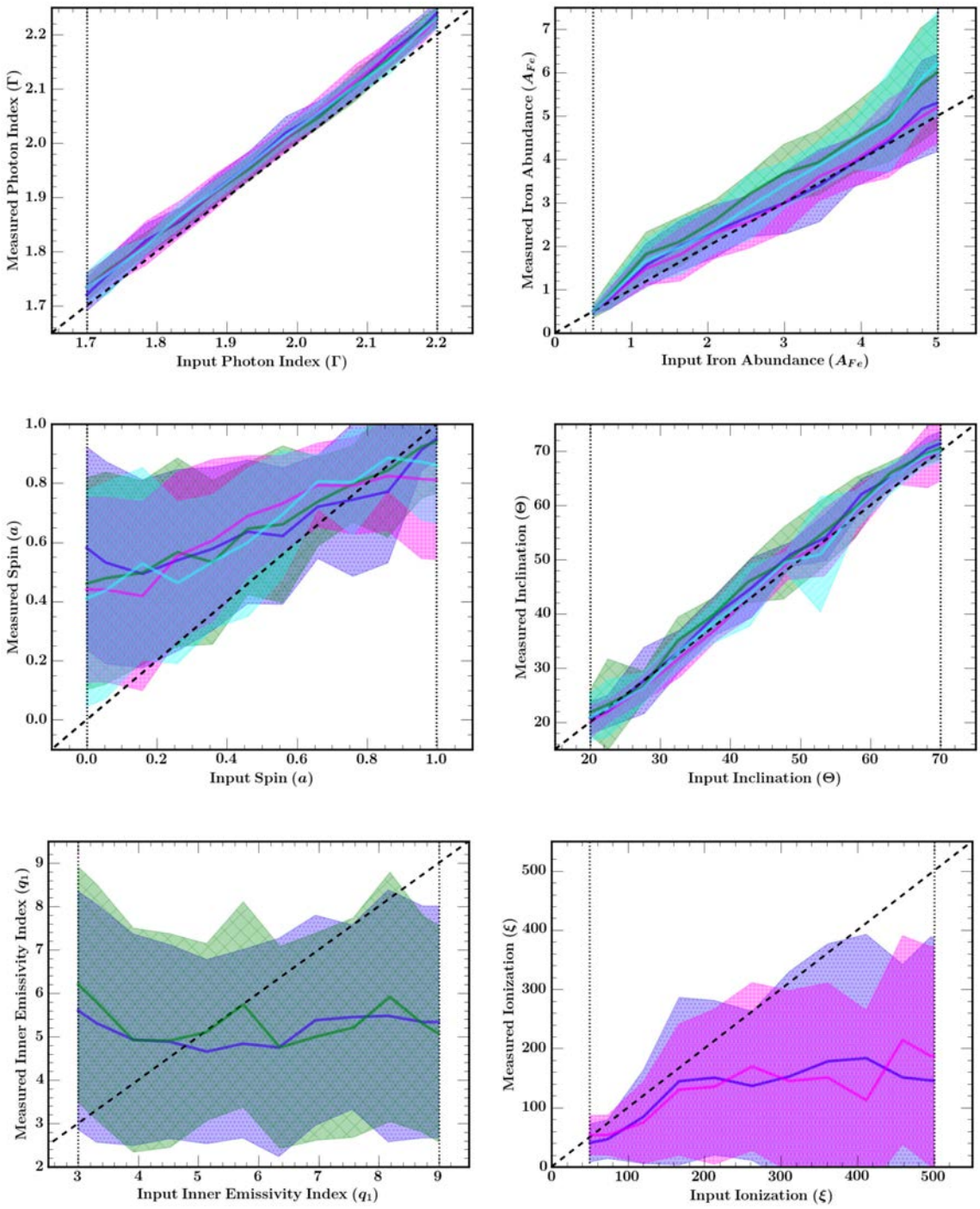

Figure 2.2: Summary of the $R = 1$ results for all four tests in the 2.5–10 keV band. Spectra were binned with respect to input values and plotted with the central solid lines showing the data. The 1σ errors for the Test A (small blue dots), Test B (large green hexes), Test C (small pink crosses), and Test D (small cyan hexes) data are illustrated as opaque coloured bands. Tests where certain parameters remained fixed are not plotted for that respective parameter (e.g. Test C, D for q_1 and Test B, D for ξ).

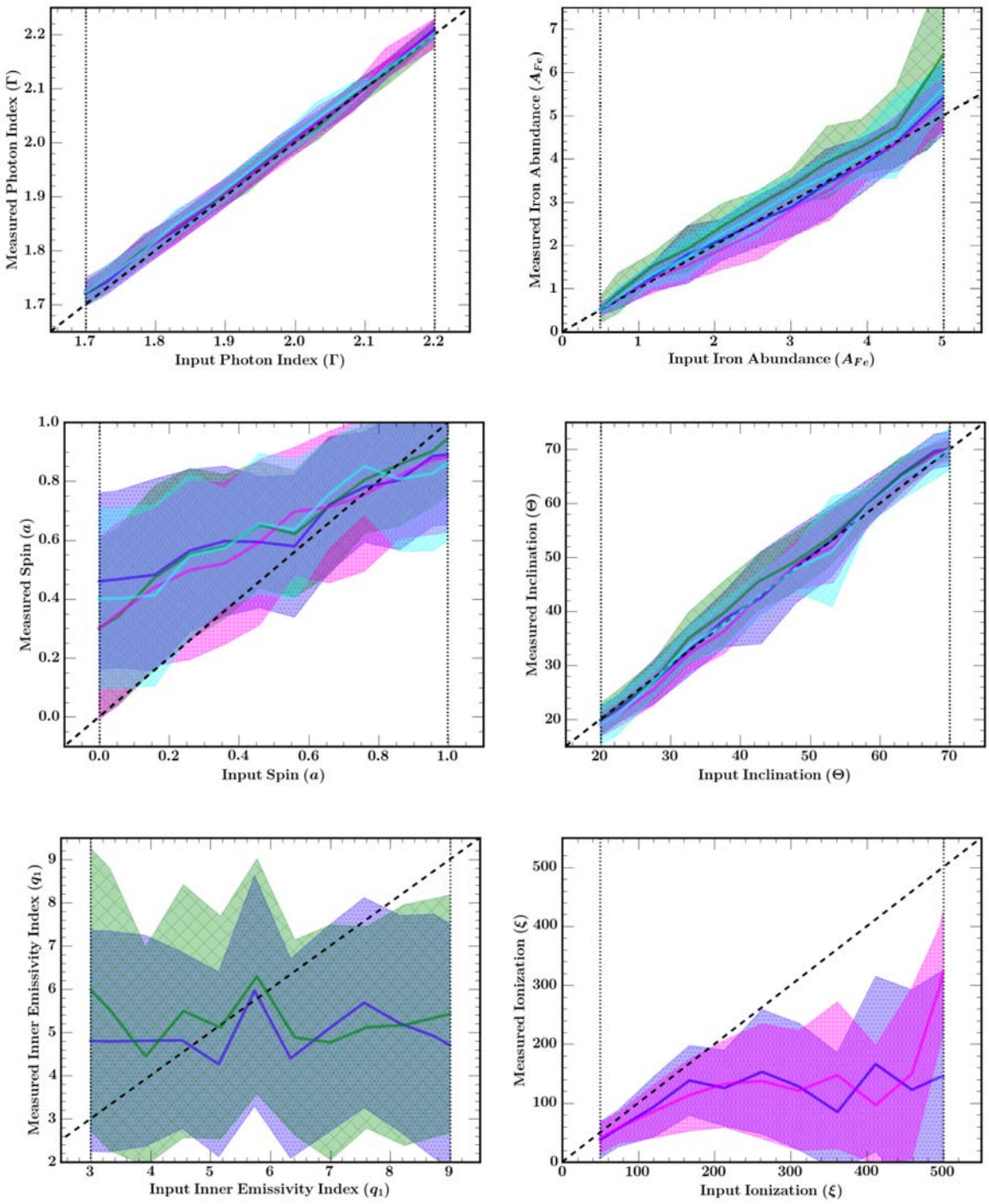

Figure 2.3: Summary of the R = 1 results for the extended 2.5–70 keV fit tests. The spectra that were originally produced using *XMM-Newton* pn response files and fit from 2.5–10 keV were simulated once more, with the same input parameter values, using *NuStar* FMPA and FPMB responses for $E > 10$ keV. The spectra were simultaneously refit from 2.5–70 keV. Band colours and patterns are the same as those in Fig. 2.2.

2.4 Results for a Reflection Fraction of 5

2.4.1 R = 5: 2.5 – 10 keV spectral fits

The results of the simulated spectral analysis from the 2.5 – 10 keV fitting of Test A are shown in Fig. 2.4; graph details are the same as those in Fig. 2.1. As expected, our ability to measure photon index decreases — shown by the parameter being more over-predicted as compared to the 2.5 – 10 keV results for R = 1 and the standard deviations also increasing. Measured iron abundance and inclination angle become more precise for most measured values, with $A_{Fe,in}$ range decreasing to $\sim$0.8 solar and θ_{in} range decreasing to $\sim 5^{\circ}$. However, A_{Fe} is slightly underestimated at intermediate values and θ remains slightly overestimated throughout. Spin is now significantly better constrained as a increases (a_{in} ranging $\sim$0.1 for a measured value of a = 0.95), so it appears an increase in reflection fraction does indeed influence our ability to constrain it. Lastly, ionization also seems to be significantly better constrained than in the R = 1 scenario, for $\xi_{in} < 250\,\mathrm{erg\,cm\,s^{-1}}$, above which the parameter is once again unconstrained. This could arise from line profile diminishing with increased ionization. Inner emissivity index (q_{in}) remains unconstrained.

As with the R = 1 analysis, there are few differences between the individual fit tests and we show Test A results for the 2.5 – 10 keV band in Fig. 2.4 as an accurate representation of all four.

2.4.2 R = 5: 2.5 – 70 keV spectral fits

The binned results of the extended energy band fitting are shown in Fig. 2.5; plot details are the same as those in Fig. 2.3. When the 2.5 – 10 keV R = 5 spectra are refit up to 70 keV, we increase our ability to constrain most reflection parameters. The input range of $A_{Fe,in}$ decreases to $\sim$0.6 solar and we especially improve our ability to constrain the lower measurement limits for a given value of $A_{Fe,in}$. Our range in θ_{in} remains around 5° and, for ionization values below $\sim 200\,\mathrm{erg\,cm\,s^{-1}}$, precision in ξ increases with the increased bandwidth. Above $\sim 200\,\mathrm{erg\,cm\,s^{-1}}$ there is no significant distinction between the fit bands, as is to be expected. Unlike the R = 1

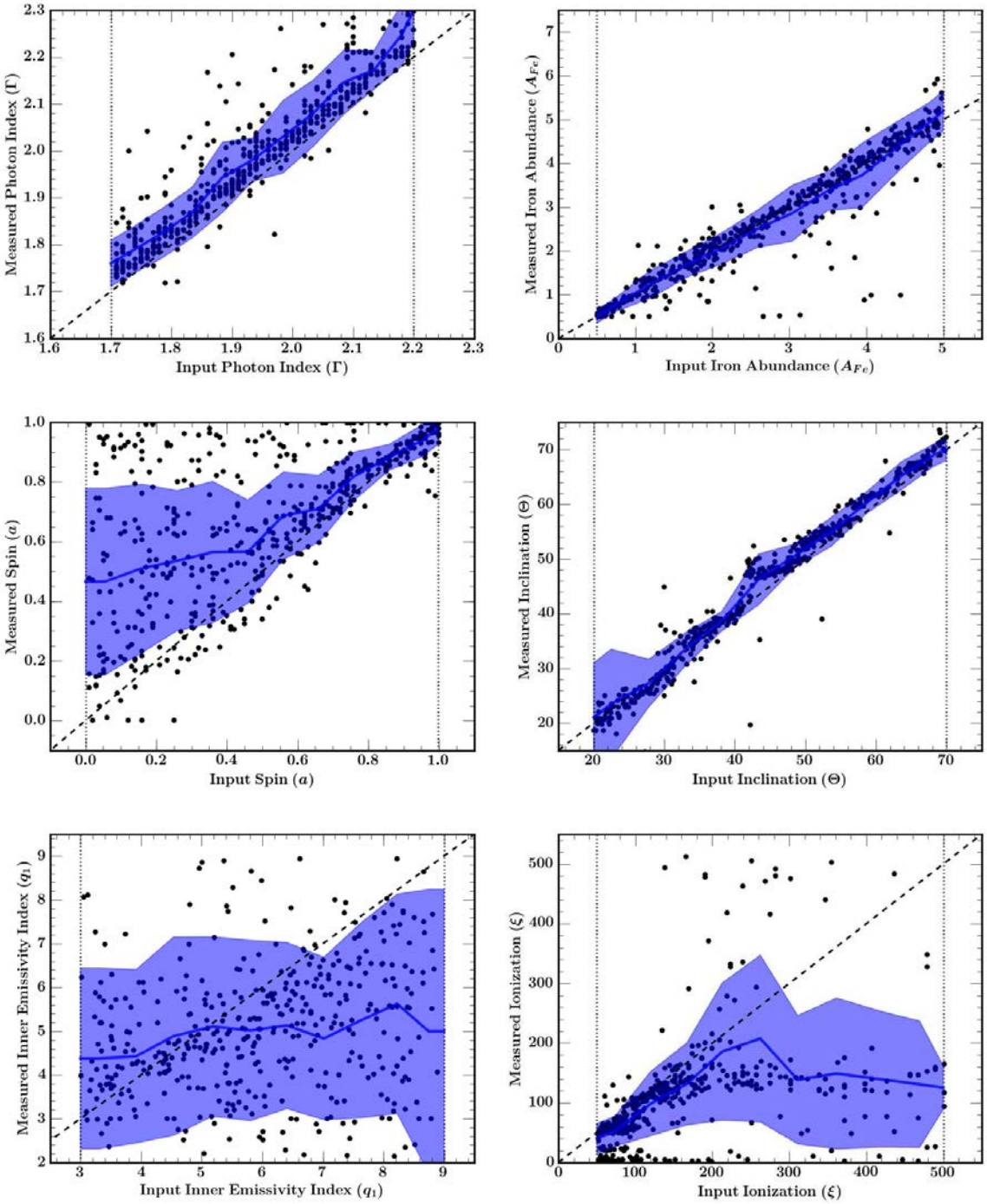

Figure 2.4: The $R = 5$ simulated spectral fitting from 2.5–10 keV. Only the results from Test A, where all 6 parameters were free to vary, are shown for simplicity. Plot details are the same as for those in Fig. 2.1. As expected, an increase in reflection fraction decreases measured precision in primary continuum parameter Γ, but increases measured precision and accuracy in reflection parameters A_{Fe}, a, and θ.

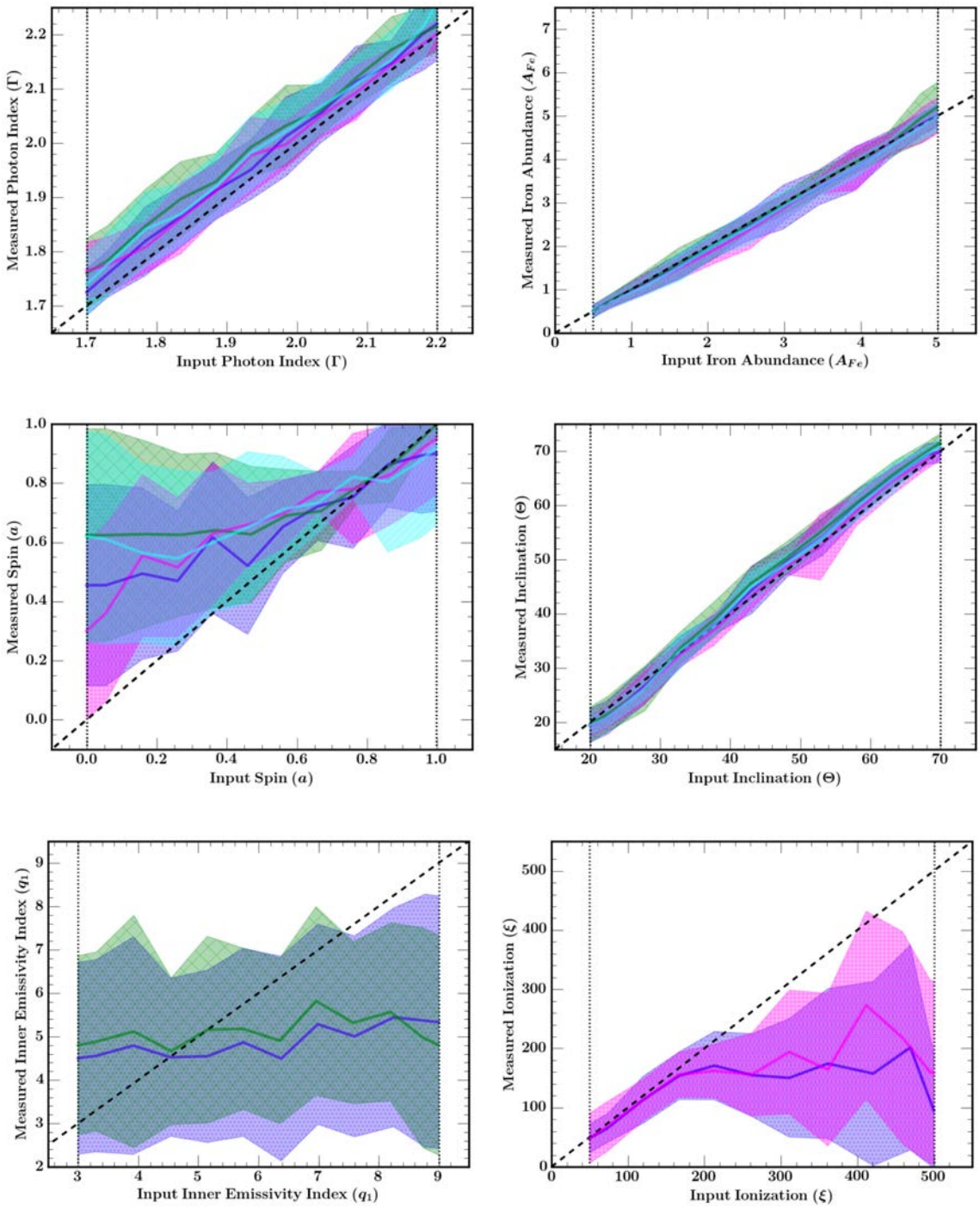

Figure 2.5: Summary of the $R = 5$ results for the extended 2.5–70 keV fit tests. Figure details are the same for those in Fig. 2.2. When spectral fits are extended up to 70 keV, parameters A_{Fe}, θ, and ξ are better constrained. However, it appears we do not improve our ability to measure a. Measurements of a continue to be an improvement over those for the $R = 1$ scenario in the same bandpass.

scenario, however, we do not improve our ability to constrain black hole spin by increasing the fit bandpass. For this case of a higher reflection fraction, possible input spin values for a given measurement increase to a range of a_{in} = 0.25 for a measured value of a = 0.95.

As with all previous results, there is little difference between the model fit tests for this extended bandpass, however all four fit tests are shown in Fig. 2.5 for completeness.

2.5 Retrograde Spin Investigation

Thus far, the possibility of retrograde spin has not been considered. Therefore, the same R = 1 spectra that were used in the 2.5 – 70 keV analysis were refit with the same model and default starting parameters for all fit tests, only now with the spin model boundaries allowing for a retrograde fit (i.e. -0.998 – 0.998). It should be noted that no retrograde fit *should* be found as none of the spectra were simulated with a spin $a < 0$ (see Section 2.2). However, by allowing the model to include retrograde spins in the statistical fitting process, we can investigate any degeneracy in measured spin results and their cause (like in the case of 3C 120). Once the lower limit for possible model a values was extended, our ability to constrain even the most extreme spins diminished in all cases, Test A shown as an example in Fig. 2.6, Left.

Repeating the above procedure for the R = 5 scenario, none of the key parameters were significantly better constrained when the model spin lower limit was relaxed to include a search for a retrograde-spinning black hole (Fig. 2.6, Right). Photon index remained over-estimated and spin itself was entirely unconstrained. As was the case when R = 1, it appears that including retrograde fits increases the standard deviation of measurements at both minimum and maximum spins. Allowing a fit model to process the full possible spin range appears to reduce our ability to measure even the most extreme spin values as tightly.

Despite the difficulty in constraining spin when allowing a full range of black hole spin values, our ability to measure other parameters remained relatively unchanged. We continue to measure prograde spins, which is to be expected given our sample of exclusively prograde objects, and we do

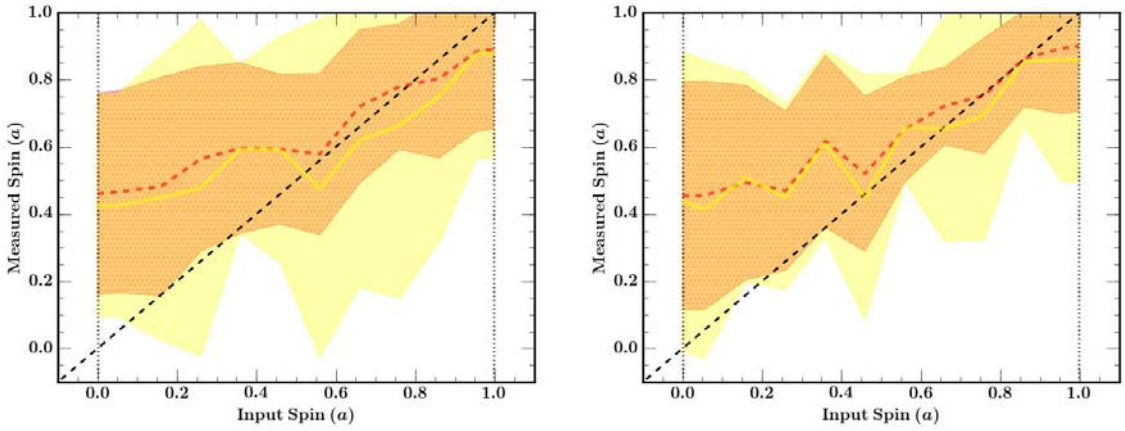

Figure 2.6: Comparison of retrograde spin results for the Test A 2–70 keV fits for R = 1 (Left) and R = 5 (Right). The prograde ($0 \leq a \leq 0.998$, red) model fits are illustrated by the dotted line, with a dotted band showing 1σ uncertainties. The retrograde (-0.998 $\leq a \leq$ 0.998, yellow) model fits are illustrated by the solid line, with a striped band showing 1σ uncertainties. In both cases, allowing the lower limit of model spin to include retrograde fits clearly disrupts our ability to constrain spin at even the highest values of a.

not adversely influence our ability to constrain other key parameters. By including retrograde spins in the modelling we simply reduce our ability to constrain the highest a-values.

2.6 Discussion

2.6.1 R = 1: band comparison

Looking exclusively at the 2 – 10 keV fit results in the R = 1 scenario, photon index and black hole spin tend to be overestimated while observation angle, and iron abundance are well constrained. Photon index is the most consistent parameter and we can be confident that our measurements of Γ are accurate to within about 5%. Constraints of θ are accurate overall: a single measured angle could account for, at most, about 18% of the total values possible and measurements become more precise for increasing inclination angles. This makes sense as more extreme angles induce more observable Doppler effects on the Fe Kα line. While iron abundance is a bit more difficult to constrain, it is measured within about 30%. Lastly, ionization and inner emissivity index are unable to be constrained in the 2 – 10 keV, R = 1 scenario. This is not unexpected due to the limited

bandwidth, which essentially forces the entire reflection component to be modelled based on the Fe Kα line alone.

Extending the fits up to 70 keV, constraints do improve significantly for most reflection parameters. Photon index, iron abundance, and inclination are no longer over-estimated. Ionization also becomes reasonably constrained for values $< 200\,\mathrm{erg\,cm\,s^{-1}}$. However, fit models continue to be insensitive to emissivity index.

Comparing only the spin results from the R = 1 analysis, we can begin to draw tentative conclusions about the robustness of an average AGN spin measurement. Since there is no significant improvement in parameter constraints with fit test, we continue by looking only at fit Test A, where all key parameters are left free to vary: when considering only the standard 2.5 – 10 keV energy band, spin is poorly constrained and grossly over-estimated below $a \sim 0.6$ (Fig. 2.7, Top Left). As mentioned above, additional reflection parameters such as ionization and inner emissivity index are unable to be constrained without additional information.

Extending spectral fits into the hard band up to 70 keV (Fig. 2.7, Top Right) provides only a small improvement to spin measurements below $a \sim 0.6$, however the random error is still substantial. It appears that the most extreme spin measurements, say $a > 0.9$, may be considered sound as the range of possible "input" values (i.e. the intrinsic spin) is reasonably narrow: about 30% the total range of measurement values possible.

Once the lower limit for possible model a values is extended and retrograde spin is allowed for in the fitting process (i.e. -0.998 $\leq a \leq$ 0.998), our ability to constrain even the most extreme spins worsens. Due to the increased random error, it appears allowing for retrograde spin diminishes our ability to measure even extreme values. It is expected that opening the lower limit for retrograde spin would increase standard deviation for smaller spin values, but doing so also had the unexpected consequence of increasing the standard deviation for larger spin values as well. The reason behind this is not immediately clear and it may be an artifact of the fitting process. For example, the larger parameter space is subject to more local minima. Therefore, including the possibility of retrograde measurements complicates the model fitting process, especially for objects with more extreme spin

values – both high and low.

2.6.2 R = 5: band comparison

When the 2.5 – 10 keV R = 5 spectra are refit up to 70 keV, we increase our ability to constrain reflection parameters A_{Fe}, θ, and ξ, consistent with the results of R = 1 investigation. It is interesting to note that our ability to constrain ξ below values of $\sim 200\,\mathrm{erg\,cm\,s^{-1}}$ greatly improves once the fit band has been extended. We can credit our improved ability to measure ξ to the higher reflection fraction and, as in the R = 1 scenario, that ability continues to improve with increased bandwidth. However, we do not improve our ability to constrain black hole spin. For this case of a higher reflection fraction, spin measurement precision decreases, with input range growing from $a_{in} \sim 0.1$ to $a_{in} \sim 0.25$ for a measured value of a = 0.95.

In the case of reflection-dominated AGN, it appears that there is an advantage to measuring black hole spin in the narrower 2.5 – 10 keV band (Fig. 2.7, Bottom Left) rather than in full 2.5 – 70 keV band (Fig. 2.7, Bottom Right). This result may seem counterintuitive, however one must keep in mind that Fig. 2.5 shows all other reflection component parameters are measured well with increasing bandpass range (with the exception of q_1, which is never constrained). It is reasonable to expect that reflection parameters such as θ or ξ become easier to model as more of the reflection component is "observed" via the Compton hump. Parameters like a and A_{Fe} rely on spectral features in the Fe Kα band and would be improved with higher signal-to-noise in the 2.5 – 10 keV band in addition to broadening the bandwidth. Having a broader bandpass when measuring spin exclusively seems to confuse the modelling of the Fe Kα profile and, unless spectral resolution is also increased with the bandwidth, these results suggest the standard 2 – 10 keV band should be used when constraining spin in this manner; i.e. with single instrument, single epoch observations. In other words, we can be confident in our high ($a > 0.8$) spin measurements to about ± 0.1. It should be noted that a simultaneous *NuStar* and *XMM-Newton* observation increases the 2 – 10 keV signal-to-noise as well as extends the observable energy range.

Allowing for retrograde spin measurements in the R = 5 scenario only served to worsen spin

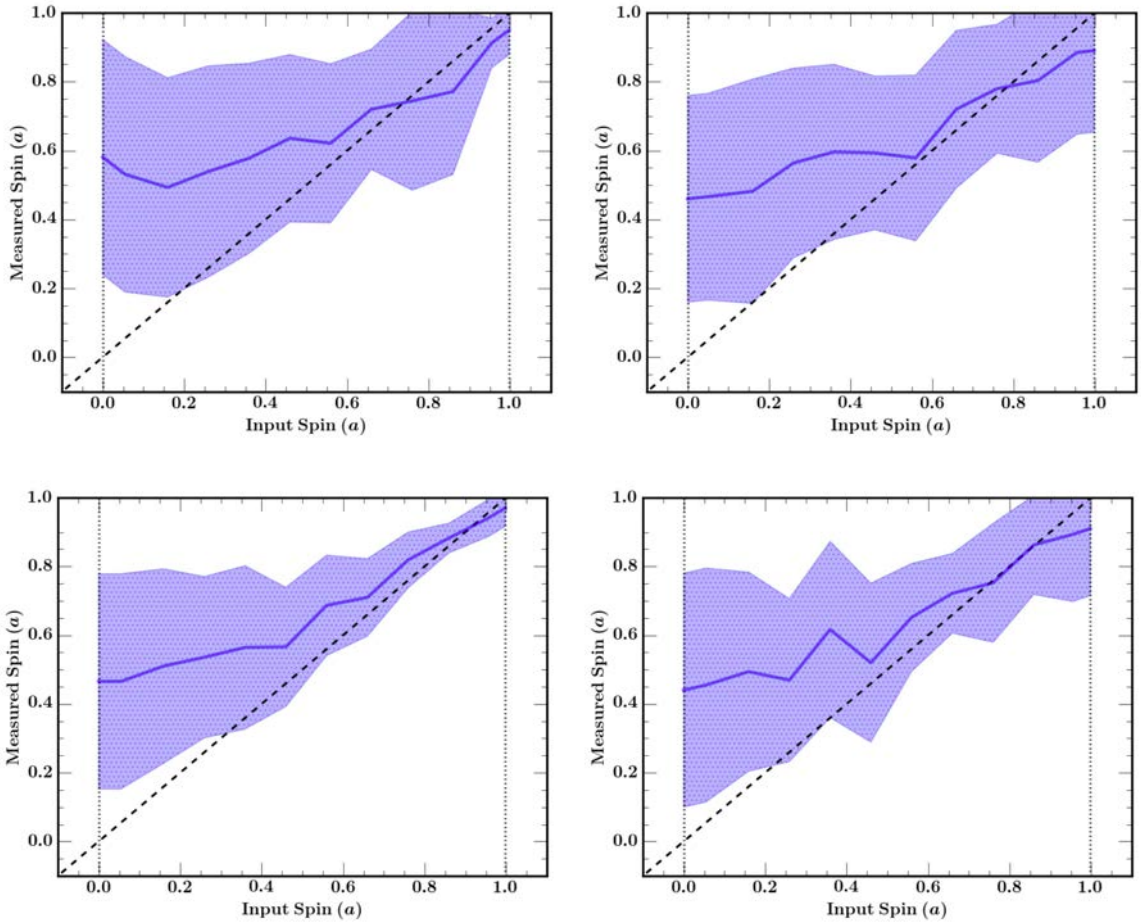

Figure 2.7: Summary of spin measurement results for Test A, placed side-by-side for visual comparison. Top Left: R = 1 spectra fit from 2.5–10.0 keV. Top Right: R = 1 spectra fit from 2.5–70 keV. Bottom Left: R = 5 spectra fit from 2.5–10 keV. Bottom Right: R = 5 spectra fit from 2.5–70 keV. Only prograde spins are allowed in these models. Each R-test uses the same simulated source spectra; fit conditions are modified while input parameters remain unchanged.

constraints when the fit band was restricted to the 2.5 – 10 keV regime. While observing a real AGN with true retrograde spin remains a possibility, their assumed rarity in nature reassures us that this complication in the modelling process is reserved for special circumstances and does not affect the majority of spectroscopic analyses.

2.6.3 Caveats

These simulated spectral fits have confirmed the need for observers to be cautious when attempting to measure reflection parameters, especially black hole spin, via Fe Kα line-fitting. While there is clear justification for similar investigations in the future, one does need to keep in mind the limitations of the work presented here.

As stated in Section 2.2, these simulations imitate the most "ideal" AGN spectrum with regards to detecting the reflection component of the X-ray spectrum (i.e. no absorption, high count rate, local object, moderate and high reflection fractions). We also fully sample the parameter space when creating the simulated spectrum; this ensures reliable error statistics, however a consequence of randomly selecting the parameter values is that we risk creating spectra with less than physical combinations of parameters (e.g. low q_1 with high a and low ξ). An examination of parameter vs. parameter space was performed for all six key parameters investigated here to see if any unphysical or extreme combinations influenced the fitting process. No such correlation was found. It must also be kept in mind that the simulations produced here are strictly mathematical models and while they mimic average Seyfert 1 X-ray spectra, they are not intended to be substitutes for empirical data.

In addition to potentially unphysical parameter combinations, we rely exclusively on the sampling statistics as a representation of the random error in the model fits. This is a reasonable first-order assumption, however there is a risk of our χ^2_ν goodness-of-fit being misrepresented by local minima. Indeed, the greater range with which the fit could fall into local minima could easily explain the observed retrograde spin results.

In an effort to understand such effects, we investigated the role of local minima by refitting the simulated spectra from the R = 1, Test A, 2.5 – 70 keV scenario (Fig. 2.3, blue). The spectra

were refit with the same model as before however this time we included error checks on all six key parameters. While this cannot guarantee absolute minima, it reduces the likelihood of local analogues. The results of both error tests were consistent and there were no significant differences between the measurement profiles using error checks and those that do not. This does not imply that error checks in spectral model fitting are superfluous: the overall fraction of good (i.e. $\chi^2_\nu < 1.1$) fits increased with fits that included error checks compared to those without. However, using the scatter in a larger number of spectra seem comparable to measuring errors on each parameter. Thus we did not run parameter error checks for the other tests in the interest of time.

Perhaps most importantly, AGN astronomers also do not rely exclusively on Fe Kα line-fitting when performing true empirical analysis, but rather use a multi-pronged approach that often includes multi-epoch observations, timing analysis like fractional variability and reverberation mapping, and/or more robust statistical methods such as principle component analysis. In this simulated study, we have focused solely on fitting a single-epoch of spectral data within two bandpasses. If we were to measure a supermassive black hole spin to be in any region shown by these plots to be less constrained, it is possible that a more confident estimate could still be obtained by better defining the reflection component using alternative methods.

This work confirms that we can be most confident in our supermassive black hole spin measurements for high values of spin, above $a > 0.8$ and it can be constrained to within $\sim 10\%$ under the simulated conditions. It is important to note that most AGN that have undergone spin analysis are narrow-line Seyfert 1s that literature has shown are suspected of being reflection dominated (i.e. high R-value) and maximally spinning. Since brighter AGN with high spin are now shown to be easier to measure, there may be a sampling bias in AGN spin measurements and it might be difficult to determine the true spin population distribution (Vasudevan et al., 2016).

2.7 Conclusions & Future Work

In summary, analysis of simulated average AGN spectral fitting under a blurred reflection scenario has shown that accurately measuring standard X-ray spectral parameters can indeed be a challenge. If restricted to the oft-utilized Fe Kα line region of 2 – 10 keV, most parameters are over-estimated and spin itself is unconstrained for all but the most extreme values. Once the bandpass is extended up to 70 keV the measurements improve for most parameters, those like Γ, A_{Fe}, and θ are no longer over-estimated, and spin is better constrained for the highest values. An increase in reflection fraction improves measurements further for most reflection parameters, while decreasing our ability to constrain Γ slightly — as to be expected in a reflection-dominant scenario. The inner emissivity index (q_1) is never constrained under the conditions tested and likely requires detailed fitting of the Fe Kα profile in order to be properly estimated. Including the soft-excess in these analyses is an interesting, but lengthy challenge and will be considered in future work.

The results discussed above are found under particular conditions. That being said, those conditions are conservative and do well at representing the standard model-fitting practice of a bright AGN source. Therefore, the fact that we seem to be less able to constrain spin for intermediate values warrants caution when making empirical spin estimates and fully justifies further investigation into AGN spectral modelling as a whole. However, it must be emphasized that black hole spin can be measured with confidence for $a > 0.8$ to about ± 0.1, most especially for objects with a higher reflection fraction.

The usefulness of observatories like *NuStar* for AGN spectroscopy cannot be overstated. The effects of increased bandwidth, improved signal-to-noise, and high spectral resolution have not been tested here. However, we expect these to improve our ability to model AGN spectra.

Acknowledgments

The authors would like to thank the referee, Dr. Chris Reynolds, for constructive comments as well as Dr. Dan Wilkins, Dr. Herman Marshall, and Dr. Dom Walton for their insightful commentary regarding this study. The *XMM-Newton* project is an ESA Science Mission with instruments and contributions directly funded by ESA Member States and the USA (NASA).

Chapter 3

Deep analysis of short-term X-ray variability in Mrk 493 driven by model-independent methods.

The work in Ch.3 & Ch.4 are being prepared as one manuscript for publication in the Monthly Notices of the Royal Astronomical Society.

3.1 Introduction

Narrow-line Seyfert 1 (NLS1) galaxies are a class of active galactic nuclei (AGN) that are known for being extreme: possessing rapid short-term X-ray variability, displaying multi-component X-ray spectra, and accreting at high-Eddington rates (Sulentic et al., 2000; Grupe, 2004; Grupe et al., 2010). The NLS1 galaxies 1H0707-495 and IRAS 13224-3809 made history with the discovery of relativistically blurred Fe Lα lines and reverberation lags (Fabian et al., 2009, 2012). X-ray reverberation lags are the delays in radiation between the primary emitter and its reprocessed emission off the innermost regions of the accretion disk. By measuring these delays, the geometry of the environment close to the central black hole can be mapped down to distance scales too small to be probed by other means. The presence of Fe Lα features was also groundbreaking as it confirmed that the source of soft-excess radiation in 1H0707-495 and IRAS 13224-3809 is reflection, as predicted by Ross and Fabian (2005). The soft-excess is a feature below ~ 2 keV that is nearly ubiquitous in the spectra of Type 1 AGN and the cause of its emission is still being debated (Done and Nayakshin, 2007; Done et al., 2012; Boissay et al., 2016). Thus, studying the X-ray spectra of Fe Lα emitting NLS1 objects provides us with an opportunity to not only map the innermost regions of AGN, but also be confident that we truly are observing reflected emission from the accretion disk.

Mrk 493 is a local (z = 0.03) AGN that has been viewed by *Swift* every few years since 2005 and most recently in October of 2015. Its observation history has shown that this object is on average about twice as bright as the better-known NLS1s 1H0707-495 and IRAS 13224-3809. A pointed 13.7 ks *XMM-Newton* observation in 2003 revealed an X-ray light curve with slight variability and a spectrum with a prominent soft-excess. A clear Fe Kα emission line can also be seen in the 2003 spectrum and, perhaps more interestingly, Hurlburt (2013) identified Mrk 493 as a potential Fe Lα emitter. The 2003 observation was taken in Large Window Mode and the pn data were piled-up. A proposal to re-observe Mrk 493 in a longer campaign with *XMM-Newton* in Small Window Mode was granted with a 190 ks exposure. During the 2015 follow-up observations the source dropped in flux by more than a factor of two. A preliminary look at the 2015 EPIC spectra demonstrate that

Mrk 493 is an interesting object, with a prominent soft-excess, and variability that has its count rate doubling in less than 2 ks. Despite its interesting spectral profile and behaviour, Mrk 493 has not previously been the subject of an in-depth study. Thus, a deep analysis of the 2015 *XMM-Newton* data is presented in this work in an attempt to better understand this NLS1 galaxy.

This work is organized as follows: Section 3.2 summarizes the data collection and reduction. Section 3.3 introduces the model-independent techniques first utilized to characterize the behaviour of Mrk 493 in the X-ray. A preliminary look at the average spectra for each 2015 observation is shown in Section 3.4 and is followed by deeper time-resolved analysis in Section 3.5. A blurred reflection scenario is tested in Section 3.6 via time-resolved spectroscopy and fractional variability modelling. Section 3.7 summarizes the findings and discusses their implications, and Section 3.8 presents the concluding remarks.

3.2 Observations and data reduction

The 2003 *XMM-Newton* observation (ObsID 0112600801; hereafter XMM03) was during revolution 568 starting on 16 January 2003 and spanned 19 ks. The pn camera (Strüder, 2001) operated in large window mode and the two MOS detectors (Turner et al., 2001) operated in small window mode, all three detectors used a medium filter.

The first 2015 *XMM-Newton* observation (ObsID 0744290201; hereafter XMM15a) was during revolution 2786 starting on 24 February 2015 and spanned 97 ks. The second observation (ObsID 0744290101; hereafter XMM15b) was during revolution 2789 starting on 2 March 2015 and spanned 100.4 ks. The EPIC detectors in this case all operated in small window mode with a medium filter for both 2015 observations.

The Optical Monitor (OM) (Mason et al., 2001) and Reflection Grating Spectrometers (RGS1 and RGS2)(den Herder et al., 2001) observed simultaneously with the EPIC instruments during the 2015 epochs, however the OM data appeared dominated by the host galaxy and will not be discussed further. RGS data analysis will be discussed elsewhere. Observation details are listed in Table 3.1.

Table 3.1: Mrk 493 *XMM-Newton* data log for the single 2003 and two 2015 observations.

(1) ObsID	(2) Designation	(3) Start Date	(4) System	(5) Instrument	(6) Duration	(7) Mode	(8) Filter	(9) GTI (ks)
0112600801	XMM03	2003/01/16	EPIC	pn	19.22 ks	large window	medium	13.63 ks
(no flare)				MOS 1	19.22 ks	small window	medium	18.41 ks
				MOS 2	19.22 ks	small window	medium	18.41 ks
0744290201	XMM15a	2015/02/24	EPIC	pn	95.91 ks	small window	medium	66.91
(no flare)				MOS 1	95.91 ks	small window	medium	92.87
				MOS 2	95.91 ks	small window	medium	92.83
0744290101	XMM15b	2015/03/02	EPIC	pn	99.32 ks	small window	medium	69.21
(flaring)				MOS 1	99.32 ks	small window	medium	87.38
				MOS 2	99.32 ks	small window	medium	85.91

Data files from both epochs were processed to produce calibrated event lists using the *XMM-Newton* Science Analysis System (SAS) version 15.0.0 and latest calibration files. The data were examined for background flaring and pileup. Moderate flaring was seen throughout XMM15b and those time periods were ignored. No pileup was detected in either observation. Source photons were extracted from a circular region 35 arcsec in radius and centred on the object. The background photons were extracted from an area 50 arcsec in radius close to the object and then scaled appropriately.

Single to quadruple events were selected for the MOS data while single and double events were selected for the pn. Events next to a bad pixel or the CCD edge were omitted (i.e. data quality flag set to zero). Spectra from the 2015 data of both observations were limited to the 0.3 – 8.0 keV range based on high background at $E > 8$ keV. The pn spectra of XMM15a were limited further on the high end, between 0.3 – 6.5 keV, due to high background beginning at 6.5 keV. The resulting mean count rates for XMM03 were: $5.86\,\mathrm{count\,s^{-1}}$ for pn, $1.41\,\mathrm{count\,s^{-1}}$ for MOS 1, and $1.43\,\mathrm{count\,s^{-1}}$ for MOS 2 in the 0.3 – 10.0 keV band. XMM15a had mean count rates of: $1.88\,\mathrm{count\,s^{-1}}$ for pn, $0.45\,\mathrm{count\,s^{-1}}$ for MOS 1, and $0.45\,\mathrm{count\,s^{-1}}$ for MOS 2 0.3 – 8.0 keV band. And lastly, XMM15b had count rates of: $2.03\,\mathrm{count\,s^{-1}}$ for pn, $0.50\,\mathrm{count\,s^{-1}}$ for MOS 1, and $0.49\,\mathrm{count\,s^{-1}}$ for MOS 2 for the same energy band.

All spectral model fitting was performed using the X-ray spectral fitting package XSPEC v. 12.9.0. Model parameters are reported in the rest frame of the AGN (z = 0.03, D_{L} = 133 Mpc) and a cosmology of H_0 = $70\,\mathrm{km\,s^{-1}\,Mpc^{-1}}$, q_{o} = 0, and Λ_{o} = 0.73 is assumed. All models include a Galactic column density of $N_{\mathrm{H}} = 2.11\times10^{20}\,\mathrm{cm^{-2}}$ as determined from the LAB Survey[1] (Kalberla et al., 2005). Errors on model parameters correspond to a 90% confidence level.

[1] http://heasarc.nasa.gov/cgi-bin/Tools/w3nh/w3nh.pl

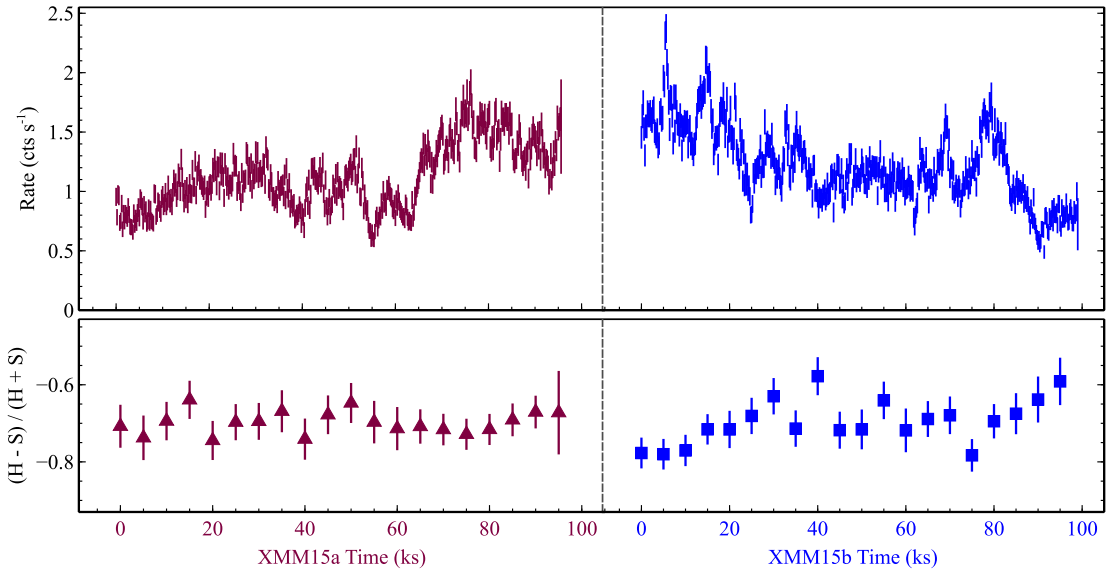

Figure 3.1: The 0.2-8.0 keV merged-MOS background-subtracted light curves and hardness ratios of Mrk 493. Top: light curves of XMM15a (maroon triangles) and XMM15b (blue squares) are plotted side-by-side for comparison; the observations are separated by 5 days – XMM15a began on Feb. 24$^{\rm th}$ and XMM15b on March 2$^{\rm nd}$. Bottom: same as Top for hardness ratios comparing soft (0.35–0.5 keV) and hard (5–8 keV) energy bands. Light curves are binned by 200 s while hardness ratios are binned by 5 ks.

3.3 Model-Independent Analysis

Before delving into detailed multi-epoch spectroscopy, we first approached the 2015 Mrk 493 data in a model-independent fashion. It is very common for multiple scenarios to describe spectra equally well (Bonson et al., 2015; Gallo et al., 2013, 2015) and so we hope to gather preliminary clues as to the nature of X-ray variability in Mrk 493 that may aid in later spectral analysis.

Source photons were extracted to create light curves in a variety of energy bands. For light curves, we considered down to 0.2 keV and the bands spanned 0.2 – 8.0 keV and 0.2 – 10.0 keV for XMM03 and both XMM15a and XMM15b, respectively. The light curves from all EPIC instruments proved consistent in their respective epochs and thus MOS 1 and 2 light curves were combined per epoch, taking care to match the observation start and stop times.

The 2015 broad band merged-MOS light curves are shown in Fig. 3.1 (Top). A simple visual inspection shows that the source is indeed variable on timescales as short as $\sim$ 5 ks as well as across

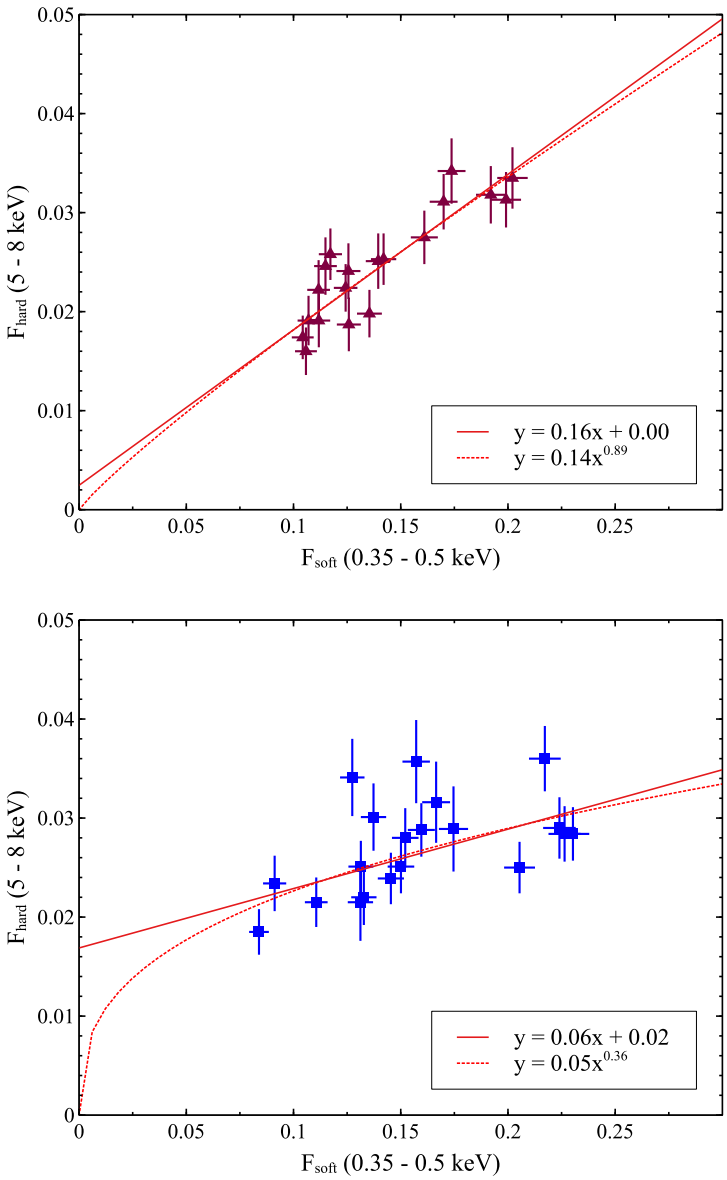

Figure 3.2: Flux-flux plots of the two 2015 observations for the soft and hard bands. The data for both XMM15a (maroon triangles) and XMM15b (blue squares) were fit with linear (solid red line) and power law (dotted red line) models.

the entire 2015 observational campaign. The XMM03 light curve varied in flux by a similar factor of around 50%. Hardness ratios of the soft (0.35 – 0.5 keV) and hard (5 – 8 keV) bands in each epoch were plotted with respect to time and reveal the XMM15b spectrum softening as the broadband flux increases (Fig. 3.1, Bottom). Re-plotting the same hardness ratios with respect to flux did not show significant flux dependence. This does not mean the variability is insensitive to flux, but rather that changes in the soft and hard bands may change at relatively constant ratios with respect to one another.

To further this investigation, flux-flux plots comparing the same bands were created following (Taylor et al., 2003) with the same light curve binning of 5 ks. The results show that XMM15a variability could be either linear (χ^2_ν= 0.93) or pivoting (χ^2_ν= 0.96) in nature while neither model is acceptable for XMM15b (χ^2_ν= 1.59 and 1.50 for linear and pivoting models, respectively). Therefore, while the exact nature of the X-ray variability is still unknown, it appears to change between the first and second half of the 2015 campaign.

The spectra of all three epochs of observations were fit with a power law between 2 – 10 keV (2003 data, grey) 2 – 8 keV (XMM15a, maroon; XMM15b, blue), excluding the iron line region, and allowed only normalization to be free. Extrapolating down to 0.3 keV (Fig. 3.3, Top), we see that the three epochs have similar spectral profiles and differ mostly below 1 keV (Fig. 3.3, Bottom). There appears to be a change in soft-excess as well as the presence of positive residuals around 6 keV (Fig. 3.3, Bottom).

Unless otherwise noted, the XMM03 analytical results were consistent with those of the 2015 data in all following analyses and the 2015 results alone are discussed due to their higher data quality.

3.3.1 Fractional Variability

Root-mean-squared fractional variability ($F_{\rm var}$) analysis is used to quantify the variability intrinsic to a light curve while accounting for uncertainty as a function of energy (Edelson et al., 2002; Ponti et al., 2004). This parameter compares the amplitude of any variations present in a given bandpass by calculating the standard deviation of counts to the average in that bandpass.

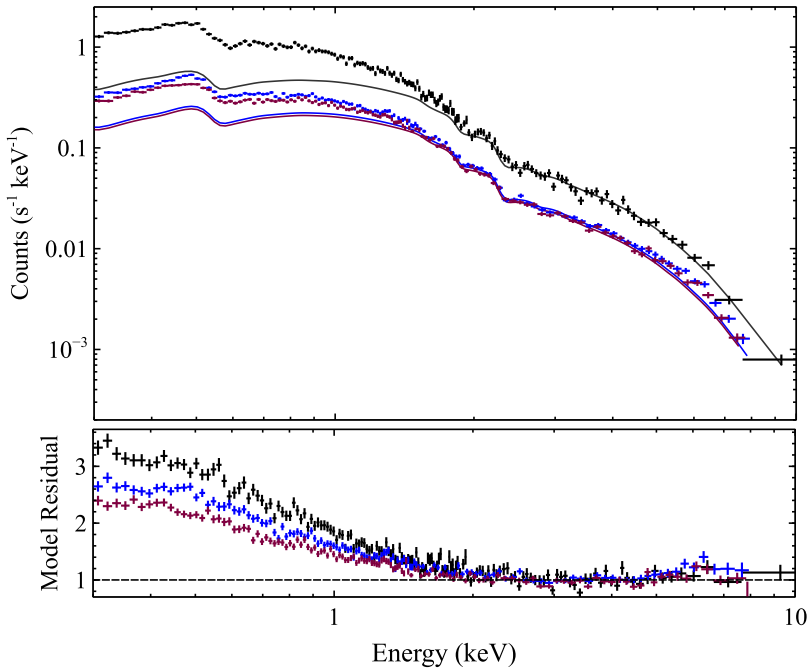

Figure 3.3: XMM03 (grey), XMM15a (maroon), and XMM15b (blue) X-ray spectra simultaneously fit with a power law, the photon indices of which are linked across the epochs. The model (grey solid line) is fit from 2–8 keV (2003 data) and 2–8 keV (2015 data) excluding the iron line region and then extrapolated down to 0.3 keV (Top). The model residuals for all three epochs (Bottom) show a large soft-excess. The 2015 data also have some positive residuals around 6 keV.

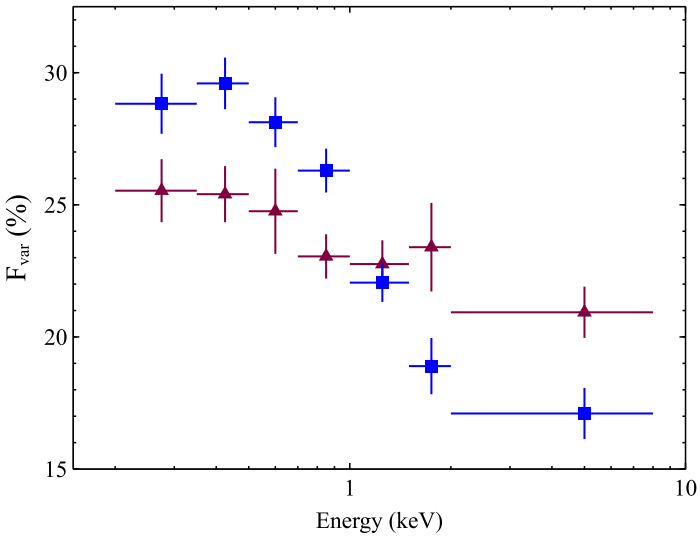

Figure 3.4: Fractional variability ($F_{\rm var}$) of the merged-MOS broad band light curves. Both epochs show increased spectral variability in the soft (<1 keV) band, with the variability in XMM15b far more significant. Colours and symbols are the same as those in Fig. 3.1.

$F_{\rm var}$ thus compares the relative magnitudes of spectral variability, independent of time or flux. Mathematically,

$$F_{\rm var} = \frac{1}{\langle X \rangle} \sqrt{S^2 - \langle \sigma_{\rm err}^2 \rangle} \tag{3.1}$$

where $\langle X \rangle$ is the mean count rate, S^2 the total variance of the light curve, and $\langle \sigma_{\rm err}^2 \rangle$ the mean squared error. The $F_{\rm var}$ was computed for a total of nine energy bins using uncertainties following the procedure defined by Ponti et al. (2004).

The $F_{\rm var}$ profile of all three epochs were calculated and compared, however the 2003 results did not show any significant variability and will not be discussed further. The light curves were binned by 200s and the energy bins spanned 0.2 – 8.0 keV, the last bin ranging from 5 – 8 keV due to the increase in high-end noise. The results from the pn instrument were compared to that of the MOS to check for consistency and were found to not significantly differ.

The $F_{\rm var}$ profile for XMM15a (Fig. 3.4, maroon triangles) shows a slight increase in soft-band variability. Spectral variability greatly increases in the second epoch where the $F_{\rm var}$ profile for

XMM15b shows variability peaking around 0.4 keV and steadily declining as energy increases (Fig. 3.4, blue squares). Thus most variability in XMM15b is seen in the softest X-ray bands. This is in agreement with the $F_{\rm var}$ profiles seen in other Type I Seyferts which can be bell-shaped or sloped: peaking in the intermediate bands or having a linear trend as changes in the primary power law source drives the changes observed (Gallo et al., 2013; Fabian et al., 2013; Bonson et al., 2015).

A lack of evidence of spectral hardening/softening (Fig. 3.1, Bottom) does not contradict the clear presence of spectral variability in the source, as seen in both the broad band light curves and $F_{\rm var}$ analysis. Rather, it could mean that the source(s) of variability changes by equal rates in both the hard and soft bands and thus the rate of change is constant over both time and flux.

3.3.2 Principal Component Analysis

A powerful tool used in many scientific fields for multi-variable statistical analysis is Principal Component Analysis (hereafter PCA). PCA performs an eigenvalue decomposition in which a data set is is modelled by a number of linear relationships that minimize low or redundant information. These linear relationships are the principal components and are made up of an eigenvalue or coefficient (also called a 'loading') along with its corresponding eigenvector. The principal components are not correlated by definition (see Feigelson and Babu, 1992, for review). In other words, PCA looks for a collection of related variables in a data set that explains most of the variance and clumps them together into a single principal component. It then repeats the process, finding the second most influential variables (giving the second principal component), and so on until a data set is reduced to a few principal components that model variance in the data best.

PCA is a powerful technique as it is model-independent and has the ability to reduce a dataset with hundreds of parameters down to a much more manageable size while retaining information. In the case of AGN timing analysis, PCA can be applied to isolate the uncorrelated variable components in an X-ray spectrum and quantify their variability. A PCA spectrum can then be created in order to identify which of the original spectral component(s) may be responsible for the majority of the variability (e.g. Parker et al., 2014a,b, 2015).

Using the PCA_PUBLIC code[2], PCA was completed on data from all three *XMM-Newton* observations: the 2003 and both 2015 epochs. After testing time bin sizes of 10, 15, and 25 ks, the spectra were binned by 10 ks and analyses were conducted on the individual epochs alone, the 2015 epochs combined, and all three epochs combined. The results were consistent across the three EPIC instruments and so the individual MOS data were merged for increased signal-to-noise and are shown as an example.

Error bars were calculated by randomly perturbing the input spectra, recalculating the PCA, and finding the variance in the PCs themselves (Miller, 2007). The significance of individual components was assessed via log-eigenvalue (LEV) diagrams: the data were plotted by fractional variability as a function of eigenvector number. The data asymptotically approach null variability and components that fall above the trend outlined by the majority of points were considered significant (see Parker et al., 2014a, Fig. 2 as an example).

The PCA of the individual 2015 epochs were consistent and the epochs were combined. The first three PCs of the combined 2015 run were significant although only PC 1, with $52.1\pm4.5\%$ fractional variability, shows any sort of profile shape. As the sign of the counts is inconsequential, one can interpret PC 1 as showing a source of variability that dominates at softer energies and decreases linearly toward zero with increasing energy. There is a slight increase in variability again around 5 keV before the trend once again diminishes. While accounting for a combined $\sim 25\%$ of the variability between them, PCs 2 and 3 appear to dominate only above 6 keV and cannot be distinguished from possible noise effects.

Alone, the PCA of the 20 ks-long 2003 epoch is inconclusive. Once the 2003 data is included in the combined 2015 analysis, however, the results are consistent with that of the 2015 PCA (Fig. 3.5). The additional data improve the resolution of the individual components and we see the clear sloped shape of PC 1, this time accounting for $90.8\pm2.3\%$ of the spectral variability. PC 2 is accounting for far less of the fractional variability in this case, at $3.0\pm2.5\%$, however we can confirm that its contribution is located around 5 keV and above – perhaps the source of the slight upturn in residuals

[2]http://www-xray.ast.cam.ac.uk/ mlparker/

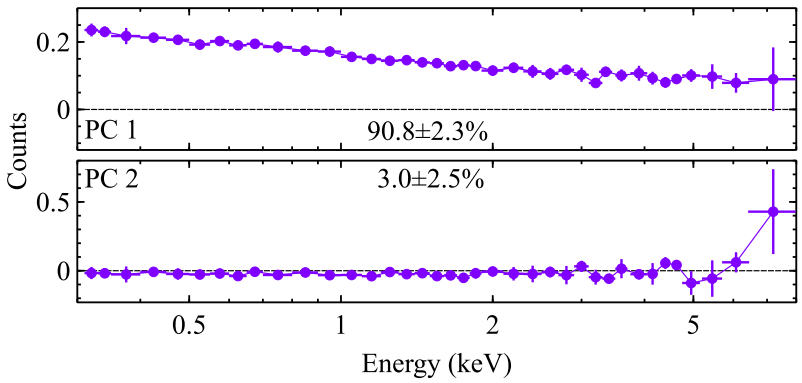

Figure 3.5: PCA normalized spectra of the combined 2003 plus 2015 analysis. Merged-MOS data are shown as an example, as the pn were consistent. Data were binned by 10 ks.

seen in Fig. 3.3. Components 3 and 4 are not statistically significant, both accounting for just a few percent of the spectral variability, but we do see a possible source around 5 keV once again, this time in PC 4.

Comparing Figure 3.5 to simulations in Parker et al. (2015), it seems as though the primary source of both short-term (hours) and long-term (years) variability in Mrk 493 is a change in normalization of some kind. The increased variability in the soft band is consistent with the results of the $F_{\rm var}$ analysis (Section 3.3.1) and even the change in soft-excess as seen in the power law residuals of the 2015 spectra (Fig. 3.3). Whether or not the spectral variability is actually due to the soft-excess alone or perhaps a change in normalization of the primary component – as the linear nature of the PCA would suggest – requires further investigation.

3.4 Average X-ray Spectroscopy

For an initial investigation of the average XMM15a and XMM15b spectra, both epochs were fit individually with MOS parameters linked within each epoch. As the spectra of both epochs are very similar (see Fig. 3.3) and the pn data of XMM15b are truncated at 6.5 keV due to background (see Section 3.2), only XMM15a is discussed in detail.

A power law fit from 2 – 8 keV and extrapolated to lower energies shows a very prominent

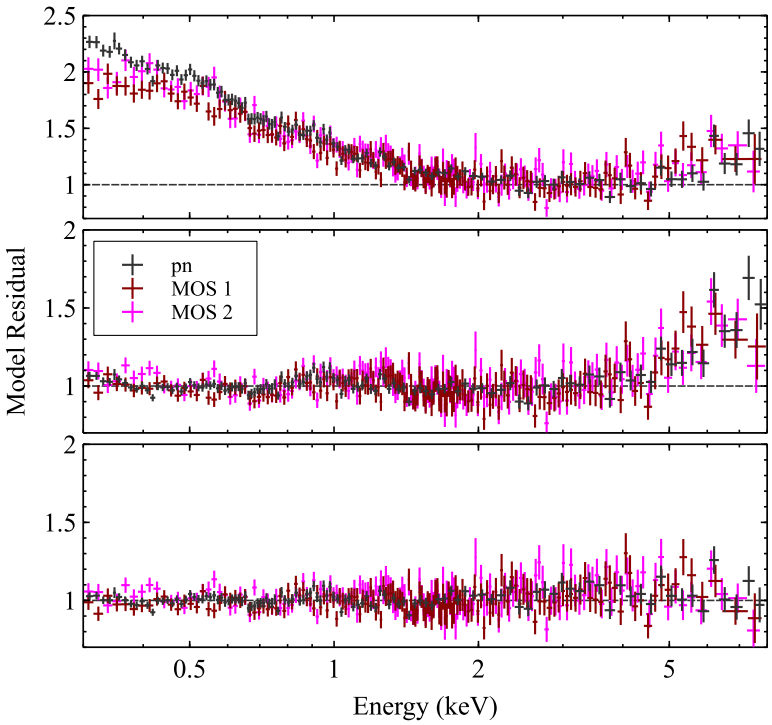

Figure 3.6: Residuals of the toy model fit to XMM15a spectra as an example; the results of XMM15b were consistent. MOS data are red (MOS 1) and pink (MOS 2) while the pn data are grey. A power law fit between 2-8 keV and extrapolated reveals a pronounced soft-excess below $\sim$ 1 keV and positive residuals around 6 keV (Top). The addition of a black body describes the softer spectra well, but large positive residuals remain above 5 keV (Middle). Including a very broad Gaussian profile fixed at Fe Kα 6.4 keV results in the best statistical model (Bottom). Note the different residual scales.

soft-excess below ~ 2 keV and moderate but broad residuals above 5 keV (Fig. 3.6, Top). Including a black body improved the soft-band residuals although the goodness-of-fit remained poor (χ^2 / dof = 1775 / 1544) and the high-end residuals increased (Fig. 3.6, Middle). Adding a Gaussian profile at the intrinsic Fe Kα line energy improved residuals overall and resulted in an excellent ($\Delta\chi^2$= 246 for 6 additional degrees of freedom) fit statistic (Fig. 3.6, Bottom).

Despite the excellent fit statistic and visual appearance of the toy model described above, the Gaussian required was extremely wide, and poorly constrained for XMM15a, in order to account for the broad residuals spanning from 5 keV onward. The upper-limit found for XMM15b $\sigma_{\rm pn}$ is almost certainly due to the truncation of data at 6.5 keV, but that does not explain the widths of all other line fits, the bandwidths of which were not so restricted. Alternatively, if the photon index were fixed at the lower value found from the initial 2 – 8 keV fit ($\Gamma \sim 1.9$ instead of ~ 2.4 from the broad-band fit) the high-end residuals remain moderate and can be well described by a Gaussian of more reasonable width ($\sigma \sim 0.1$ keV). In this scenario, however, the fit statistic is poor (χ^2/ dof = 2336 / 1545) until a second black body is added to account for the now-wider soft-excess ($\Delta\chi^2$= 817 for 6 additional degrees of freedom). This double-black body toy model has an equally good fit statistic as the single black-body model (χ^2_ν / dof = 0.99 / 1541) and comparable residuals. A broken power law was also tested with a single black body and Gaussian, but this version did not describe the data as well as either of the two toy models above.

In essence, we may choose to interpret the 2015 X-ray spectra of Mrk 493 as having either an usually wide soft-excess or an usual "hard-excess" – neither of which can be ruled out based on plausibility alone. Mrk 493 is an NLS1: objects that are known for having very prominent soft-excesses usually attributed to their higher-than-average reflection fractions. Translating the PCA profiles to physical components of an average Seyfert 1 spectrum, we can hypothesize that the 2015 X-ray spectra of Mrk 493 may include a pivoting photon index, a change in normalization of some kind – perhaps also of the primary component, and something that will influence the spectra at energies above 5 keV. Based on the toy modelling, a blurred reflection component is likely given the prominence of the soft-excess and presence of a broad Fe Kα line.

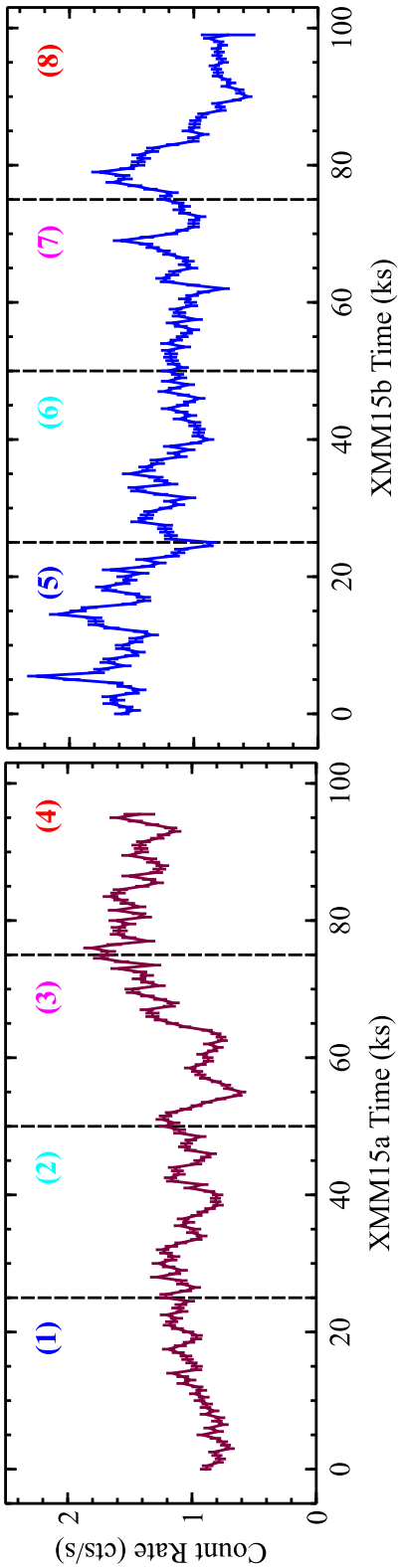

Figure 3.7: Illustration of the light curve divisions for time-resolved analyses of XMM15a (maroon, Left) and XMM15b (blue, Right). Time bins were made such that flux peaks and dips were isolated while keeping the time bins as consistent as possible. The XMM15 spectra were extracted every 25 ks for a total of four time bins per epoch. Time divisions also serve as a rough flux-resolved analysis. Merged-MOS data shown here as an example.

As the purpose of the toy model is simply to act as a preliminary probe into the nature of the X-ray spectra and the model components themselves have no direct physical implications, we will leave this preliminary analysis and continue on to more detailed timing analysis.

3.5 Time-Resolved Analysis

The 2015 X-ray light curves were sub-divided into time bins in order to better understand the rapid variability in Mrk 493 (Section 3.3.1) and the properties of the average spectra (Section 3.4). Both epochs were broken into four 25 ks time segments to capture changes in flux throughout the light curve while keeping roughly equal total counts in each (Fig. 3.7). Both model-independent and model-dependent analyses were completed using these time bins. The EPIC spectra showed consistency between the MOS spectra for both epochs within known calibration uncertainties and so, in an effort to increase signal to noise, the individual MOS 1 and MOS 2 data at each epoch were merged into single spectrum using the FTOOLS program ADDASCASPEC.

Hardness ratios were generated with respect to time utilizing the same 0.35 – 0.5 keV vs. 5 – 8 keV bands as the epoch average analysis in Fig. 3.2. We can more clearly see, now, the differences in spectral softening/hardening in each 25 ks time step: while the XMM15a spectrum is indeed variable, XMM15b shows more steady and significant peaks and troughs in the hardness ratio profile. When comparing to the broadband light curve in Fig. 3.7, it appears that the XMM15b spectrum softens as the continuum brightens and that the sharpest increase in spectral hardening occurs in Bin 8, the very last 25 ks of the entire 2015 campaign.

3.5.1 Time-Resolved Analysis: $F_{\rm var}$

Fractional variability plots of the individual time bins were created for each epoch in the same manner as those from the total light curves (Section 3.3.1) and are shown in Fig. 3.9. The time-resolved $F_{\rm var}$ plots are coloured according to the bin labels in Fig. 3.7 and overplotted for each individual epoch.

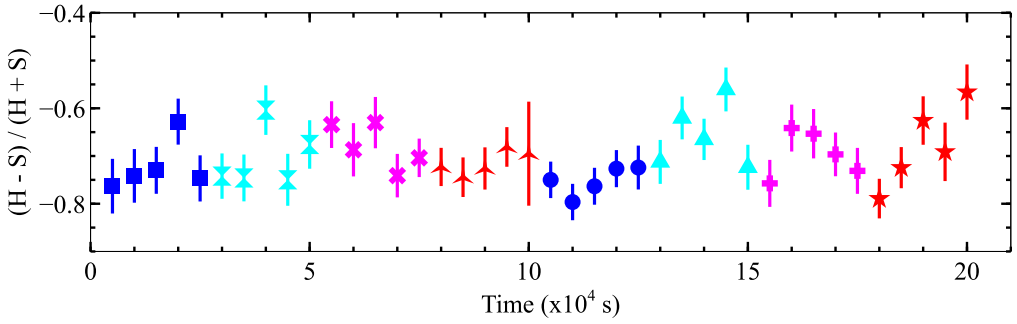

Figure 3.8: Time-resolved hardness ratios for the eight time bins of 2015. The light curves were binned by 5 ks and compare the soft (0.35-0.5 keV) and hard (5-8 keV) bands. Bin 1 (squares), Bin 2 (hour glasses), Bin 3 (crosses), Bin 4 (pinched triangles), Bin 5 (circles), Bin 6 (triangles), Bin 7 (pluses), and Bin 8 (stars) were selected as illustrated in Fig. 3.7 and with consistent colours.

In comparing Figures 3.9 and 3.4, the time-resolved $F_{\rm var}$ are consistent with their epoch-averages: XMM15a has increased variability in the soft band that is nearly averaged out once all time bins are considered. XMM15b average $F_{\rm var}$ retains significant soft-band variability due to the nearly 40% $F_{\rm var}$ below ~ 0.5 keV in Bin 8 (red stars). Consistency with the average $F_{\rm var}$ is encouraging and it is additionally interesting to see when the individual $F_{\rm var}$ profiles change in shape. Variability below ~ 1 keV in XMM15a begins low, increasing to a maximum in Bin 3, and then falls again. In contrast, variability is highest in XMM15b at energies above ~ 2 keV in the first three time bins, with soft variability suddenly increasing dramatically in Bin 8.

The time-resolved $F_{\rm var}$ for the 2015 epochs as a whole shows XMM15a variability is dominated by the intermediate band and the harder energy bands dominating for most of XMM15b. Both the intermediate band in XMM15a and hard band in XMM15b have variabilities reaching $\sim 22 - 36\%$, although the time-resolved $F_{\rm var}$ above 2 keV is more difficult to constrain due both to the higher signal-to-noise and encroaching background in the XMM15b epoch and thus the 5 – 8 keV band as a whole were combined into a single energy bin.

When one compares the timing of strong soft-band variability to the broadband light curves (Fig. 3.7), it appears that the *rate* of soft-band variability increases when the average flux is lowest (i.e. Bin 3 and Bin 8). This is consistent with the time-resolved hardness ratios shown in Fig. 3.8

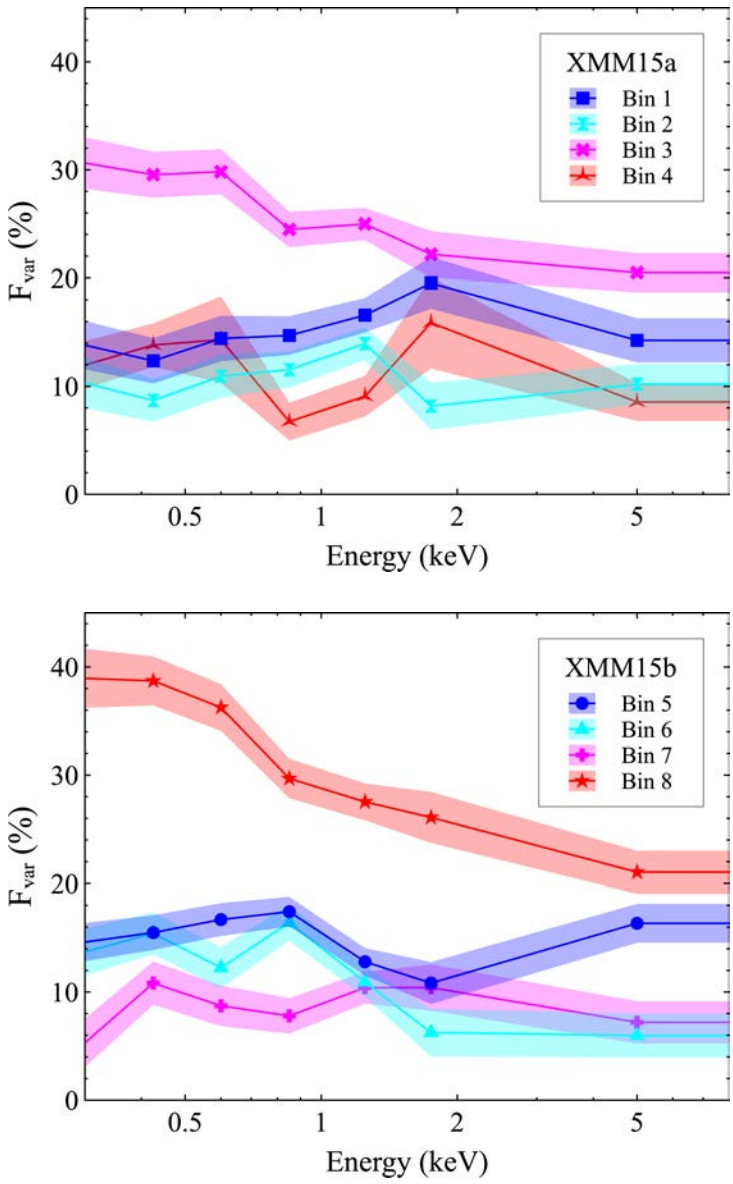

Figure 3.9: Time-resolved $F_{\rm var}$ of the merged-MOS spectra. Light curves were binned by 200 s and coloured bands represent errors calculated following Ponti et al. (2004). Plot labels and colours are consistent with those of Fig. 3.8

in which these bins appear to have the sharpest increase in spectral hardening/softening for their respective epochs. As Bin 8 contains both a sharp increase and decrease in flux, each around 12 ks in length, this time bin was further sub-divided in hopes of isolating instances of highest and lowest flux. Unfortunately, the signal-to-noise was poor for these shorter time segments and no further analysis could be performed.

It is the time-resolved $F_{\rm var}$ that allows us to see the energy-dependent behaviour of the spectra within each time bin. According to the trends seen in Fig. 3.9, we see evidence of multiple modes of variability: one that dominates around ~ 2 keV for most of XMM15a and one that dominates below ~ 1 keV most notably during the last 25 ks of XMM15b. Whether or not these differing $F_{\rm var}$ profiles result from the same source of variability remains to be determined.

3.5.2 Time-Resolved Analysis: PCA

Primary Component Analysis was performed on the time-resolved spectral bins (Fig. 3.7) for all three EPIC instruments. Details on the procedure are the same as those for the epoch-averages and are described in Section 3.3.2, with the exception of the spectral time binning: to account for the shorter timescales involved, after testing various time bin sizes a bin size of 2.5 ks was used instead of the 10 ks of the epoch-average PCA. Results of both MOS 1 and MOS 2 PCA were compared and confirmed to be consistent before merging the data. After comparing the PCA results from individual time bins of each epoch, the spectra of similar time bins were analyzed together in a combined PCA.

The combined PCA of merged-MOS data from XMM15a time bins 1, 2, and 4 are shown in Fig. 3.10 (Left, maroon triangles). Interestingly, PC 1 (33.4$\pm$5.2%) of this new analysis resembles PC 2 of the 2003 + 2015 combined PCA (Fig. 3.5). In addition, the profile of PC 2 (21.2$\pm$3.1%) is similar to PC 1 of the 2003 + 2015 combined PCA: the first two PCs have swapped in order and the dominant source of long-term variability appears to play a secondary role across shorter timescales in the XMM15a observation. While PCs 3 and 4 are marginally significant statistically, they do not have distinct PCA spectral profiles.

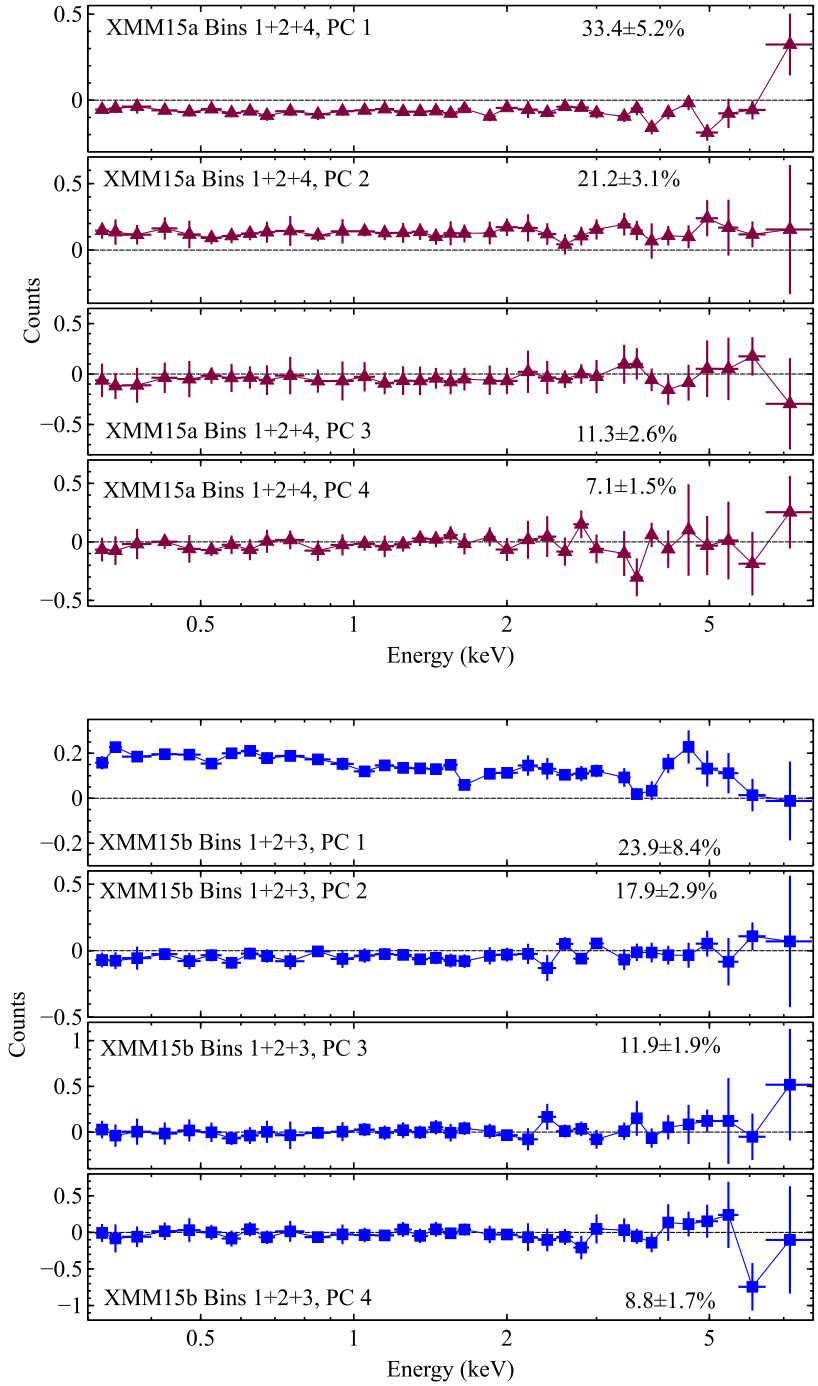

Figure 3.10: PCA performed on the time-resolved spectra of the XMM15a (maroon triangles) and XMM15b (blue squares) observations. Similar time bins were combined into single PCA runs: bins 1, 2, and 4 of XMM15a (Left) and bins 5, 6, and 7 of XMM15b (Right). The first four PCs of both epochs were statistically significant.

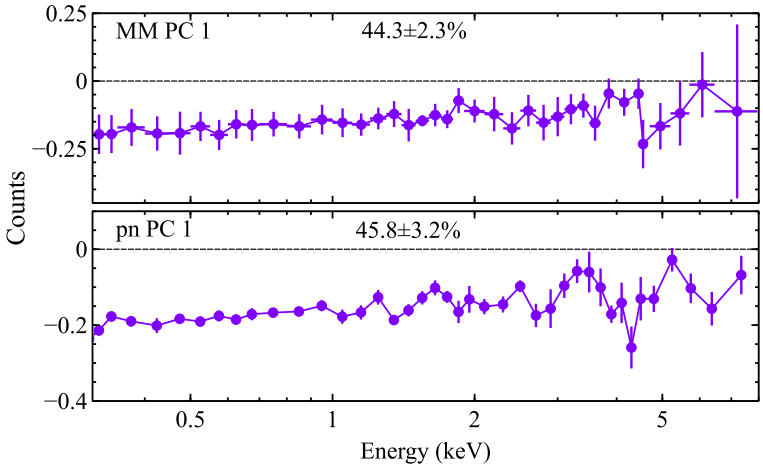

Figure 3.11: Same as Fig. 3.10 but for the unusual bins: Bin 3 and Bin 8. PC 1 is compared between the merged-MOS data (Top) and the pn data (Bottom).

The XMM15b PCA using combined time bins 5, 6, and 7 merged-MOS data are shown in Fig. 3.10 (Right, blue squares). Here, PC 1 (23.9±8.4%) has the most distinctive PCA spectral profile observed thus far, with a strong soft-end variability that approaches zero ~ 4 keV before jumping up again between 4 – 5 keV. Once again, while statistically significant PCs 2 and 3 appear to influence only energies above 7 keV and cannot be distinguished from noise. PC 4 (8.8±1.7%), however, shows a source of variability centred closely around 6 keV and may indicate (weak) short-term variability of the iron line. The pn results of the two previous analyses were also tested and shown to be consistent.

The time-resolved $F_{\rm var}$ of Section 3.5.1 showed that Bin 3 and Bin 8 contain the most variability in the soft band. These two time bins also stand out amongst the rest in their profile shape. Therefore, PCA was run on the combined merged-MOS spectra from both Bin 3 and Bin 8 (Fig. 3.11, Top). Only the first PC was significant in this case (44.3±2.3%), however we once again see the normalization-like profile that also dominated the variability in the PCA of the combined remaining bins of XMM15b. In this instance, despite the lower signal-to-noise, the PC spectral shape is more distinct with a clear dip between 4 – 5 keV. The dip is resolved further in the pn analysis (Fig. 3.11, Bottom) and appears associated with the normalization-like component (45.8±3.2%).

Another model-independent measurement that may be capable of detecting intrinsic changes in the time-resolved X-ray spectra is power spectral density (PSD). PSD functions are a relatively recent (Papadakis et al., 2016) tool that can be applied to analyze X-ray reprocessing in Type I sources and are theorized to show the filtered echo of the primary emission and, therefore, can also be deconstructed to obtain estimates on coronal height (assuming a lamp-post model, see Papadakis et al. (2016) for details). PSDs of the time-resolved spectra were made for the broad 0.3 – 8 keV X-ray band as well as those for narrower bandpasses, including the 5 – 8 keV iron line band. PSDs were also calculated for the average XMM15a and XMM15b spectra and while all results lacked the resolution for robust modelling, they agreed within uncertainty and showed a bent power law break energy of around 10^{-3} Hz and slope of ~ 2 – consistent with average results for Seyfert galaxies in Emmanoulopoulos et al. (2016). There was no differentiation between time bins with the given signal-to-noise.

3.6 Blurred Reflection Scenario

Based on the collective results of the model-independent analyses of Sections 3.3 and 3.5 along with the toy model spectroscopy of the average 2015 data (Section 3.4), we are able to say that long-term (i.e. years) X-ray variability in Mrk 493 is induced by changes in a normalization-like component that may in turn be related to the changes in the soft-excess observed in the average spectra. The short-term (hours to days) X-ray variability, on the other hand, seems far more complex.

It is quite possible that the variability profiles discussed above may in fact be due to changes in a partial covering absorber. Changes in an absorbing body's covering fraction and/or column density can create spectral variability over a range of timescales. Partial covering absorption is well known to reproduce a disk reflection profile by diminishing the continuum flux red-ward of the Fe Kα line (Miller, 2006; Miller et al., 2010) and it is common for Seyfert spectra – especially those of dimmer objects – to be well described by either scenario alone or a combination of both scenarios (e.g. Bonson et al., 2015; Gallo et al., 2013; Marinucci et al., 2014). However, detailed modelling of

both neutral and ionized absorbers by Parker et al. (2014b) determined that such absorption would present itself in PCA spectra as variability at intermediate energies (between $\sim$1 – 4 keV, depending on the characteristics of the absorber involved), such a component is not observed in the PCA of Mrk 493 at any timescale. There have also been no spectral signatures of absorption in Mrk 493 (Section 3.4). While we cannot rule out partial covering as a possible source of variability in this object, we chose to focus on a blurred reflection scenario for the remainder of this work.

Emission from relativistic blurred reflection is expected to be seen in objects in which we have an unobstructed view of the AGN central engine: namely, Type I sources. The primary, non-thermal emission from the corona gets reprocessed by the accretion disk and re-emitted as softer X-rays. Due to the extreme gravitational forces close to the supermassive black hole, light-bending concentrates the isotropic coronal emission toward the inward part of the disk and can increase observed reflected radiation, the combination of which forms the observed soft-excess.

The XMM15a spectra were fit from 0.3 – 8.0 keV for both pn and merged MOS data with a power law plus blurred reflection model. All three EPIC spectra were compared for consistency, but due to background interference the pn will not be discussed further. Disk reflection model REFLIONX (Ross and Fabian, 2005) was utilized modified by the blurring kernel KDBLUR2, which incorporates a broken power law for the emissivity profile. The single blurred reflection model did not explain the data well (χ^2 / dof = 1967 / 1302). Epoch XMM15b was fit from 0.3 – 8 keV for the merged-MOS data and faired only marginally better with the single blurred reflector model (χ^2 / dof = 1313 / 1259). Both epochs showed noticeable positive residuals above 5 keV.

In an attempt to fit the Fe Kα line core, a distant reflector was added to the model. Since the prominent soft-excess is one of the motivations for attempting reflection models, REFLIONX was again used to model the addition of a distant reflector as it has a thorough treatment of atomic features below 2 keV. To describe a neutral, distant reflection source – such as that from a cold torus – the ionization parameter was fixed at $\xi = 1\,\mathrm{erg\,cm\,s^{-1}}$ and the iron abundance set to solar value. The photon index of the power law source illuminating the distant reflector was fixed at Γ = 1.9, the canonical value for AGN (e.g. Nandra and Pounds, 1994). There is no reason to assume that the

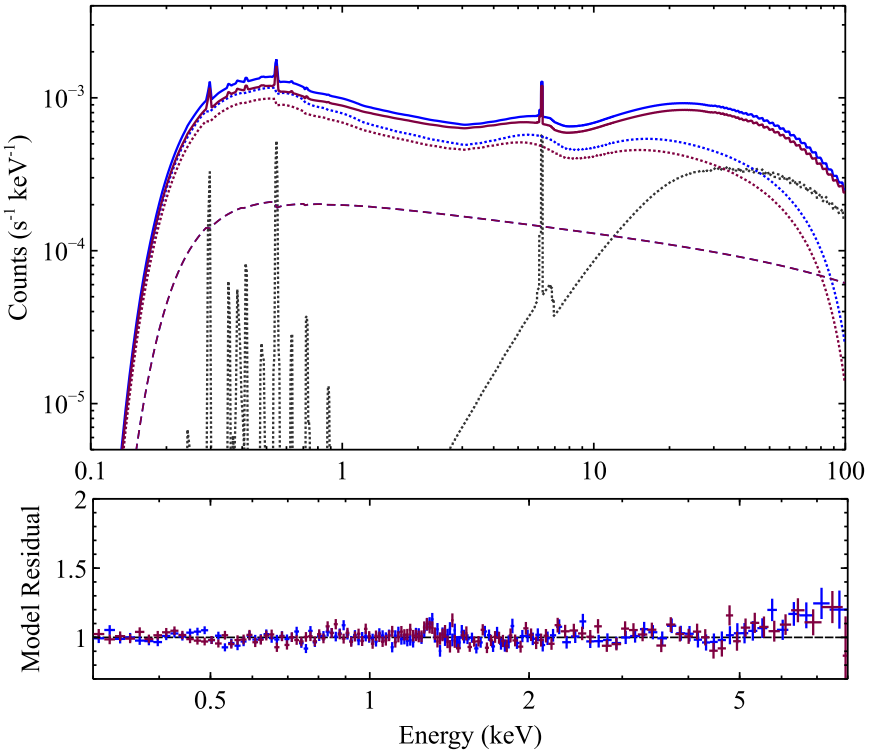

Figure 3.12: Top: The best blurred reflection model simultaneously fit to both 2015 epochs of merged-MOS data. The individual model components of XMM15a (maroon) and XMM15b (blue) are illustrated with dotted (blurred reflection) and dashed (power law) lines. The total model for each epoch is a solid line. The distant reflector is unchanged across the epochs and is therefore not coloured. Bottom: model residuals. Note the different energy scales.

radiation incident on the distant reflector will be the same as that from the primary component and if a value of $\Gamma = 2.0$ was used instead it did not significantly alter the fit statistic.

When the blurred plus distant reflector model was fit to the XMM15a data, the fit statistic greatly improved ($\Delta\chi^2 = 617$ for 4 additional free parameters) and the residuals diminished. The addition of a blurred reflector also improved the XMM15b spectral fits ($\Delta\chi^2 = 26$ for 4 additional free parameters). Adding a second *blurred* reflector, for a combined model of 2×blurred reflector + distant reflector + power law, satisfied both 2015 epochs equally well but did not improve the fit statistic significantly.

Lastly, the single blurred reflector model was applied to both epochs of merged-MOS data and

fit simultaneously with the following parameters linked between epochs: inner disk radius ($R_{\rm in}$), inclination angle (θ), and iron abundance ($A_{\rm Fe}$). The distant reflector was kept linked throughout the epochs. The relativistic blurring application remained the same and the parameters break radius ($R_{\rm br}$) and outer emissivity index (q_2), which are not able to be constrained, were fixed to $10R_{\rm g}$ and 3, respectively.

Both epochs of merged-MOS data are well-described with the single blurred reflector model (χ^2 / dof = 825 / 784) with no prominent residuals (Fig. 3.12). Slight positive residuals remained at the highest energies, and while this is not unexpected due to the high background, the tenacity of this "hard-excess" (see also Section 3.4) makes it seem more likely to be a part of the continuum rather than an artifact of background.

If the primary X-ray components remain linked across the epochs, the fit statistic is consistent (χ^2 / dof = 826 / 786) and the residuals are unchanged. If only the primary components (photon index and power law normalization) are allowed to vary instead, the fit is also acceptable (χ^2 / dof = 839 / 787) although marginally worse and there is no change in residuals. Blurred reflector ionization and normalization were also compared: while unlinked ionization values agreed with each other within uncertainties, linking the two resulted in a marginally worsened fit (χ^2 / dof = 835 / 787). If instead blurred reflector normalization were linked with ionization allowed to vary between epochs, the fit statistic is the same as that from keeping ionization linked (χ^2 / dof = 835 / 787). Thus, it appears a change in both ionization and blurred reflector normalization are required to best explain the average 2015 spectra although generally one can say the spectra are well-described by a lone change in one or the other.

The best blurred reflector model details are listed in Table 3.2. According to the average spectra, the difference in the spectra between XMM15a and XMM15b can be explained primarily by a decrease in disk ionization and/or blurred reflector normalization with possible minor changes in the primary component that are inconclusive when measured only via these epoch average spectra. Both a flux- and time-resolved analysis of these spectra may further clarify the role of the primary X-ray component in Mrk 493.

Table 3.2: The blurred reflection model for the simultaneous fits to the 2015 spectra. Merged-MOS data alone were used and were fit between 0.3–8 keV. Linked parameters are shown with dotted lines. According to this average spectral analysis, the difference in X-ray flux states is due to changes in the blurred reflector primarily.

(1)	(2)	(3)	(4)	(5)
Model Component	Model Parameter	Units	XMM15a	XMM15b
Power Law	Γ		2.14±0.03	...
	model flux	$\mathrm{ph\,cm^{-2}\,s^{-1}}$	$(5.43^{+5.84}_{-2.23})\times10^{-4}$	...
Blurred Reflector	q_1		7.5±1.5	$6.6^{+1.1}_{-2.8}$
	$R_{\rm in}$	$R_{\rm g}$	$1.25^{+0.34}_{-1.25}$	...
	θ	degree	53^{+6}_{-23}	...
	$A_{\rm Fe}$	solar	0.5±0.1	...
	Γ		$\Gamma_{\rm PL,15a}$	$\Gamma_{\rm PL,15b}$
	ξ	$\mathrm{erg\,cm\,s^{-1}}$	1005^{+119}_{-242}	800^{+229}_{-128}
	model flux	$\mathrm{ph\,cm^{-2}\,s^{-1}}$	$(3.29^{+0.29}_{-0.52})\times10^{-3}$	$(3.79^{+0.33}_{-0.53})\times10^{-3}$
	R ($R_{\rm ref}$ / $R_{\rm pl}$)		2.58±0.09	3.63±0.07
	Fit Statistic	χ^2/ dof = 825 / 786	χ^2_ν = 1.05	

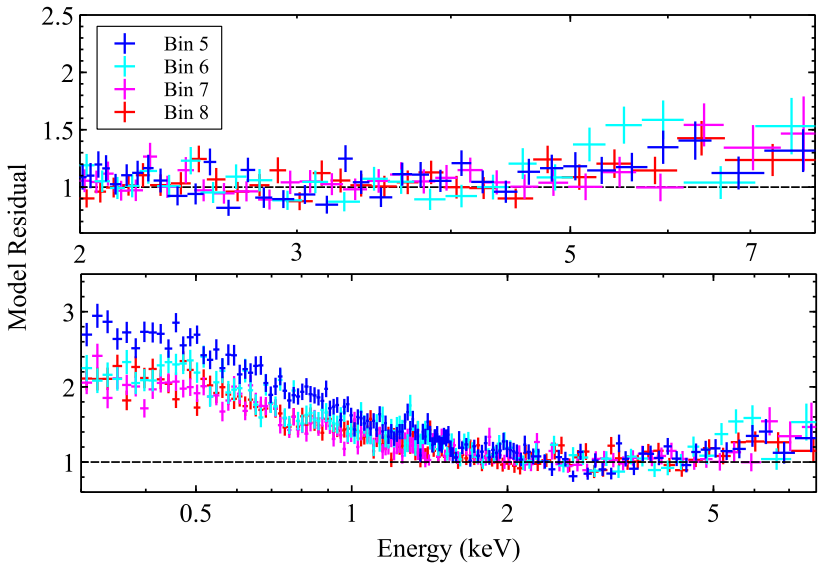

Figure 3.13: Model residuals from a power law with normalization allowed to vary fit to the time-resolved spectra of XMM15b, between 2–8 keV (Top) and extrapolating to lower energies (Bottom). Colours correspond to the time bins shown in Fig. 3.7.

3.6.1 Time-Resolved Spectroscopy

A power law fit to the time-resolved spectra of XMM15b between 2 – 8 keV while keeping normalization free to vary (Fig. 3.13, Top) and then extrapolated to lower energies (Fig. 3.13, Bottom) reveals changes in the soft-excess and Fe Kα line that were not apparent in the average spectrum. We see Bin 5 having the largest soft-excess and that of the following three remaining relatively consistent. The Fe Kα line also appears significantly broader in Bin 6 compared to the others.

The best blurred reflection model from the average spectral fits (Section 3.6) was next applied to the time-resolved spectra of XMM15b. The primary emitter was allowed to vary between time bins as well as the parameters for inner emissivity index, inclination, ionization, iron abundance, and the normalization of the distant reflector. Inner disk radius was set to $1.24R_{\rm g}$, the value found from the average spectral fits, and break radius to $10R_{\rm g}$. This preliminary fit described the data very well (χ^2/dof = 956 / 955), although there were noticeable residuals above $\sim$2 keV for the first two

bins in particular.

As the photon index did not vary greatly after Bin 6, it was linked between bins 6, 7, and 8. It should be noted that in an effort to quantify the effect of a variable Γ, the F-test was applied comparing a free Γ between all 8 time bins. Only the transition between bins 5 and 6 justified an unlinked Γ with a p-value of 0.3% (assuming the model is correct), however neither the chi-squared fit statistic nor individual error estimates on these values justify allowing Γ to be free.

If power law normalization were linked as well in the last three bins, the fit statistic did not change although there was slightly more spread in the residuals around 0.5 keV. Therefore, power law normalization was allowed to continue to vary across all time bins. Blurred reflector ionization and inner emissivity index were then freed between all time bins as well. These changes resulted in an equally good fit statistic (χ^2/dof = 955 / 951) and reduced residual scatter overall, despite some positive residuals remaining above ~ 6 keV.

We expect the inner emissivity index to be somewhat difficult to measure spectroscopically without increased signal-to-noise (Bonson and Gallo, 2016) and so the precise values of this parameter were taken as upper-limits. The break radius will also change with emissivity index, however this parameter proved even more difficult to constrain than inner emissivity index and so it was fixed at $10R_{\rm g}$ and linked throughout the process. If the inner disk radius was allowed to vary while remaining linked throughout the time bins, the fit statistic did not improve and thus was left fixed at the average fit value of $1.24R_{\rm g}$.

It should also be noted that the blurred reflector normalization and ionization are degenerate in this case (see Wilkins and Gallo, 2015b, for review). With no other prominent atomic features to constrain the ionization parameter, it acts essentially as the normalization within this limited bandpass by increasing or decreasing the reflection continuum flux as needed. There is no significant change to the model fit statistic if the blurred reflector normalization were free to vary instead of ionization, nor if both were free to vary together. We do expect ionization to increase (decrease) with an increase (decrease) in incident (i.e. primary) emission as well as a steepening (flattening) of the inner emissivity index, and so we allow ionization to vary instead of blurred reflector normalization.

In all subsequent model fits, blurred reflector normalization was tested as well, but as it was indistinguishable from ionization in all cases we will not discuss it further.

Especially of note is that Bin 5 does not require a primary component, with a power law normalization consistent with zero, and is well-described by blurred plus distant reflection alone. The primary component is significant in Bin 6 and remains so for the rest of the epoch. This suggests that the reflection fraction is much higher in the beginning of XMM15b and perhaps corresponds to the higher total flux during this time bin – consistent with the higher soft-excess seen in the initial power law extrapolation. This may also explain the inconsistencies in Γ analysis discussed above: if the reflection fraction is high enough to wash out the primary component, we would not expect to be able to estimate a change in Γ across time bins.

Extending the model to simultaneously fit the entire 2015 dataset, blurred reflection describes the spectra best when power law normalization, inner emissivity index, and disk ionization continue to vary between time bins (χ^2/ dof = 1945 / 1899). Photon index also changes slightly between XMM15a and XMM15b (2.10 to 2.15, respectively). Overall, a blurred reflection scenario attributes the short-term (~ 25 ks) spectral changes as being due predominantly to changes in ionization of the disk and only minor changes in the primary component. Between Bin 5 and Bin 6, we see a significant increase in flux of the primary component which then varies only subtly throughout the rest of the observation.

3.6.2 TRS: MCMC simultaneous modelling

The blurred reflection model was then used to fit all time bins of the two epochs of observations simultaneously in order to test if long-term changes across the epochs were consistent. A Markov Chain Monte Carlo (MCMC) method was used via an open-source EMCEE algorithm developed by Foreman-Mackey et al. (2013) utilizing the original algorithm of Goodman and Weare (2010). The XSPEC-friendly program, XSPEC_EMCEE, was developed by Jeremy Sanders and is publicly available.[3]

[3] https://github.com/jeremysanders/xspec_emcee

Table 3.3: MCMC error estimation of the blurred reflection model. Columns list: epoch of observation (1), time bin number (2), duration of bin (3), photon index (4), power law flux from 0.1–100 keV (5), inner emissivity index (6), ionization parameter (7), blurred reflector flux from 0.1–100 keV (8), and reflection fraction from 0.1–100 keV (9). Parameters that remained linked (with uncertainties) or fixed (no uncertainties) throughout the fitting are listed in the final row along with fit statistic.

(1) Epoch	(2) Time Bin	(3) Bin Duration (ks)	(4) Γ	(5) $PL_{\rm flux}$ (x10^{-4}) (ph cm^{-2} s^{-1})	(6) q_1	(7) ξ (erg cm s^{-1})	(8) $BR_{\rm flux}$ (x10^{-3}) (ph cm^{-2} s^{-1})	(9) R (R_{ref} / R_{pl})
XMM15a	1	25	2.23±0.04	$7.48^{+0.20}_{-0.21}$	$7.4^{+1.5}_{-1.1}$	335^{+48}_{-34}	$6.42^{+0.36}_{-0.34}$	0.86±0.01
	2	25	2.19±0.03	$7.86^{+0.20}_{-0.21}$	$8.4^{+1.0}_{-1.2}$	363^{+53}_{-36}	$6.35^{+0.36}_{-0.35}$	0.81±0.01
	3	25	2.12±0.03	$5.24^{+0.23}_{-0.22}$	$8.8^{+0.9}_{-1.1}$	550^{+60}_{-43}	$9.14^{+0.36}_{-0.38}$	1.74±0.01
	4	24	2.14±0.03	$3.44^{+0.37}_{-0.38}$	$7.6^{+1.0}_{-1.0}$	871^{+71}_{-96}	$16.76^{+0.58}_{-0.56}$	4.87±0.01
XMM15b	5	25	2.23±0.02	$3.51^{+0.43}_{-0.44}$	$7.8^{+1.0}_{-0.9}$	1021^{+41}_{-20}	22.05±0.64	6.28±0.01
	6	25	2.07±0.03	1.45±0.30	$6.6^{+1.1}_{-0.7}$	766^{+38}_{-53}	13.87±0.48	9.59±0.01
	7	25	2.14±0.03	$6.63^{+0.24}_{-0.23}$	$7.0^{+1.3}_{-1.0}$	501^{+41}_{-31}	$8.58^{+0.38}_{-0.41}$	1.29±0.01
	8	24	2.11±0.03	4.14±0.22	$7.2^{+1.1}_{-0.9}$	555^{+64}_{-43}	9.74±0.37	2.35±0.01
All Epochs	all bins	n/a	$R_{\rm in}$ ($R_{\rm g}$)	θ (degree)	q_2	$A_{\rm Fe}$ (solar)	χ^2/dof	
			$1.56^{+0.08}_{-0.09}$	55±2	3.0	0.6±0.1	1960 / 1934	

The MCMC fitting was run with 76 walkers and 10,000 iterations. The best-fit parameter values from the manual fitting of Section 3.6.1 were used as the peak of the MCMC probability distributions and the errors were from the widths of those distributions. The first 1000 steps were burned to ensure truly random initial conditions. Only photon index, power law normalization, blurred reflection ionization, and the inner emissivity index were unlinked and allowed to vary throughout the entire dataset. Inner emissivity index was difficult to constrain in the manual model fits (Section 3.6.1); however, we were optimistic in the ability of the MCMC process to better constrain the upper limits of the manual fits and allowed this parameter to remain free. The manual fitting also did not require the photon index to vary across most time bins, although an F-test indicated of a potential change in Γ in XMM15b motivated us to allow photon index to vary here. Inclination angle and iron abundance were linked throughout across all datasets, but allowed to vary. The flux of the power law and that of the blurred reflector were calculated between 0.1 – 100 keV for each fit result in an attempt to track reflection fraction (R) as well. The results of the MCMC approach are outlined in Table 3.3 and component fluxes are shown in leu of normalization for clarity. It should be noted the parameter central values and fit statistic listed here correspond to a *manual fit assessment* performed separately as a consistency check and thus can be adopted as the true model values.

Time series were created for a visual inspection of the main parameters and the evolutions of inner emissivity index, ionization, photon index, and power law normalization are illustrated in Fig. 3.14. The individual time bins are coloured in accordance with Fig. 3.7 and the unusual time bins from the time-resolved $F_{\rm var}$ study (Section 3.5.1) are highlighted in yellow. We see that while inner emissivity index remains relatively constant within model constraints, the other three parameters show significant variability across the 25 ks time bins. Disk ionization more than doubles between the start of XMM15a and the start of XMM15b, before dropping again in roughly parabolic fashion to nearly its starting values. Power law normalization shows an opposite trend to that of disk ionization: dropping from its starting value to a minimal value in Bin 2, before climbing once again. Photon index remains relatively constant within uncertainty for XMM15a, but shifts significantly within the later epoch – in agreement with the PCA results of Section 3.3.2.

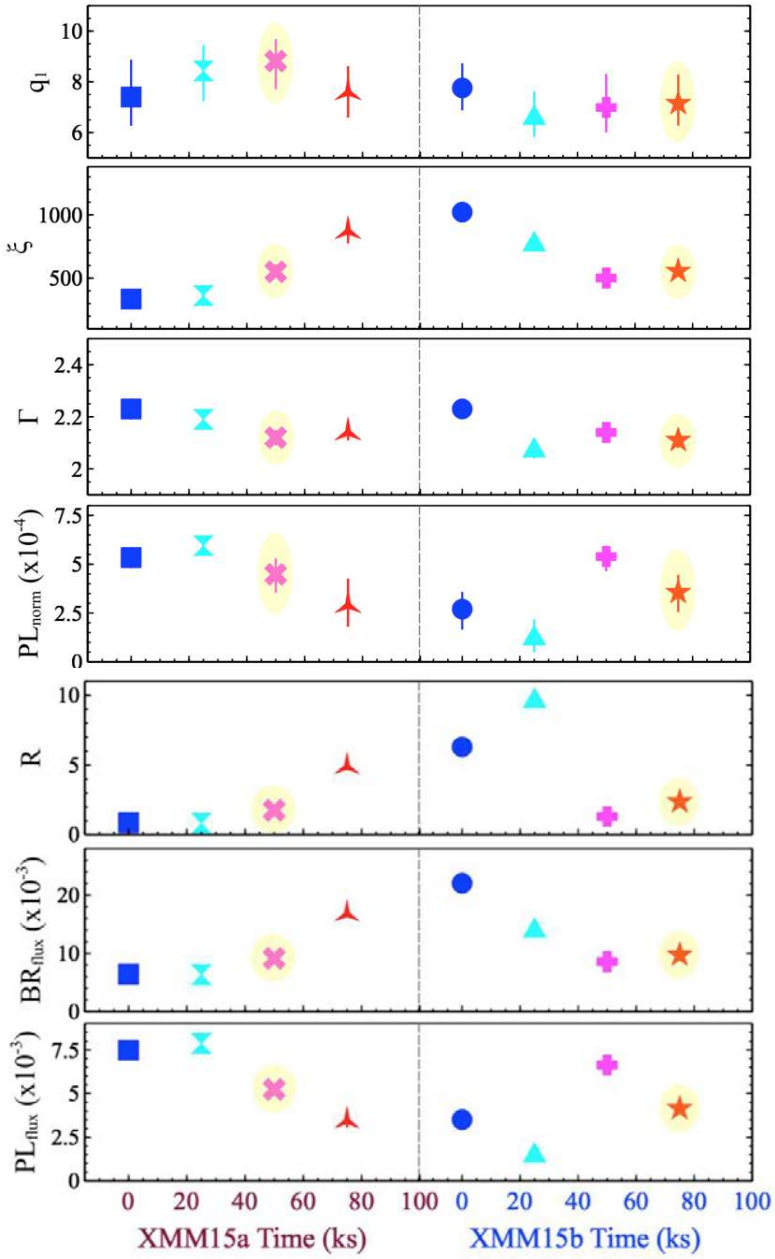

Figure 3.14: Trends extracted from the simultaneous epoch fitting of time-resolved spectra via MCMC using the blurred reflection model. Parameter details are shown in Table 3.3. XMM15a data (triangles) and XMM15b data (squares) are coloured correspond to the time bins shown in Fig. 3.7. The two time bins with more unusual $F_{\rm var}$ profiles as seen in Fig. 3.6.3, Bin 3 and Bin 8, are highlighted in yellow.

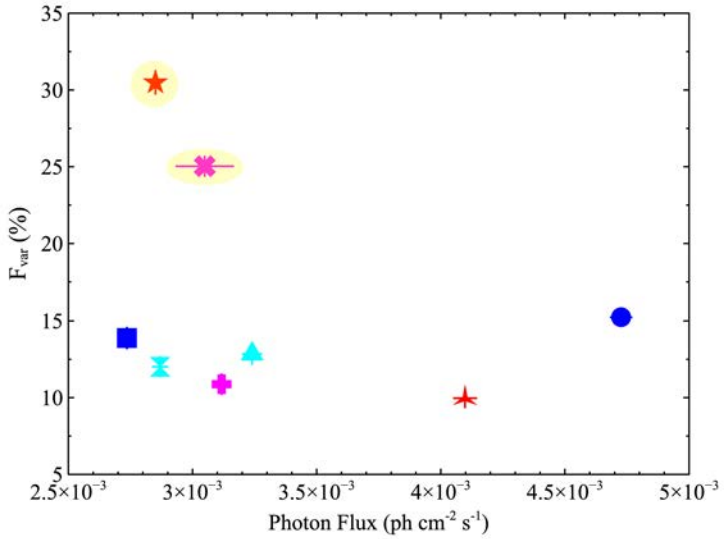

Figure 3.15: Average 0.3–8.0 $F_{\rm var}$ per time bin as a function of photon flux in the same band. Colours correspond to the time bins shown in Fig. 3.7 and the two time bins with more unusual $F_{\rm var}$ profiles, as seen in Fig. 3.6.3, are highlighted in yellow.

Of real interest is a measurement of reflection fraction (R) over time or how the ratio between blurred reflection flux and power law flux varies. Type I Seyfert galaxies can have high reflection fractions as more of the innermost emission is able to escape unabsorbed from the central engine (Fabian et al., 2012; Wilkins and Gallo, 2015b) and NLS1s can be the most extreme examples of these, with reflection fractions climbing to 10 or more in some objects. Based on the results of the initial model-independent analysis (Section 3.3) as well as the subsequent spectroscopy (Sections 3.4 and 3.6.1), we expect Mrk 493 to be reflection dominated as well. This does appear to be the case overall, with all but the first 50 ks of the 2015 observations having $R > 1$ (see also column 9 of Table 3.3). Reflection fraction roughly follows the trend seen in blurred reflector flux and disk ionization.

The average $F_{\rm var}$ per time bin as a function of 0.3 – 8.0 keV flux was also calculated and is shown in Fig. 3.15. The two unusual time bins, Bin 3 and Bin 8, clearly stand out as having the most average spectral variability within 25 ks. This is consistent with the average continuum flux as seen in the broadband light curve.

The detailed time-resolved spectroscopy bolster previous analyses that point to changes in a blurred reflector as the primary source of variability in Mrk 493 during the 2015 observations. We see that disk ionization in particular appears to be responsible for most of the variability on time scales of ~ 25 ks with the addition of the primary X-ray component contributing as well via changes in the photon index. Aside from the spectroscopy, evidence of primary component changes only appear in the average PCA and not in the $F_{\rm var}$, flux-flux analyses, nor hardness-ratio tests. Perhaps changes in the primary source can only clearly be seen under these finer time bins because behaviour across longer time scales (days) are averaged out.

3.6.3 Time-Resolved $F_{\rm var}$ Modelling

It would be useful to see the shape of fractional variability profiles produced by different spectral models, independent of the data. Therefore, one hundred simulated spectra were produced using the best blurred reflection model developed in Section 3.6. By simulating $F_{\rm var}$ profiles in this way, we lose the model-independent aspect of the analysis. However, we hope to elucidate the more complex and codependent nature of the variable parameters using this approach.

The blurred reflection model described in Table 3.2 was used as a model template for generating simulated spectra in the same manner as described originally in Section 3.5.1. One at a time, the photon index (Γ), power law normalization ($PL_{\rm n}$), and disk ionization (ξ) parameters were randomly varied. As before, $F_{\rm var}$ analysis was then performed on the three sets of simulated spectra to produce the models which were then scaled and overplotted onto the time-resolved $F_{\rm var}$ data.

We now see, when the entire self-consisted broad-band model is taken into account, there is a clear difference in $F_{\rm var}$ profile shape between $PL_{\rm n}$ and ξ (Fig. 3.16, Middle and Bottom rows): the former dominates at intermediate energies while the latter peaks below 0.5 keV and declines linearly thereafter. It is now clear that changes in ξ create an $F_{\rm var}$ profile that most closely resembles Bin 3 and Bin 8 – the standout time bins for their significantly higher soft-band variability. This is consistent with the PCA produced by these two bins (Fig. 3.11) that resembles a change in normalization with most variability at softer energies. In reality, a combination of changing

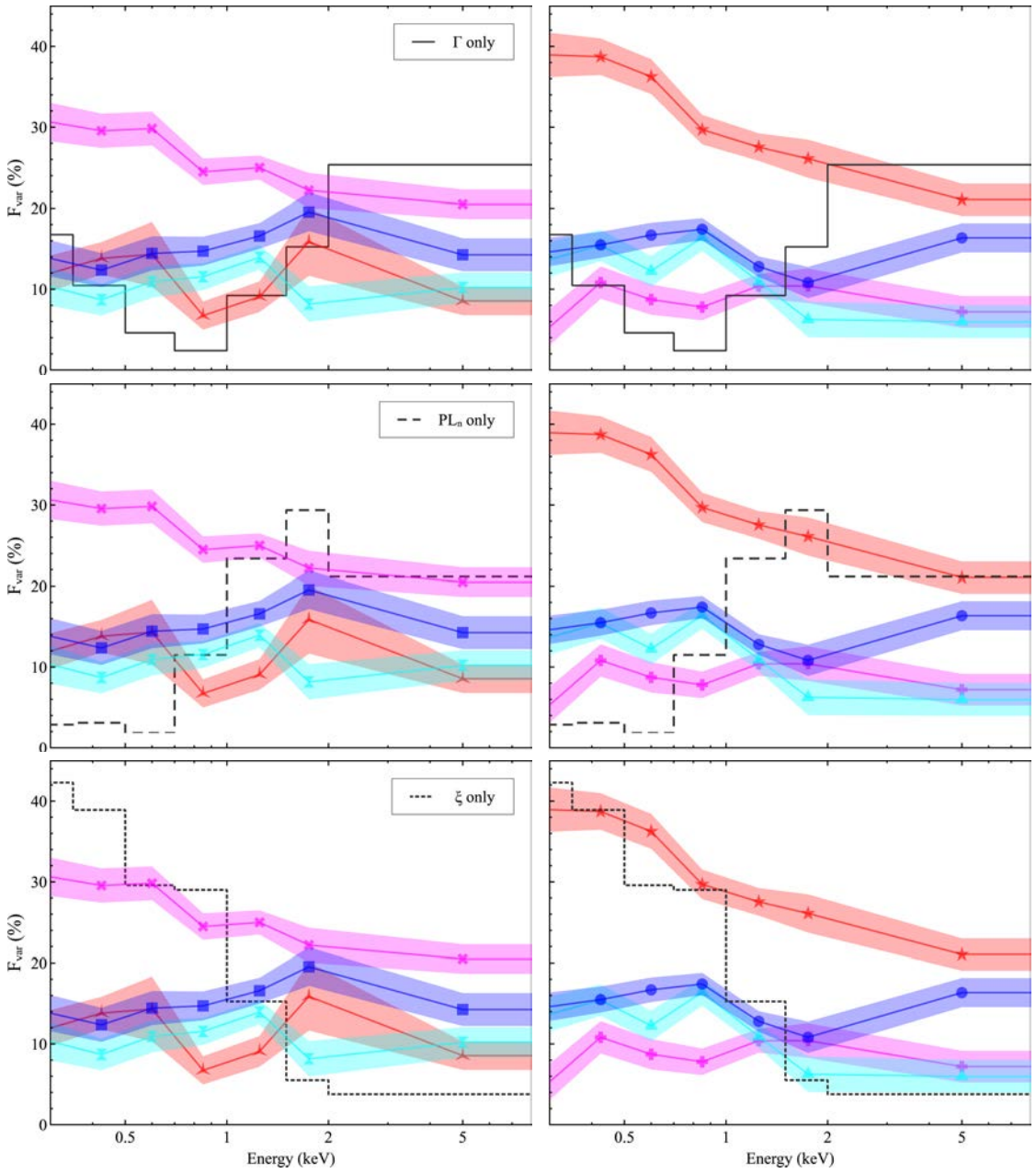

Figure 3.16: Same as Fig. 3.9 but with simulated $F_{\rm var}$ profiles (grey lines) produced using the best blurred reflection model. Changes in photon index (Γ, solid), power law normalization ($PL_{\rm n}$, dashed), and disk ionization (ξ, dotted) were simulated individually.

parameters would most likely account for the data profiles seen here.

3.7 Discussion

Short term ($\sim$25 ks) X-ray variability in Mrk 493 has proven to be more complex than initial observations of this object would suggest. Its average 2015 X-ray spectra appear quite standard, for even very pronounced soft-excesses are commonly seen in narrow-line Seyfert 1 galaxies, and it is only through more detailed timing studies that the remarkable nature of Mrk 493 emerges.

The PCA studies probe variability on both 10 ks and 2.5 ks timescales across light curve observations spanning $\sim$ 7 hrs (Section 3.3.2) to $\sim$ 10 yrs (Section 3.5.2). The results consistently show a source of variability that resembles a change in normalization of some kind. It is interesting to note that when examining the shortest timescales *without* the unusual time bins (Bin 3 and Bin 8), we see a change in the primary component between the first and second half of the 2015 observations. The first half of 2015 is dominated by variability almost exclusively above 6 keV and the normalization-like component that was prominent in the 2015 and combined 2003 + 2015 epoch-averaged PCA appears to play a secondary role. The second half of 2015 is dominated once again by the normalization-like component, which remains the primary source of variability in the combined PCA of the unusual time bins and it is through these that we may begin to connect the dots.

Bin 3 and Bin 8 stand out in both the time-resolved spectroscopy (Section 3.6.1) and fractional variability (Section 3.6.3). According to the $F_{\rm var}$ modelling comparison, both of these time bins are well described by changes in disk ionization. However, the disk ionization model does not describe the data well above $\sim$ 2 keV – where power law normalization is more consistent. One can imagine that, in reality, both the primary emitter and blurred reflector are changing across the observations and time-resolved analyses pick up on the more dominant source of variability within each time bin. Based on evidence presented by the time-resolved spectroscopy, we can say that the primary component drives most of the variability in the first half of the 2015 observation with changes to

both photon index and power law normalization. In the second half of the 2015 observation, we see the blurred reflector begin to drive the variability while remaining correlated with the primary component (Fig. 3.14). The usual bins appear at times of moderate parameter values – neither highest nor lowest observed – and thus may indeed be moments of highest rate of variability as the source transitions from a more primary-driven state to a state of more active blurred reflection.

This scenario is in agreement with known empirical relationships: we see Γ steepen as $PL_{\rm n}$ increases, R grows with increasing $BR_{\rm flux}$, as does ξ. We must be careful in how we relate the time-resolved $F_{\rm var}$ to the spectroscopy studies, however. It is important to stress that the time-resolved $F_{\rm var}$ plots depict the variability *within* each 25 ks time bin and not *between* each bin, as the time-resolved spectra (Fig. 3.13) and time series (Fig. 3.14) illustrate. Attempts to resolve both the spectra within shorter timescales to make a more direct comparison to the $F_{\rm var}$ results were unsuccessful due to high background.

Unlike the other relationships noted above, we do not observe a correlation between $PL_{\rm n}$ and ξ. It is reasonable to anticipate an increase in ξ as incident radiation onto the disk increases via rising $PL_{\rm n}$, although there has been an instance where this is not observed (Gallo et al., 2015). A lack of correlation may indicate changes in the geometry of the primary source so that incident radiation onto the disk decreases even as $PL_{\rm n}$ itself grows or perhaps there are intrinsic changes in the disk that would increase ξ without the need of more ionizing radiation. Indeed, if the blurred reflection scenario is correct, then the behaviour of the blurred reflector in this object does appear to be puzzling.

The ionization of the blurred reflector most heavily influences the variability during the 2015 observations, driving the soft-excess to jump/dip in flux by as much as 50% over the course of the observations. During the time of highest flux (first 50 ks of XMM15b), the spectrum is heavily dominated by blurred reflection. The primary component normalization moderately varies no greater than 40% during the 2015 observations and photon index varying at most $\sim 10\%$ during the first half of XMM15b – suggesting any such pivoting action is overshadowed by changes in normalizations of both the primary and reflection components. This is in agreement with the time-resolved PCA,

which assigns the primary PC to a normalization-like source.

Changes in ionization would cause nearly-uniform variability across the 0.3 – 8 keV X-ray band with minimal influence on the Fe Kα line as long as the ionization overall is high – which appears to be the case (Sections 3.6, 3.6.1, and 3.6.2). The change in the Fe Kα line remains an open question, however. We first note the change in Fe Kα during time-resolved spectroscopy, when the line abruptly changes *after* a drop in soft-excess flux in XMM15b (Fig. 3.13). Then, in the time-resolved PCA, we see a principal component influencing energies between 4 – 5 keV most prominently during the unusual time segments Bin 3 and Bin 8.

We note that positive residuals remain when spectra of XMM15b are fit with the blurred reflection model. These excess residuals were assumed to be due to the background that overtakes the source at 8 keV, but could in fact be due to a missing spectral component. The 4 – 5 keV source of variability seen in the PCA analyses also hint at a source of variability thus far unaccounted for. It is important to stress that no additional spectral component, reflection or otherwise, was required by the blurred reflection model fit to either the average epoch or time-resolved spectra and attempts at reverberation lag analysis were inconclusive due to limited signal-to-noise. However, the growing evidence of another emission source in addition to the standard blurred plus distant reflection motivates further robust statistical applications and is addressed in detail in Chapter 4.

3.8 Conclusions

In this summary, we determined the characteristics of the X-ray continuum of Mrk 493 by analyzing both the long- and short-term variability of this object with an emphasis on model-independent techniques. Data from *XMM-Newton* merged-MOS instruments were primarily utilized due to background interference in the pn at lower energies, although the pn data were processed alongside all investigations to confirm results. The most significant conclusions are as follows:

- Long-term (years) X-ray variability appears to be driven by changes primarily in blurred reflector normalization/ionization. With the limited exposure time of the 2003 observation

(XMM03), more detailed analyses could not be performed on this epoch alone.

- Variability on intermediate time scales (weeks) was studied using the two consecutive 2015 observations and showed a change in the primary source of variability between the first half of 2015 and the second.

- Fractional variability ($F_{\rm var}$) from the average light curves of both 2015 epochs showed the latter half of 2015, XMM15b, to be the most variable with around 30% variability below 1 keV.

- Principal component analysis (PCA) performed on the average light curves in all three epochs (XMM03, XMM15a, and XMM15b), both individually and combined, detected a primary source that was linear with a slight rise toward the softest energies – indicative of a kind of normalization. Other statistically significant principal components were detected although their PC spectral profiles were not well resolved and their characteristics could not be determined with the epoch-average PCA alone.

- Time-resolved $F_{\rm var}$ revealed significant changes in the variability profiles of both 2015 spectra across 25 ks timescales. Most time bins of XMM15a peaked in variability around 2 keV whereas those of XMM15b peaked above 2 keV. However, there were two time bins, one from each epoch, that were unlike the others and showed strong ($\sim$40%) soft-band variability below $\sim$ 1 keV. These two unusual time bins, XMM15a Bin 3 and XMM15b Bin 4, were monitored closely in the following analysis.

- Performing PCA on combined time bins confirm the bullet points above. XMM15a bins 1, 2, and 4 were processed together and separately from XMM15b bins 1, 2, and 3. These results confirmed that the primary source of variability changed between the first and second half of the 2015 observations: dominating above 6 keV in XMM15a and appearing normalization-like in XMM15b.

- PCA performed on the combined unusual time bins confirmed a normalization-like source of variability with a now significant source of variability also apparent between 4 – 5 keV.
- Time-resolved spectroscopy revealed that the soft-excess drops significantly after the first 25 ks of XMM15b followed 25 ks *later* by a drop in emission above 4 keV. Simultaneous fitting of all time bins of the two 2015 epochs together via MCMC support changes in the blurred reflector, specifically disk ionization, as the primary source of short-term variability. Changes in the primary component, specifically normalization, produced variability on a smaller scale. We see a significant increase in ionization correspond to times of highest average flux.
- A modelling of the time-resolved $F_{\rm var}$ analysis using the best blurred reflection model highlighted XMM15a Bin 3 and XMM15b Bin 4 as being unique. The variability in these two bins appears to be driven primarily by changes in ionization, in contrast to all other time bins which appear to be driven by changes in primary component parameters. Tracking these two unusual bins in a variety of parameter spaces we see that they always fall around intermediate parameter values: neither at minima nor maxima. This suggests that the rate of change in ionization increases during transition periods between highest and lowest average flux.

In conclusion, the primary source of X-ray variability in Mrk 493 is most likely due to changes in the blurred reflector and changes in disk ionization specifically. We once again note that ionization can replicate the behaviour of blurred reflection normalization, especially when ionization values are high, and further work would need to be performed on data with multiple atomic features before a robust distinction between disk ionization and blurred reflector normalization can be made. With that said, changes in disk ionization describe the X-ray data from three separate epochs well on both longer and shorter timescales.

At shorter timescales, the behaviour of variability becomes more complex and we see evidence that changes in the primary component – more specifically, power law normalization – dominates at different times. XMM15a appears to have a more balanced reflection fraction while XMM15b

experiences greater changes in R. There is also an unusual miscorrelation between the soft-excess and broad iron line in the XMM15b spectroscopy that is as of yet unexplained.

Mrk 493 has proven to be an object of spectral complexity and may become a hidden gem among AGN for its unusual X-ray variability. Continued, multi-band monitoring of Mrk 493 would reveal the true nature of its short-term variability and may also catch it should it return to the flux levels seen in 2003.

Acknowledgments

The authors would like to thank A. G. Gonzalez and H. Ehler for thoughtful brainstorming sessions. The *XMM-Newton* project is an ESA Science Mission with instruments and contributions directly funded by ESA Member States and the USA (NASA).

Chapter 4

Investigating the Source of Unexplained X-ray Variability in Mrk 493

The work in Ch.3 & Ch.4 are being prepared as one manuscript for publication in the Monthly Notices of the Royal Astronomical Society.

4.1 Introduction

Central engines of active galactic nuclei (AGN) are fundamentally composed of the supermassive black hole, its surrounding accretion disk, and a corona of hot ($\sim 10^9$ K) electrons in some configuration above the two. As black holes themselves are defined in nature only by their mass and angular momentum[1], the properties of the disk and corona play essential roles in determining the overall behaviour of the AGN itself. While coronal geometry appears to be influential, particularly in the X-ray regime (e.g. Done et al., 2012; Wilkins, 2016; Gonzalez et al., 2017), it too is described almost entirely by two properties: coronal density and temperature. By comparison, the accretion disk is more complicated. Even under the standard "thin disk" Shakura-Sunyaev formulation (e.g. Shakura and Sunyaev, 1973; Novikov and Thorne, 1973; Penna et al., 2012) changes in properties such as line-of-sight inclination, iron abundance, and location of the inner radius can greatly influence an AGN's X-ray spectrum (Bonson et al., 2015).

The nature of accretion disks has been a topic of great interest for the astronomical community in general, having application in the study of high-mass binary systems, stellar formation, and black hole binary systems in addition to AGN. It is in the lower-mass objects that we have the opportunity to observe disks directly due to both the higher intrinsic disk temperature ($T_{disk} \propto \mathrm{M_{BH}}^{-\frac{1}{4}}$) and shorter evolutionary timescales (i.e. within observable lifetimes). Through such observations, we have seen just how diverse accretion disks can be: possible disk scenarios range from those that are radiatively efficient, optically thick, and geometrically thin (i.e. thin disks); to those that are radiatively inefficient and two-dimensional (i.e. "slim disks", see Sadowski & Aleksander 2009 and Sadowski et al. 2011 for review); to lastly those that are advection-dominated, optically thin, and nearly spherical ("ADAFs", see Narayan & McClintock 2008 for review).

The kind of accretion disk a black hole possesses depends predominately on accretion rate although accretion mechanism (i.e. steady vs. chaotic), black hole spin, feedback (radiative and/or mechanical), and magnetohydrodynamical effects all play a role in the ultimate characteristics of the

[1] Black hole electric charge appearing to reside predominantly in the mathematical regime.

disk (e.g. King and Pringle, 2006; Jiang et al., 2014; Castello-Mor et al., 2016; Muñoz-Darias et al., 2016). Observations of stellar-mass black holes in active binaries have revealed that a disk evolves through multiple states throughout its lifetime (see Remillard et al. 2006 for review) and it is suspected that their higher-mass counterparts may as well (e.g. Merloni et al., 2003; Uttley et al., 2005; Gonzalez-Martin and Vaughan, 2012).

The evolutionary timescales of AGN prevent us from observing change of disk states directly, however that does not mean an AGN disk is static. To the contrary, supermassive black hole accretion disks have displayed evidence of intrinsic variabilities in the form of disk instabilities (e.g. Grupe et al., 2015), outflows (e.g. Tombesi et al., 2010; King, 2010; Zubovas and King, 2016), clumpy "hot spots" (e.g. Porquet et al., 2004; Markowitz et al., 2009), and disk warping (e.g. Reynolds et al., 2009; Fedorova et al., 2016). It is here that AGN, and Type I Seyfert galaxies in particular, have the potential to be very informative: with their relatively unobscured view of the central engine and intrinsic disk emission lying primarily in the UV, their reflected disk emission has less to contend with in the X-ray bandpass. We can study accretion disk properties through relativistic reflection and effectively probe the innermost regions of the disk on timescales from as little as hours to as long as decades.

Studies of Type I and intermediate-Type I Seyfert galaxies have revealed occasional narrow line features that lie at no known intrinsic X-ray atomic energies, but that may still be associated with the accretion disk. Guainazzi (2003) found an emission feature at 5.7 keV in *XMM-Newton* and *BeppoSAX* data of Seyfert 1 galaxy ESO 198-G24 that they interpret as either a part of a disk line profile or possible emission off the inner surface of molecular torus. That same year, Yaqoob et al. (2003) analyzed *Chandra* HETGS spectra of NLS1 galaxy NGC 7314 and found an emission feature at 5.84 keV. They discuss the various sources of the 5.8 keV feature, including the possibility that it may be the blue horn of a heavily-redshifted disk line. Porquet et al. (2004) find a feature at 5.4 keV in the *XMM-Newton* spectra of Seyfert 1.8 galaxy ESO 113-G010 and theorize the source to be hot spot on the disk; the feature's disappearance in a later epoch (Porquet et al., 2007) support the scenario of a short-lived hot spot.

Mrk 493 is a Type I AGN located in an SB(r)b galaxy host at a redshift of z = 0.03. The first detailed X-ray analysis of Mrk 493 was performed by Boller, Brandt, and Fink (1996) when it was included in their collection of NLS1 galaxies observed by *ROSAT*. However, despite being a bright ($\sim$8 $\mathrm{count\,s^{-1}}$ in *XMM-Newton* pn) X-ray object of study for nearly three decades, it did not appear to be a NLS1 of any extraordinary significance until Hurlburt (2013) identified it as a potential Fe Lα emitter during their search for such objects using 2003 *XMM-Newton* data. While not as bright as it was in 2003, the 2015 data of Mrk 493 have proven to be a fortuitous look at a NLS1 in a reflection-dominated, lower-flux state: model-independent analyses as well as detailed spectral modelling together reveal complex, correlated short-term ($\sim$25 ks) variability driven by both a blurred reflector and primary X-ray emitter (Chapter 3).

Though the 2015 X-ray spectra themselves do not require anything more than a blurred reflector plus primary component with cold distant reflection, an additional and unexplained source of variability continued to appear in model-independent analyses: the soft-excess was shown to drop in flux $\sim$ 25 ks before the spectrum above 4 keV and time-resolved Principal Component Analysis (PCA) showed a small, but significant feature between 4 – 5 keV in the primary component across all three EPIC instruments. Chapter 3 discusses the full treatment of the 2015 data, including timing-resolved fractional variability studies and Markov Chain Monte Carlo (MCMC) model error estimation. Here, we investigate the unexplained "red feature" seen between 4 – 5 keV: testing the significance of its presence in the spectra as well as discussing the results of model-independent tests and feasibility of possible sources. We utilize the 2015 data mentioned above and observation details are described fully in Chapter 3. (see Table 3.1).

The paper is organized as follows: Section 4.2 describes a principal component analysis performed on the time-resolved spectra and Section 4.3 addresses how the red feature changes spectroscopically over short timescales. Section 4.4 investigates the flux dependence of the red feature. Lag analysis is attempted in Section 4.5 and a residual mapping technique is applied in Section 4.6. Possible origins for the red feature are addressed and tested in Section 4.7 and a summary of the work with conclusions are in Section 4.8.

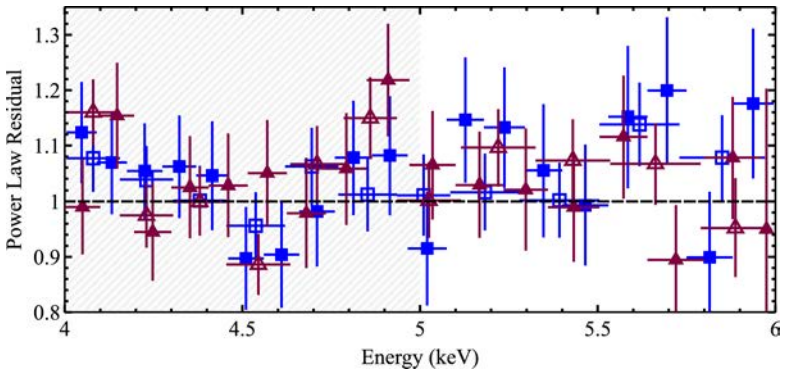

Figure 4.1: Power law residuals between 4–6 keV for both 2015 epochs of EPIC data. XMM15a pn (filled maroon triangles) and merged-MOS data (open maroon triangles) were fit with a power law simultaneously with XMM15b pn (filled blue squares) and merged-MOS data (open blue squares), with power law normalization allowed to vary between epochs. The 4–5 keV band of interest from the time-resolved PCA is shaded in grey.

4.2 Principal Component Analysis

As explained in Chapter 3, the 2015 time-resolved PCA showed the first evidence of an additional source of variability unexplained by a single blurred reflector scenario. Time bins that included periods of deep minima were shown in Chapter 3 to be the most reflection-dominant and it were these time bins, Bin 3 and Bin 8, that also showed evidence of a source of variability between 4 – 5 keV in the first principal component (Fig. 3.11). The sloped shape of PC 1 can be associated with changes in normalization of either the power law or blurred reflection components, a parameter like disk ionization, or some combination of all three. Variability above 6 keV may be tentatively attributed to the Fe Kα emission, should it prove variable on such timescales. However, the feature between 4 – 5 keV is still unaccounted for.

Simply "zooming in" between 4 – 5 keV on the average spectra from 2003 and 2015, there is only inconclusive evidence of the red feature as slight positive residuals around 4.8 – 4.9 keV in the 2015 spectra after a simple power law is applied (Fig. 4.1). It is not surprising that the XMM03 data may not pick up on such a subtle feature, as the short look was $\sim$20 ks long. A look at the background spectrum of XMM15a in comparison to the background-subtracted source spectrum

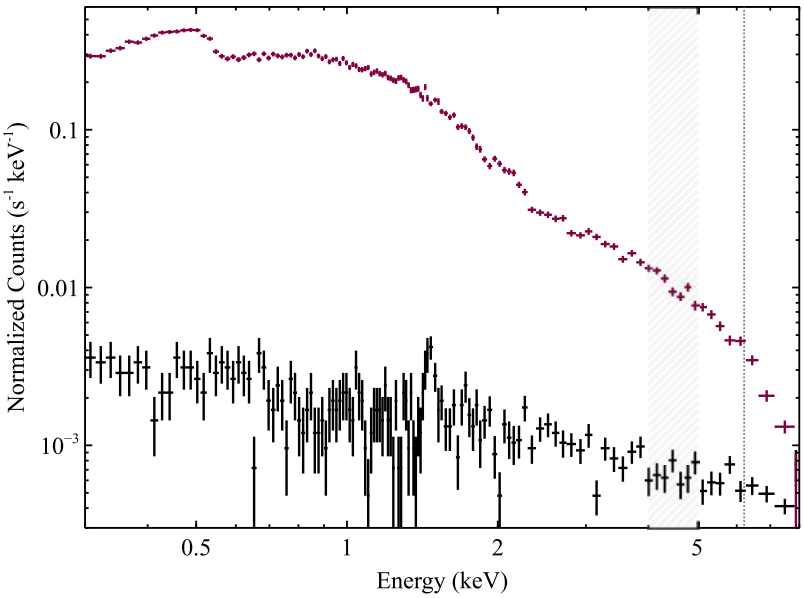

Figure 4.2: XMM15a merged-MOS data (maroon) plotted with the background spectrum (black). Spectra were truncated above 8 keV due to high background. The 4–5 keV band of interest is highlighted (grey diagonal fill) and the location of the Fe Kα line at 6.4 keV in the source frame is marked (grey dotted line).

(Fig. 4.2), no obvious background feature can explain the residuals although an insignificant, but visually apparent, bump can still be seen in the source spectrum around 4.8 keV.

4.3 Time-Resolved Spectra

Time-resolved spectra were extracted from each of the eight bins as described originally in Section 3.6.1. Due to superior signal-to-noise, merged-MOS spectra alone are discussed unless otherwise noted.

The residuals of a power law simultaneously fit with its parameters free to vary between 2 – 8 keV in each time bin of XMM15b revealed an interesting evolution in the spectra between 4 – 7 keV (Fig. 4.3). Visual inspection shows that in the first 25 ks, a moderate positive residual is seen that resembles a redshifted broad Fe Kα line around 6 keV (Bin 5, dark blue). Between 25 ks– 50 ks, the positive residuals between 5 – 6 keV increase and there appears an additional

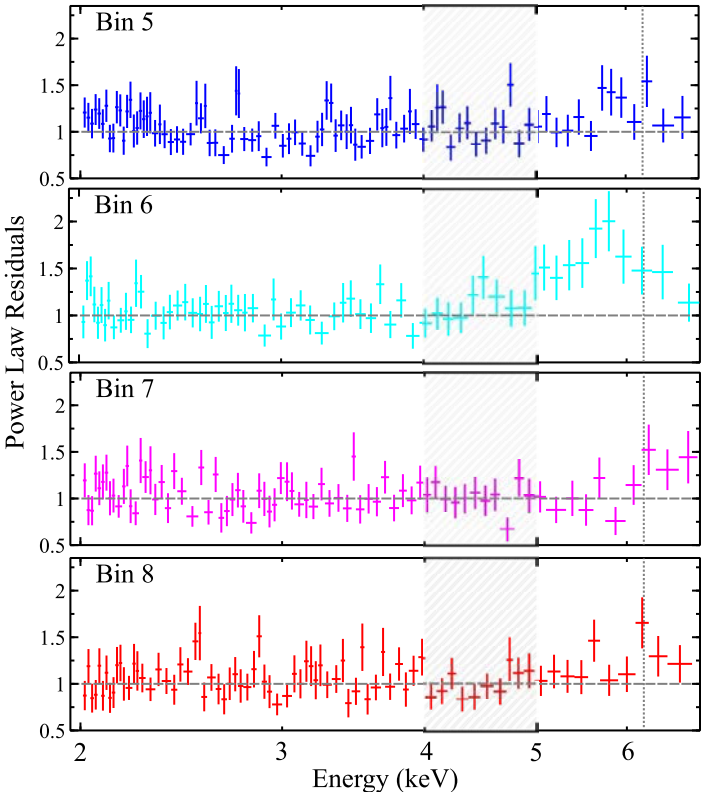

Figure 4.3: Model residuals of the merged-MOS time-resolved spectra fit with a power law between 2–7 keV. Time bins are those illustrated in Fig. 3.7, time increases from Top to Bottom, and data colours are consistent with the bin labels in Fig. 3.7. The bands of interest are marked as in Fig. 4.2.

positive, smaller residual around 4.5 keV (Bin 6, cyan). Between 50 – 75 ks, positive residuals remain around 6.4 keV in the source frame while the lower energy residuals have disappeared (Bin 7, pink). Finally, in the last 25 ks of the observation, no clear positive residuals of any kind remain, although one might see a hint of the Fe Kα line (Bin 8, red).

We see that, at least on 25 ks timescales, the Fe Kα line appears to be variable: beginning the XMM15b observation slightly redshifted before returning to its intrinsic energy. If the Fe Kα line is also variable on shorter timescales, i.e. within each individual time bin, it is reasonable to confirm that the PCA components seen in Chapter 3 dominating above 6 keV may describe changes with the Fe Kα line. The time-resolved spectra were further subdivided in attempts to isolate periods of deep minima. These periods reached as low as 0.5 $\mathrm{count\,s^{-1}}$ in the merged-MOS broadband light curves, but lasted for only about 10 ks or so and thus were too noisy upon subdivision to resolve any features.

Spectra from all four time bins were individually fit with power law plus Gaussian models between 2 – 7 keV in order to measure the significance of positive residuals. While all residuals were visibly improved by the addition of a Gaussian, three out of four of the XMM15b time-resolved spectra did not statistically require anything more than a power law. Bin 6, however, did improve its fit statistic with the addition of a the Gaussian ($\Delta\chi^2$= 30 for 3 d.o.f) located at $5.80^{+0.18}_{-0.19}$ keV with σ = $0.53^{+0.32}_{-0.19}$ keV. Adding a second narrow (σ = 0.001 keV Gaussian, $E = 4.61^{+0.08}_{-0.07}$ keV, describe the data well between 4 – 5 keV and no residuals remain, although the fit statistic does not significantly change. If the fit range is extended down to 0.3 keV, the data are best described by the addition of a black body component with E = 0.11$\pm$0.01 keV and $norm = (8.29^{+2.94}_{-3.30})\times10^{-6}\,\mathrm{erg\,s^{-1}\,kpc^{-2}}$ (χ^2_ν / d.o.f. = 208 / 225).

It is interesting to note that Bin 6 is also the time period of highest reflection fraction, R, (Chapter 3, Table 3.3) and 25 ks following is the time bin of lowest R. As these spectra are too similar in flux to plot difference spectra directly, the best toy model of Bin 6 (cyan) was applied to Bin 7 (pink) without re-fitting which clearly illustrates the changing behaviour of the spectra above 4 keV (Fig. 4.4, Middle, pink). Despite the change in R and features above 4 keV, the soft-excess

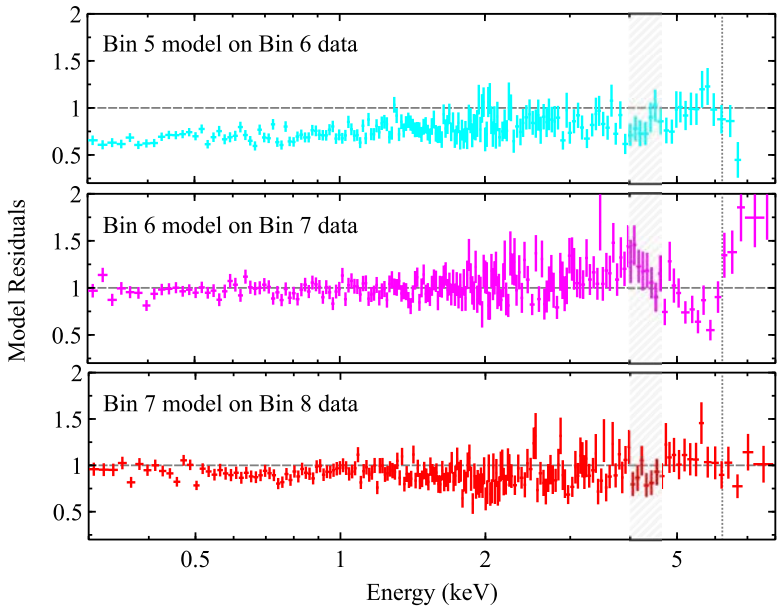

Figure 4.4: Residuals of the best-fit toy models applied to the spectra of consecutive time bins. Figure details are the same as those in Fig. 4.3.

remains consistent. Expanding the exercise to include Bin 6 with a Bin 5 model (Fig. 4.4, Top, cyan), and Bin 8 with a Bin 7 model (Fig. 4.4, Bottom, red), we see an illustration of the difference spectra throughout XMM15b: both the soft-excess and red feature change between the first 50 ks of XMM15b, but the next 25 ks see only variability above 4 keV while the soft-excess remains constant, and in the last 25 ks there is barely any change at all.

The time-resolved spectral model residuals of XMM15a show similar characteristics to those of XMM15b, with positive residuals above 4 keV, but any potential features are even less resolved as those of XMM15b and model parameters were inconclusive. The soft-excess also changes in flux during XMM15a: dipping slightly between the first two time bins before rising by about 17% in the last 50 ks, consistent with the trend of the overall continuum.

4.4 Flux-Resolved Spectra

Flux-resolved spectra of XMM15a and XMM15b were extracted for periods of highest and lowest flux ($>$0.6 $\mathrm{count\,s^{-1}}$ and $<$0.5 $\mathrm{count\,s^{-1}}$ respectively, for individual MOS instruments as an example). The results of the individual epochs were compared and then stacked to boost signal-to-noise. Residuals of a power law simultaneously fit between 2 – 7 keV to the spectra in the same manner as the time-resolved spectra show a positive excesses around 6 keV and also around 5 keV (Fig. 4.5, Top) – the latter only apparent in the lower-flux spectra. No positive residuals remain between 4 – 5 keV, where the red feature is seen in the PCA and time-resolved spectroscopy.

The lower-flux data alone were then modelled to test the significance of the 5 keV residual. A power law plus Gaussian fit to the 2 – 7 keV band described the low-flux spectra well (χ^2/ dof = 664 / 644), however positive residuals remained (Fig. 4.5, Middle). The addition of a second Gaussian to the model improved the residuals (Fig. 4.5, Bottom) and the fit statistic moderately improved ($\Delta\chi^2$= 11 for 6 additional degrees of freedom). A slight, but statistically insignificant rise in residuals continues to be present from around 5.5 – 6 keV which may be the red wing of a broad Fe Kα line. The best-fit toy model found a photon index of Γ = $2.19^{+0.09}_{-0.04}$ (pn), 2.18$\pm$0.08 (MM) and first Gaussian parameters of E_1 = 6.37$\pm$0.07 keV (pn), $6.43^{+0.07}_{-0.08}$ keV (MM) and $\sigma_1 < 0.25$ keV (pn), 0.12 keV (MM). The second Gaussian central energy was E_2 = $5.24^{+0.18}_{-0.17}$ keV (pn), 5.26$\pm$0.05 keV (MM). The second Gaussian also had a constrained EW of $\sigma_2 < 0.45$ for the pn spectra, however the EW remained narrow and unconstrained for the merged-MOS.

To ensure that the $\sim$5 keV positive residual was not an artifact of the background, the toy model that best described the lower-flux spectra was applied to the higher-flux state spectra without fitting. A constant factor was used to scale the flux appropriately without affecting the model itself. The toy model over-predicted the data at both $\sim$5 keV and 6.4 keV and thus these features were not a part of the constant continuum.

It is possible that the limited signal-to-noise may produce marginally significant spectral features like the one seen around 5 keV in Bin 6 or the epoch-merged, low flux-resolved spectra

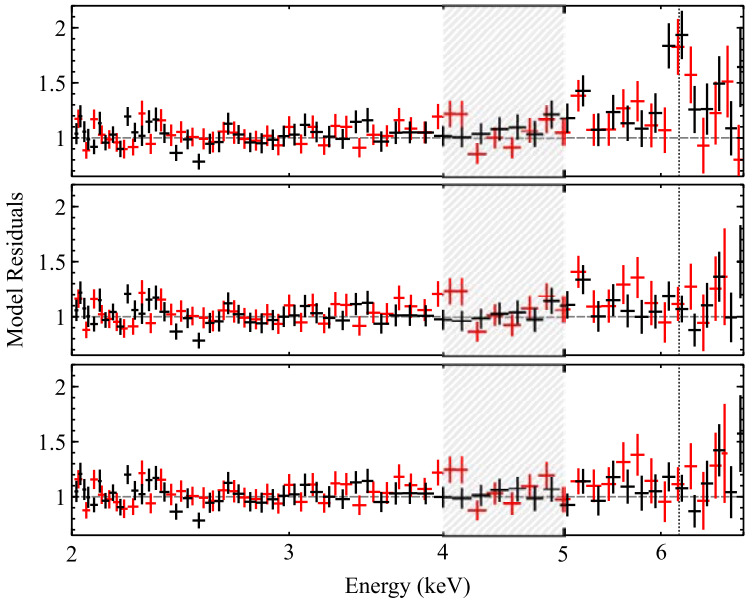

Figure 4.5: Toy model fit from 2–7 keV to the low-state pn (black) and merged-MOS (red) flux-resolved spectra. Top: a power law model alone. Middle: a power law plus single Gaussian. Bottom: same as Middle with the addition of a second Gaussian. Both residuals lie between 5–6.4 keV in this case.

here. In which case, the red feature is nothing more than an artifact of systematic error. To test this possibility, 500 simulated spectra were created between 0.3 – 8 keV from nothing but a power law profile. The spectra had total counts equal to that of the pn low flux-resolved spectrum, as this was the spectrum that had the most statistically significant red feature. A power law model plus Gaussian model was then fit to each spectrum and the Gaussian stepped through the entire 0.3 – 8 keV energy range in steps of 0.05 keV to avoid local minima find the best fit. When Gaussian width was fixed to that of a narrow feature (σ = 1 eV), 16.8% of the fits found a "feature" with greater significance than the red feature in the flux-resolved spectra of Mrk 493. When Gaussian width was free to vary, 26.8% of the fits found a more significant feature. Therefore, while the detection of the red feature in the flux-resolved analysis is certainly not robust, we see that it is unlikely to be due to systematic error and, when taken along with the model-independent detections, it cannot be dismissed easily.

4.5 Lag Analysis

The time-resolved PCA initially indicated the 4 – 5 keV band exhibits variability which was also confirmed by the time-resolved spectroscopy. The flux-resolved spectra reveal statistically significant features between 5 – 6 keV which appear contradictory to the time-resolved analyses until one considers the timescales involved, namely that the time-resolved data probe 25 ks (hours) timescales and below while the flux-resolved data probe ∼200 ks (days). Especially interesting is how the features above 4 keV change apparently independently of the soft-excess. Assuming the standard AGN central engine geometry consisting only of the black hole, accretion disk, corona, and distant torus, one expects all but the most distant reflected emission to be correlated with the primary emission in some fashion. Therefore, we perform a thorough lag analysis on the 2015 data in hopes of clarifying the spectral components at play while maintaining a model-independent approach.

Detections and subsequent analyses of time lags between individual spectral components (i.e. reverberation mapping) have been game-changers in the field of AGN astronomy, for both high-energy regimes and optical/UV (see for example Peterson 1993, Peterson & Horne 2004, and Uttley et al. 2014). By measuring the time delay between flares in the UV continuum and optical broad-line region (re)emission, for example, one can calculate the light travel time and therefore proper distance across the broad-line region and also estimate black hole mass (e.g. Chiang and Murray, 1996; Peterson and Horne, 2004; Li et al., 2013). Applying reverberation mapping to central engine geometry, correlations between variability in the primary and blurred reflection X-ray components help constrain the radius of the ISCO and black hole spin (e.g. Zoghbi et al., 2010; Cackett et al., 2014; Reynolds, 2014; Kara et al., 2016).

Of course, lag analysis is not limited to comparing emission from specific physical components of the AGN and can be applied to any energy bands of interest. We therefore decided to explore potential time lags in three energy bands: 0.35 – 1 keV (representative of the fiducial soft-excess), 1 – 2 keV (representative of the fiducial primary component), and 5 – 8 keV (includes the iron line

band). Various and more extended "hard bands" were also tested, ranging from 2 – 8 keV and 3 – 8 keV, but the most conclusive findings arose from comparisons to the 5 – 8 keV band and so we will not discuss the other hard bands further. We followed the procedures outlined by Nowak et al. (1999) and Uttley et al. (2014) unless otherwise noted.

Thorough tests were run to ensure the most reliable approach. Epoch XMM15b included multiple incidences of background flaring and required good-time interval maps for its data processing. However, one cannot have non-contiguous light curves when performing a lag analysis unless the omitted time segments are very small, which is not the case in XMM15b. Therefore, despite the more interesting nature of its variability compared to XMM15a (see Fig. 3.4), XMM15b was excluded from the lag analysis. Lag analyses produced on MOS 1, MOS 2, merged-MOS, and pn instruments were compared. While being generally consistent overall, the pn data appeared more sensitive to correlations and as it also has superior signal-to-noise as an individual (i.e. not merged) instrument. Thus, the lag analysis of the pn data were pursued further. Lastly, the time binning of the original light curves influence the lag analysis results: too small a binning and correlations may be lost in the noise, too large a binning and the analysis will not be able to resolve correlations on time scales shorter than the bin length. Larger time bins will also directly limit the temporal frequency range being studied. Light curve time bins of 10, 20, 30, and 40s were tested and it was determined that a light curve time binning of 10s was best for the XMM15a data as a balance between resolution and signal-to-noise.

Time lag analyses were performed for 0.35 – 1 keV vs. 1 – 2 keV, 0.35 – 1 keV vs. 5 – 8 keV, and 1 – 2 keV vs. 5 – 8 keV, producing lag spectra as a function of both frequency and energy. Unfortunately, despite evidence of energy band correlations in a preliminary cross-correlation analysis, the coherence was too low in the frequency bands of interest and final lag results of both the lag-energy and lag-frequency spectra were inconclusive.

4.6 Residual Mapping

The apparent delay in variability between the time-resolved spectra below 1 keV and above 4 keV remains an important curiosity and so we attempt an alternative approach to uncovering the mystery by looking at the excess residual images following the method illustrated by Iwasawa et al. (2004).

The pn data from each observation were used to create 10 sequential spectra, each one of 10 ks duration ($\sim$ 6 – 7 ks exposure after correction for live-time and background). For each spectrum the data between 3.5 – 5.5 keV and 7 – 10 keV were grouped with a minimum of 20 counts per bin and fit with a broken power law model. The break energy was fixed to 7 keV and is introduced to the continuum model to account for the high background. Note, the 4 – 5 keV band is not excluded during the continuum fit. The data in the omitted Fe Kα band are replaced and the spectra are re-binned into 250 eV-wide energy bins. From these spectra, the excess residuals in the 4.63 – 5.13 keV and the 5.88 – 6.63 keV bands are recorded, and an image is created following Iwasawa et al. (2004).

The pn excess residual image was of rather low signal-to-noise in the band of the red feature. Therefore, the method was repeated for the MOS 1 and MOS 2 detectors in each epoch. The process was similar with the exception that energy bins were 225 eV wide. The residuals for the red feature were extracted from 4.69 – 5.14 keV and 5.82 – 6.5 keV for the Fe Kα band. The residuals from all three EPIC instruments (PN + MOS 1 + MOS 2) were stacked and light curves created for both XMM15a (Fig. 4.6, Top) and XMM15b (Fig. 4.6, Bottom). The error on the light curve data points is shown as the variance in the light curve. We do not carry out full MC error estimates as we realize the excess residuals are of low significance in the 10 ks bins. We simply wish to examine possible trends with the continuum and Fe Kα bands.

The light curves from both orbits are moderately consistent and 0.2 – 10.0 keV continuum band (black points) mimics the overall light curve trends for both epochs. The increase in Fe Kα line flux as seen in Fig. 4.3 (second from Top, light blue) is also shown here as a jump in the Fe Kα line profile (blue circles). The appearance of the red feature in the same time bin, however, are not

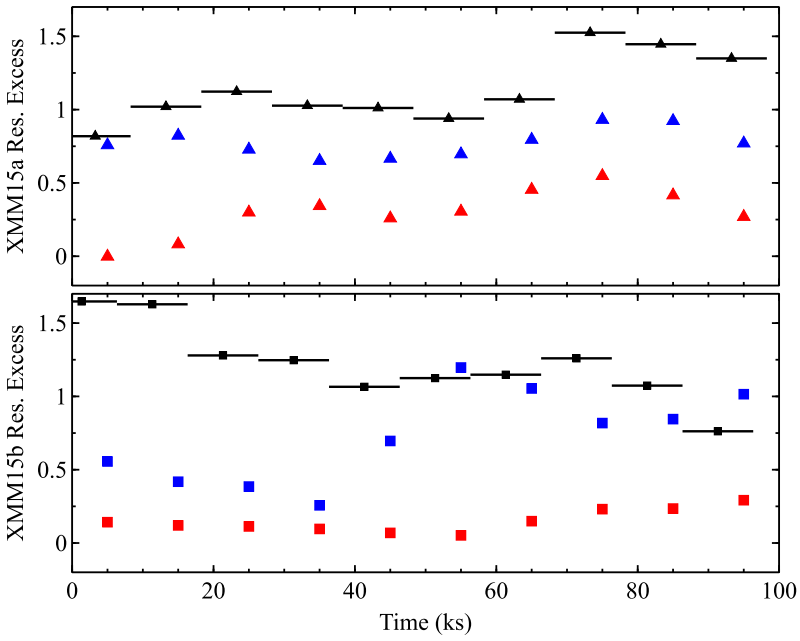

Figure 4.6: Residual mapping using merged EPIC data for XMM15a (Top, triangles) and XMM15b (Bottom, squares). A continuum band (0.2–10.0 keV, black) is compared to that of the Fe Kα ($\sim$5.8–6.4 keV, blue) and a band including the time-resolved red feature ($\sim$4.65–5.14 keV, red). Individual band energies differed slightly based on instrument.

reproduced in the residual map (red squares). The residual maps of XMM15a show that both the energy band of the Fe Kα line and that of the red feature evolve in roughly the same fashion, and that both follow the trend of the continuum in that epoch. Thus, although the features appear to vary differently from the soft-excess in the time-resolved spectra, it appears as though they may originate from a similar source.

Inconsistencies between the time-resolved spectral residuals and the residual maps may be due to the difference in the time binning, which are about a factor of three larger in the time-resolved spectra than they are in the mapping. The behaviour and appearance of the X-ray spectrum of Mrk 493 has certainly proven to be very much dependent on the time scales on which it is seen.

4.7 Discussion

Both spectroscopic and model-independent analysis of the two 2015 *XMM-Newton* observations of Mrk 493 continue to point at an unidentified source of variability acting in the 4 – 5 keV band. Epoch-merged flux-resolved spectra in the low state show a power law residual feature around 5 keV that is statistically significant and time-resolved spectroscopy catch a similar feature around 4.5 keV that is short-lived (25 ks). While similar residuals in the average spectra are not statistically significant, the fact that this red feature is present in multiple instruments, across multiple epochs, and appears along with the Fe Kα line to be variable, suggests the red feature is an intrinsic component to the X-ray spectrum and may be in some way connected to a reflection component and underlying continuum.

While robust statistical studies have been unable to elucidate the true nature of the red feature due to limited signal-to-noise, we are certainly free to hypothesize what the source of variability may be and so here we address the possible scenarios that may give rise to such a feature.

4.7.1 Spallation

Spallation, or the destruction of iron into metals of lower atomic number by the bombardment of energetic protons, has been theorized to happen on the surface of accretion disks. First proposed by Skibo (1997), observations of spallation effects are becoming more of a possibility as technology advances to the point that these lower-Z atomic transitions can be resolved in the X-rays. Most recently, evidence of spallation has been found in the fluorescent X-ray spectra from the broad-line region (BLR): Turner and Miller (2010) analyze a feature around 5.4 keV in NGC 4051 and determine it could be Cr I Kα, enhanced to the point of detectability via spallation of gas outside of the plane of the accretion disk; and Xu et al. (2016) suggest enhanced Mn in M51 is likely due to spallation of BLR clouds.

Evidence of spallation in the accretion disk itself has remained more ambiguous. Blurring effects such as those that broaden a Fe Kα inner disk line could also broaden the (already weaker) lower-Z lines to the point of non-detection. An extended red wing of a very broad Fe Kα line could also complicate spallation detections, even if the lower-Z features are narrow themselves. Finally, we expect the inner accretion disk to be ionized and thus the features quoted in Skibo (1997, Fig. 4) will be more numerous as the lower-Z elements now include their H-like and He-like counterparts.

First assuming the simplest scenario of a cool source, the red feature in Mrk 493 could be either Ti Kα (4.51 keV) or V Kα (4.95 keV). These elements are expected to have ratios of 4 and 3% that of Fe Kα, respectively (Skibo, 1997). Our time-resolved spectral feature has a line centre of around 4.6 keV, suggesting Ti as the best spallation candidate. However, this same time-resolved spectral feature has a flux of 9% that of the Fe Kα line (Fig. 4.3, second from Top), and thus our line ratios are not consistent. In other cases, the red feature appears closer to 5 keV (Fig. 4.5, Top), which is more consistent with the spallation product V. However, the line ratios here are even more disparate with the hypothetical V line having a flux a whopping 60% that of Fe Kα.

Therefore, the possibility of spallation as the source of the mystery feature here in Mrk 493 appears slim. The line ratios and varying central energies of both the mystery feature and larger

Fe Kα line are both more suggestive of high-velocity redshifts of intrinsic iron rather than a separate atomic feature.

4.7.2 Inflow

A shift in an Fe Kα line to redder energies can happen via bulk motion of some kind away from the line of sight, as would be seen from an inflow of material toward the central engine. Such inflows could offer an explanation for the apparent Fe Kα line shift in time bin 6 as well as the red feature. The weaker flux of the red feature is in agreement with the increase in relativistic Doppler boosting away from the observer as would be seen in the faster flow. The ~ 0.6 keV redshift of Fe Kα from its intrinsic energy of 6.4 keV would require a velocity of around 0.1 c. To shift Fe Kα further to the red feature band (4 – 5 keV) would require much greater velocities of around 0.25 c or more.

Inflows within the central engine have been discussed before as explanations for anomalous emission lines around similar energies in other objects (e.g. Yaqoob et al., 2003; Giustini et al., 2017), however it is difficult to imagine a scenario where one would see an inflow at an angle and speed sufficient enough to redshift the Fe Kα line by nearly 2 keV while also having no signatures of absorption that correspond with the diffuse, flowing material along the line of sight.

Outflows or winds in AGN, on the other hand, are well-documented and ultra-fast outflows (UFO's) have been observed reaching velocities of up to $\sim 0.1\ c$ (Tombesi et al., 2010). It would be a very contrived scenario, however, that allowed an outflow from the far side of the disk to be seen (redshift) and not the that from the near side (blueshift). Additionally, one of the calling cards of outflows are the absorption features and even with absorption signatures, there remain alternative explanations for some winds in the form of intrinsic disk self-absorption (Gallo et al., 2013).

Depending on geometry, whether one adopts an outflowing or inflowing scenario there remains the question of additional blueshifted features of the material on the opposite side of the disk. The blueshifted features would have to be attenuated somehow in order for only the redshifted material to be observed alone. This attenuation brings us back to the absorption scenario and consequent features. It is unlikely that the red feature seen in the 2015 Mrk 493 spectra is due

to an outflow/inflow.

4.7.3 Hot Spot

The fact that this mystery feature is seen only with the iron line in the low-flux data, that it is seen in multiple instruments, and that it behaves in the same manner as the Fe Kα line across short timescales all point toward a disk-like feature, but one independent of the more pronounced Fe Kα line: a hot spot perhaps or the red peak of an extended disk line.

In addition to line-of-sight redshifts, another way to have Doppler shifting is through rotational motion such as that of the disk itself. Significant velocities can be achieved, as the source radius increases, that are sufficient to shift an intrinsic Fe Kα line by the >1 keV observed in the red feature. For a set inclination, the width of the shifted line is dependent upon the area of the source, a patch on the disk that emits from a wider Δr produces a broader line, and the length of the exposure determines whether one observes an annulus or a so-called 'hot spot'. An annulus of emission would produce both a blueshifted and redshifted line peak, but a shorter-lived hot spot could produce a singularly blue- or redshifted line depending on the radial motion observed.

Hot spots, while rare, have been observed (e.g. Miniutti & Fabian 2006). NGC 3516 is the poster child for disk hot spots in AGN ever since Iwasawa et al. (2004) published residual maps, similar to those shown above for Mrk 493, displaying prominent saw-toothed patterns of periodic variability from a 5.8 – 6.2 keV feature. NGC 3516 was observed on time scales similar to the 2015 observations of Mrk 493 (90 ks vs. 96 ks and 99 ks), although the flux of the feature in NGC 3516 reached upwards of $2.5\times10^{-5}\mathrm{ph\,cm^{-2}\,s^{-1}}$ whereas the same energy band for Mrk 493 yields only 0.83 and 0.9 $\times10^{-5}\mathrm{ph\,cm^{-2}\,s^{-1}}$ for XMM15a and XMM15b, respectively. If Mrk 493 were to return to its brighter state without significantly altering its continuum spectrum, it is possible that a hot spot could be conclusively resolved in this object as well.

The red feature in Mrk 493 may be a redshifted, narrow Fe Kα line originating from a disk hotspot while the more prominent and broad 6.4 keV feature originates from blurred reflection of the disk itself. Alternatively, returning to Bin 6 of the time-resolved spectra (Fig. 4.3, second from

Top), we see what may be *two* single-peaked Fe Kα profiles that have been redshifted away from the intrinsic 6.4 keV energy to different observed energies due to their different radial velocities away from the line-of-sight. Such shifts appear to happen on time scales no longer than 25 ks and thus can explain why the average spectrum of individual epochs continues to show the Fe Kα line at its intrinsic energy.

The smallest timescale we observe the red feature is around 25 ks (Section 4.3). If a hypothetical hot spot were to last at least the length of that light curve segment, dynamical timescale estimates suggest that it would originate from a disk radius of $\sim 43 R_{\rm g}$. If a hotpot lasts at least the length of the XMM15a observation, the source would originate from $> 100 R_{\rm g}$. Both of the scenarios are plausible as line variability studies Petrucci et al. (e.g. 2002); Yaqoob et al. (e.g. 2003); Iwasawa et al. (e.g. 2004); Zoghbi et al. (e.g. 2010) confirm these features can change on such timescales.

Alternatively, perhaps we are observing multiple instances of hot spots as they flare and dissipate on the disk at various times over various radii. Magnetohydrodynamic (MHD) disk theory predicts turbulence in the disk would result in stochastic flaring over time (e.g. Merloni and Fabian, 2001; Reynolds and Nowak, 2003). The difference in residuals between the flux-resolved and time-resolved data could indeed be showing a shift in the red feature central energy between various timescales as you would expect to see if flares appeared at random across the accretion disk.

4.7.4 Hot Annulus

Instead of single-peaked features, another possibility for the residuals seen in the time- and flux-resolved spectra is a *double-peaked* Fe Kα line profile. Such a double-peaked profile or disk line can be formed by a hot spot on the disk, as described above, that is observed over at least one orbital period around the black hole: producing both the red- and the blue-shifted Doppler peaks as the spot processes around the circumference of the disk at a given radius, forming an annulus of emission. Double-peaked disk lines have been observed in the X-ray spectra of stellar-mass (e.g. GRS 1915+105; Miller and Homan (2005)) and supermassive (e.g. MCG-6-30-15; Tanaka et al. (1995)) black hole varieties.

While not statistically significant, the 4 – 5 keV positive residuals seen in Bin 6 show the clearest example of the red feature that is from a single epoch. To test how a disk line scenario may explain the short-term variability in Mrk 493, the XMM15b time-resolved spectra were fit simultaneously between 2 – 8 keV with a power law + Laor + disk line model. Disk line inner and outer radii, centroid energy, and normalization were allowed to be free while inclination angle was linked across the data sets. As the model proved to be insensitive to inner emissivity index (not surprising given the findings of Chapter 2), the index was fixed to the standard value of 3. All Laor parameters remained linked with the exception of normalization and Laor centroid energy fixed at 6.4 keV.

As expected for the time-resolved spectra data quality, the model fit the XMM15b data well (χ^2/ dof = 475 / 497) with no obvious residuals remaining. The inner radius of the Laor profile was $1.9R_{\rm g}$, indicative of a high black hole spin, and inclination angle around 59°. The disk line inclination was around 35°, less than that required for blurred reflection (see Section 3.6). In this scenario, the differences in the XMM15b time-resolved spectra are attributed to changing disk line centroid energies, which ranged from 5.5 – 6.4 keV, and bounding radii. The Bin 6 spectrum in particular was well described by R_{in} = 18$\pm R_{\rm g}$, R_{out} = 28$\pm R_{\rm g}$, and E = 5.5$\pm$ keV.

This simultaneous fit to the XMM15b time-resolved spectra is meant as an exercise to test the viability of a disk line scenario and while such modelling cannot be quantified with current data, this exercise does support the possibility that both the Fe Kα line and unidentified 4 – 5 keV feature could in fact both be a part of a *single* line profile as two horns of a double-peaked emission line. For the disk line theory to be robust, it must be able to describe more than just spectra in an isolated energy band. However, the limited signal-to-noise make robust broadband analysis challenging. We therefore attempted to fully model the average background spectrum of XMM15b in hopes of uncovering and then modelling the mystery feature in a more robust manner. The merged-MOS background spectrum was utilized as it were these data of the XMM15b epoch that displayed the most interesting behaviour in the timing analysis. XMM15a merged-MOS and pn spectra were also tested in the following manner and were consistent.

The source plus background spectrum (i.e. not background-subtracted) for merged-MOS

XMM15b was examined along with the background model. A single power law fit between 2 – 8 keV and extrapolated shows the prominent soft-excess, but also two clear positive residuals between 5 – 7 keV. The addition of a blurred reflector minimized the soft-excess residuals and part of the 6.4 keV feature, but positive residuals around 5 keV remained. If a disk line was then added to the model with its parameters free to vary and line energy set at 6.4 keV, the resulting model is a very good descriptor of the data (χ^2_ν/dof = 509 / 505) and all but the highest-energy residuals vanish. Although it appears that the intrinsic Fe Kα line is redshifted down to around 5.9 keV in Bin 6 of the time-resolved spectra, there is no evidence of redshift in the average data and any 25 ks-scale variations could very well be averaged out.

Thus, even with the rising background above 5 keV, both blurred reflection and a disk line are required once the background flux has been robustly accounted for. In this scenario, the blue peak of the disk line accounts for most of the $\sim$6 keV flux. The disk line fit to the average XMM15b spectra required an inclination of around 18° while a blurred reflector fit to the same data find θ = 53°. This is consistent with the XMM15b time-resolved spectral modelling described above.

4.7.5 Sanity Check

While the red spectral feature seen between 4 – 5 keV in Mrk 493 is not able to be robustly modelled via spectroscopy alone, its persistence in both time-resolved and flux-resolved analyses as well as appearance in model-independent analyses like PCA, compels us to search for a self-consistent explanation to its presence and behaviour. A handful of possible sources exist, however phenomena such as spallation and disk winds can be quickly ruled out based on missing spectral features and/or timing properties. A hot spot or hot annulus on the disk itself appears far more likely and spectral modelling supports a disk line scenario.

To approach the problem from a theoretical perspective, the general relativistic formula for gravitational redshift was solved following the work outlined by Fabian et al. (1989) for a range of observation angles across radii ranging from $5R_\mathrm{g}$ – $1000R_\mathrm{g}$. The resulting line energy ratios were plotted as a function of radius. First assuming a hot spot scenario, we interpret the two features

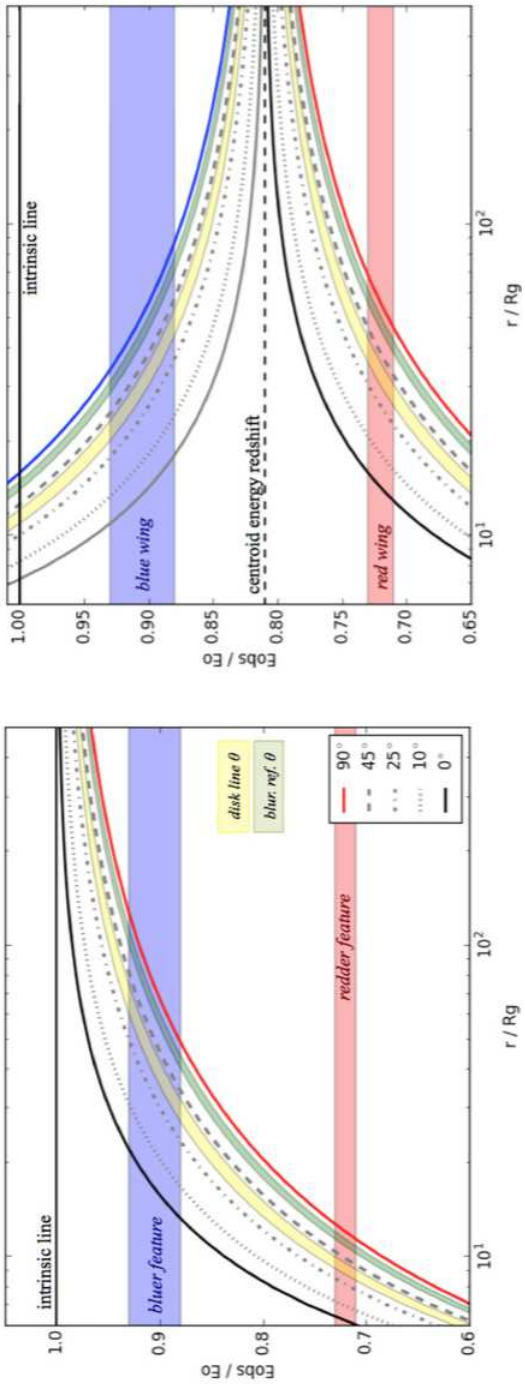

Figure 4.7: Diagrams of general relativistic redshift over a range of radii for given line energy ratios. The ratio of observed energy, E_{obs}, over intrinsic energy, E_o, is plotted on the y-axis with unity marked as a horizontal solid black line. Radii in terms of R_g are plotted on the x-axis. As an example, 90, 45, 25, 10, and 0° are drawn as curved lines. The two measured angles obtained via spectroscopy are highlighted in yellow (disk line model) and green (Laor model). The measured energy ratios for the red feature (red) and Fe Kα line (blue) are drawn as horizontal bands. Band widths for both angles and energy ratios denote measured standard deviation. Left: scenario for a hot spot. Right: scenario for a hot annulus. Both scenarios require significant redshifts from intrinsic Fe Kα.

in the Bin 6 residuals are each singular Fe Kα profiles. As no blueshifted features of any kind are detected, only lines of redshift (i.e. energy ratios <1) are illustrated (Fig. 4.7, Left).

Utilizing the centroid energies obtained from the toy model fit to Bin 6 (Section 4.3), one can compare the observed energy ratios of the red feature (red horizontal band) and more prominent feature around 5.9 keV (blue horizontal band) to the observation angle curves and thus obtain estimates for the source radii. Central energies were measured to be E_r = $4.61^{+0.08}_{-0.07}$ keV and E_b = $5.79^{+0.18}_{-0.19}$ keV for the redder and bluer feature, respectively. The widths of the horizontal bands illustrate the respective errors. The features are shifted down from the intrinsic line energy (solid horizontal black line) which would have an energy ratio of unity. Angles modelled are 90° (solid red line), 45° (dashed grey line), 25° (dash-dotted grey line), 10° (dotted grey line), and 0° (solid black line). Inclination angles found from the simultaneous time-resolved spectral modelling (Section 4.7.4) are highlighted as well, along with their associated errors: the Laor model in green and the disk line model in yellow. Inclination band widths denote each measurement's standard deviation.

We can see that, regardless of the measured inclination angle we adopt, the redder 4 – 5 keV feature and bluer 6 keV feature seen in Bin 6 must come from different radii as long as we continue to assume they are independent sources. The range of possible radii for the bluer feature, between roughly 25 – 60$R_{\rm g}$, agrees with the dynamical timescale estimate sketched out in Section 4.7.4 based on the time bin size. The redder feature theoretically originates from much further in, around 8 – 10$R_{\rm g}$, which would give it a shorter observable lifetime if it must remain a single redshifted peak (and not a double-peaked profile). This shorter lifetime is consistent with observations, where the red feature appears in the most clearly in Bin 6 and the stacked time bins 3 and 8 of the PCA and thus does not appear to be present for longer than 25 ks at one time. Therefore, the theoretical possibility of transient hot spots on the disk cannot be ruled out and in fact do well to explain the complex short-term spectral variability observed in Mrk 493 during the two 2015 observations.

A hot annulus scenario can also be illustrated in the same way. If we examine the possibility of a disk line to explain the residuals in Bin 6, lines of both blueshift and redshift must be drawn (Fig. 4.7, Right). In addition to the now double-peaked curves, the disk line centroid energy must

be redshifted itself if the disk line is to account for both the redder and bluer features observed – both of which are redward of the intrinsic Fe Kα in the time-resolved spectra. We have a constraint on how much the central energy must be shifted: the source radii for the blue wing and red wing must match since they are now from a single source. One can imagine moving the disk line centroid energy (dashed horizontal black line) down slowly until the overlapping areas highlighted by the red and blue horizontal bands stack vertically. We see that the radii line up well when the disk line centroid energy is observed to be just over $0.8E_o$. Recall that, rough as it is, this exercise agrees with the measured disk line central energy around 5.5 keV found from model fits.

If we are, in fact, observing an additional source of reflection from the disk in the form of a disk line, we can now say the source would have the following characteristics: be located at further radii than the blurred reflector (double-peaked profile not yet smoothed out), would need to be originating from a relatively small in surface area (peaks well-resolved), and would need to have a different inclination angle than that of the innermost regions of the disk (shallower observation angle). Therefore, we could be observing a small warp or "dip" in the accretion disk itself – it must be a dip and not a bump as the disk line angle is shallower than that of the main blurred reflector.

Although observing limits and timescales allow an accretion disk to be modelled as a smooth, two-dimensional surface in most cases, we do not expect an average AGN accretion disk to be so pristine (see Section 4.1). Inherent turbulence and inhomogeneities could very well produce warps (e.g. Reynolds et al., 2009; Fedorova et al., 2016) which, illuminated intermittently by a variable source like the corona, could produce characteristics of a hot spot or annulus like we see here.

4.8 Conclusions

We offer this work as a companion analysis to a deep, multi-epoch analysis of the X-ray properties of Mrk 493 (Chapter 3) by focusing exclusively on a curious 4 – 5 keV feature found therein. This feature was first discovered via model-independent analysis and continues to crop up in in both flux- and time-dependent spectroscopy studies as well as in multiple instruments across multiple

epochs. Due to the consistent appearance of this red feature, one must explore all possibilities before dismissing it outright due to limited signal-to-noise. By thoroughly investigating the red feature in Mrk 493, we conclude:

- Model-independent analyses of 2015 X-ray data uncovered an additional source of variability on timescales < 25 ks that was difficult to account for with the best-fit spectroscopy models. The additional source of variability is first seen in the primary component of the PCA between 4 – 5 keV in the two merged time bins that are dominated by reflection. We dub this the "red feature".

- Time-resolved spectral analysis confirms variability of the Fe Kα line on timescales of 25 ks during which the red feature appears between 25 – 50 ks into XMM15b, although the feature not statistically significant due to the reduced signal-to-noise. Interestingly, the Fe Kα line appears redshifted in the first half of the XMM15b observation.

- Epoch-merged, flux-resolved spectra of the 2015 data uncovered a marginally statistically significant ($\Delta\chi^2$= 11 for 6 additional degrees of freedom) positive residual along with the Fe Kα line in the lower-flux data. Analysis of the background resulted in no way to rule out the red feature on the basis of background alone. At this longer ($\sim$ 200 ks) timescale, the red feature appears around 5 keV.

- Residual mapping of the average spectra of both 2015 observations shows the band of the red feature behaving similarly to that of the Fe Kα band, and both generally follow the trend of the continuum.

- Simultaneous spectral modelling of the XMM15b time-resolved spectra between 2 – 7 keV shows the variability can be explained by transient hot spots on the disk or, alternatively, by a disk line in which the bounding radii and centroid energy shift by roughly 10 and 70%, respectively, throughout the XMM15b epoch. Curiously, the inclination of the disk line is

around 20°while a Laor model for the broad Fe Kα line is around 50°, in agreement with the blurred reflection analysis in Chapter 3.

- Full treatment of the background of the average XMM15b spectrum was performed and the disk line model applied along with a blurred reflection model to the full 0.3 – 8 keV band. The results were consistent with those of the time-resolved spectral fitting: the disk line model required an inclination significantly less than that of the blurred reflection.

- Theoretical estimates on the emission radii of disk hot spots and a single double-peaked profile were examined and show, to first-order, both scenarios can explain the time-resolved spectra equally well. Transient hot spots would originate from two locations, 25 – 60$R_{\rm g}$ and 8 – 10$R_{\rm g}$, to produce the features observed. Alternatively, a disk line would originate from about 30$R_{\rm g}$.

- If a disk line scenario were adopted, it would indicate a concave "divot" or warp in the accretion disk itself.

Further observations must be made to uncover the true nature of the red feature and confirm whether or not it is truly evidence of transient hot spots or a warp in a supermassive black hole accretion disk. Due to the apparent longevity of the feature across the 2015 epochs as well as its short-term variability, we remain hopeful that another observing campaign may capture this phenomenon.

Acknowledgments

The *XMM-Newton* project is an ESA Science Mission with instruments and contributions directly funded by ESA Member States and the USA (NASA).

Chapter 5

Conclusions

Going forward, the future of X-ray astrophysics looks bright. The *NuStar* mission continues to expand AGN observations to higher energies, *ATHENA* is on track to launch in 2028, and now *XARM* – the X-ray Astronomy Recovery Mission – has been announced as a collaboration between NASA and JAXA to rehabilitate *Hitomi* science. Astronomers are in a prime position to work with data of unprecedented quality while also utilizing advanced statistical tools and methodologies formerly reserved for more data-wealthy fields like finance and medical imaging. We are on the cusp of discovering fundamental truths about AGN at the smallest scales with broad implications for these objects and galaxy evolution as a whole. Within the next 10 – 15 years the true nature of the primary X-ray emitter, the corona, will be realized. We will be able to resolve finer atomic features in the blurred reflection spectrum and that along with an expanded bandpass will allow for robust measurements of ionization, emissivity index, and black hole spin. These findings will also break the degeneracies between blurred reflection and absorption models, putting to rest old debates while expanding our studies of complex objects. From there, the connection between accretion and radio jet activity will be more fully understood, propelling the understanding of evolutionary theory of AGN to the level of their lower-mass counterparts.

With the advancement of observations and technique, however, we must remain critical of our own methodologies to ensure the limits of our practices – whether involving complex simulations or

toy model fitting – are well defined. Our data are only as good as the uncertainties that accompany them and our work will always be bounded by, as one of my students put it: "the bars of truth." Astrophysics outside of our solar system is especially challenging as we are limited to the light that eventually reaches us, after a very long journey, and cannot (yet!) send probes or take physical samples of our subjects under study. We must carefully impose constraints on our models and tailor our methods to extract the most from our data while also remaining as unbiased as possible – it is a challenge! A reasonable approach to the problem is to systematically evaluate a common analytical method, uncover any weaknesses or blind spots that may be unrealized, and then apply the lessons learned to empirical data.

The work in Chapter 2 addresses the need for a conservative assessment on the standard practice of measuring supermassive black hole spin and other key X-ray spectral parameters using a limited bandpass, single epoch, and common models. It is by no means a comprehensive assessment and can be further expanded upon in numerous ways in order to probe the efficacies of particular spectroscopy practices. That said, it gets the ball rolling by addressing the ability to measure common Type I Seyfert spectral parameters under the simplest and most ideal conditions. As high-energy optics improves, providing unprecedented X-ray spectral resolution and wider bandpass, it is important to confirm the limits of such standard procedures – not to discourage work with less-than-ideal data but to encourage confidence in all AGN spectral studies – and to build on a list of best-practices that has been growing once the possibility of measuring supermassive black hole spin became reality.

Upon completion of our simulated X-ray spectral analysis, in which ideal spectra having counts above the previously established limit for spin measurements are created with parameters representative of average Seyfert I AGN and are fit mimicking common techniques, we are able to confirm the following:

1. Photon index, Γ, is able to be well-constrained within $\lesssim 10\%$ with standard deviation improving as reflection fraction decreases, although values tend to nearly always be

over-estimated.

2. Iron abundance, A_{Fe}, and inclination angle, θ, are both constrained within $\lesssim 20\%$ for the case of R = 1 and improving to around 10% when reflection fraction increases to R = 5.

3. The precision of A_{Fe} measurement is inversely proportional to intrinsic (i.e. input) A_{Fe} value and, interestingly, values tend to be over-estimated when ionization, ξ, is fixed and under-estimated when inner emissivity index, q_1, is fixed.

4. ξ is unable to be constrained under most circumstances and nearly all measurements were significantly under-estimated. Precision improves as the measured bandpass is extended from 2.5 – 10 keV up to 70 keV, but measurements cannot be considered robust until reflection fraction also increases to R = 5 in addition to the wider bandpass and then only for intrinsic values $\lesssim 200\,\mathrm{erg\,cm\,s^{-1}}$.

5. Black hole spin, a, is best constrained under the scenario of prograde spin and high reflection fraction, measured between 2.5 – 10 keV, with measurement precision increasing with intrinsic a value. Extending the observed bandpass to 70 keV will likely improve spin measurements as well when data are allowed to overlap, as is the case for current simultaneous *XMM-Newton* and *NuStar* observations.

6. q_1 is not able to be constrained under any of the conditions examined here and likely requires observations of the soft-excess below 1 keV as well as more detailed fitting of the Fe Kα line profile for measurement – contingent on the point above.

In summary, the ability of observers to confidently measure AGN X-ray spectral parameters depends on *which* parameters specifically they are attempting to constrain. If disk parameters A_{Fe}, ξ, or θ are of primary concern then a high reflection fraction and extended bandpass will enable the most robust measurements. However, if a robust measurement black hole spin is the main objective, observers would do best to stick to the 2.5 – 10 keV bandpass to limit falling into local minima

during the model fitting process. If an object has a high reflection fraction and high (> 0.8) intrinsic spin, then one can be confident their measurement is sound to $\pm 10\%$.

While the above analysis was performed for ideal X-ray spectra, with $>$ 200,000 counts between 2 – 10 keV, we can utilize the knowledge for improving analysis of dimmer and/or more complex spectra as well. The deep, multi-epoch analysis of Mrk 493 in Chapter 3 put into practice the points discussed in Chapter 2: averaging $\sim$ 14,000 counts in the 2 – 10 keV band, a robust estimate of supermassive black hole spin would not be possible with the current data. However, we can be confident in constraining disk parameters such as ionization due to the multi-epoch data, reflection fraction > 1, and inclusion of the soft-excess. This became important, as it appears that the primary driver of short-term X-ray variability in this object can in fact be attributed to changes in ionization. Aware of the limits spectroscopy alone can impose, the analysis of Mrk 493 was spearheaded by model-independent methods that revealed the complex nature of short-term variability in this object – a detail that could have easily become lost among model degeneracies, as is common. In particular, we find that both the primary component and the blurred reflector change on 25 ks timescales, with changes in ionization driving the soft-band variability during times of more rapid (< 25 ks) variations in continuum flux. Across the two 2015 epochs as a whole, variability is also described best by changes in ionization.

A particular model-independent method, time-resolved PCA, detected evidence of an additional source of variability between 4 – 5 keV that was unaccounted for by the single blurred reflector model which described the behaviour of the spectra well overall. In addition, time-resolved analysis saw the soft-excess dropping in flux 25 ks before the spectrum > 4 keV, a phenomenon that also cannot occur with a single blurred reflection component. Further investigation into the potential source of this red feature were described in Chapter 4, including flux-resolved analysis and disk line modelling. In the end, the 4 – 5 keV feature is not significant enough to draw any robust conclusions via spectroscopy, although discussions on hypothetical potential sources suggest transient hot spots or a divot in the accretion disk itself could reasonably produce the behaviours of both the red feature and Fe Kα line seen here.

Ultimately, this work serves as a basis upon which to build. The spin study may be easily expanded to include model parameter co-dependencies, alternative instrument responses, or alternative spectral models. Future observations of Mrk 493 could continue to find this object in a reflection-dominated state and it would be particularly fruitful if we catch it returning to higher-flux, for comparison. With that in mind, we are successful in being able to show the power of model-independent methods in driving exploratory analysis, especially for less-luminous objects. And when it comes to spectral modelling specifically, we quantify the ability of popular modelling methods to accurately measure key X-ray spectral parameters, constraining our ability to measure supermassive black hole spin and allowing future studies to optimize their work for best results (Bentz et al., 2016; Wang et al., 2017; Coziol et al., 2017). As our tools and techniques in high-energy astrophysics continue to advance, such work will only improve. It is truly an exciting time for AGN X-ray astronomy as we catch glimpses of the future, right around the corner.

Bibliography

Abbott, B. P. et al. (2016). Observation of Gravitational Waves from a Binary Black Hole Merger. *Physical Review Letters*, 116(6):061102.

Abdo, A. A. et al. (2009). Radio-Loud Narrow-Line Seyfert 1 as a New Class of Gamma-Ray AGN. *The Astrophysical Journal*, 707:L142–L147.

Barret, D. et al. (2016). The Athena X-ray Integral Field Unit (X-IFU). *Proceedings of the SPIE*, 9905:41.

Beckmann, V. and Shrader, C. R. (2012). *Active galactic nuclei*. Wiley-VCH, Weinheim, Germany.

Belczynski, K., Wiktorowicz, G., Fryer, C., Holz, D., and Kalogera, V. (2012). Missing Black Holes Unveil The Supernova Explosion Mechanism. *The Astrophysical Journal*, 757(1):91,6.

Bentz, M. C. et al. (2013). The Low-Luminosity End of the Radius-Luminosity Relationship for Active Galactic Nuclei. *The Astrophysical Journal*, 767(2):149,27.

Bentz, M. C. et al. (2016). A Low-Mass Black Hole in the Nearby Seyfert Galaxy UGC 06728. *The Astrophysical Journal*, 831(1):2,10.

Berton, M. et al. (2016). Compact steep-spectrum sources as the parent population of flat-spectrum radio-loud NLS1s. *Astronomy & Astrophysics*, 591:A98,9.

Blandford, R. D. and Znajek, R. L. (1977). Electromagnetic extraction of energy from Kerr black holes. *Monthly Notices of the Royal Astronomical Society*, 179(3):433–456.

Boissay, R., Ricci, C., and Paltani, S. (2016). A hard X-ray view of the soft excess in AGN. *Astronomy & Astrophysics*, 588:A70,19.

Bolton, C. T. (1972). Dimensions of the Binary System HDE 226868 = Cygnus X-1. *Nature*, 240(102):124–127.

Bonson, K. and Gallo, L. C. (2016). How well can we measure supermassive black hole spin? *Monthly Notices of the Royal Astronomical Society*, 458(2):1927–1938.

Bonson, K., Gallo, L. C., and Vasudevan, R. (2015). Is HE 0436-4717 Anemic? A deep look at a bare Seyfert 1 galaxy. *Monthly Notices of the Royal Astronomical Society*, 450(1):857–872.

Bourne, M. A., Nayakshin, S., and Hobbs, A. (2014). Black hole feedback in a multiphase interstellar medium. *Monthly Notices of the Royal Astronomical Society*, 441(4):3055–3064.

Bowyer, S., Byram, E. T., Chubb, T. A., and Friedman, H. (1964). Lunar Occultation of X-ray Emission from the Crab Nebula. *Science*, 146(3646):912–917.

Bradt, H. V. D., Ohashi, T., and Pounds, K. A. (1992). X-Ray Astronomy Missions. *Annual Review of Astronomy and Astrophysics*, 30(1):391–427.

Brenneman, L. and Laura (2013). Measuring Supermassive Black Hole Spins in AGN. *Acta Polytechnica*, 53:652.

Brenneman, L. W. et al. (2011). The Spin of the Supermassive Black Hole in NGC 3783. *The Astrophysical Journal*, 736(2):103,10.

Brenneman, L. W. and Reynolds, C. S. (2006). Constraining Black Hole Spin via X-Ray Spectroscopy. *The Astrophysical Journal*, 652(2):1028–1043.

Brenneman, L. W. and Reynolds, C. S. (2009). Relativistic Broadening of Iron Emission Lines in a Sample of AGN. *The Astrophysical Journal*, 702(2):1367–1386.

Broderick, A. E., Loeb, A., and Narayan, R. (2009). The Event Horizon of Sagittarius A*. *The Astrophysical Journal*, 701(2):1357–1366.

Cackett, E. M. et al. (2014). Modelling the broad Fe K-alpha reverberation in the AGN NGC 4151. *Monthly Notices of the Royal Astronomical Society*, 438(4):2980–2994.

Cappi, M. (2006). Relativistic blue- and red-shifted absorption lines in AGNs. *Astronomische Nachrichten*, 327(10):1012.

Castello-Mor, N., Netzer, H., and Kaspi, S. (2016). Super- and sub-Eddington accreting massive black holes: A comparison of slim and thin accretion discs through study of the spectral energy distribution. *Monthly Notices of the Royal Astronomical Society*, 458(2):1839–1858.

Chatterjee, S., Rodriguez, C. L., and Rasio, F. A. (2016). Binary Black Holes in Dense Star Clusters: Exploring the Theoretical Uncertainties. *The Astrophysical Journal*, 834(1):68,22.

Chiang, J. and Murray, N. (1996). Reverberation Mapping and the Disk Wind Model of the Broad Line Region. *Astrophysical Journal*, 466:704.

Collinson, J. S., Ward, M. J., Landt, H., Done, C., Elvis, M., and McDowell, J. C. (2017). Reaching the Peak of the quasar spectral energy distribution - II. Exploring the accretion disc, dusty torus and host galaxy. *Monthly Notices of the Royal Astronomical Society*, 465(1):358–382.

Cowperthwaite, P. S. and Reynolds, C. S. (2012). The Central Engine Structure of 3C120: Evidence for a Retrograde Black Hole or a Refilling Accretion Disk. *The Astrophysical Journal Letters*, 752(2):L21,5.

Coziol, R., Andernach, H., Ortega-Minakata, J. P. T.-P. R. A., del Rio, F. M., and Moreno del Rio, F. (2017). What sparks the radio-loud phase of nearby quasars? *Monthly Notices of the Royal Astronomical Society*, 466(1):921–944.

Czerny, B. and Goosmann, R. (2004). Flare-induced fountains and buried flares in AGN. *Astronomy and Astrophysics*, 428:353–363.

Dadina, M., Cappi, M., Malaguti, G., Ponti, G., and De Rosa, A. (2005). X-ray absorption lines suggest matter infalling onto the central black-hole of Mrk 509. *Astronomy and Astrophysics*, 442(2):461–468.

Dauser, T., Garcia, J., Wilms, J., Böck, M., Brenneman, L. W., Falanga, M., Fukumura, K., and Reynolds, C. S. (2013). Irradiation of an Accretion Disc by a Jet: General Properties and Implications for Spin Measurements of Black Holes. *Monthly Notices of the Royal Astronomical Society*, 430(3):1694–1708.

Davis, S. W. and Laor, A. (2011). The Radiative Efficiency of Accretion Flows in Individual AGN. *The Astrophysical Journal*, 728(2):98,19.

den Herder, J. W. et al. (2001). The Reflection Grating Spectrometer on board XMM-Newton. *Astronomy and Astrophysics*, 365(1):L7–L17.

Doi, A., Nagira, H., Kawakatu, N., Kino, M., Nagai, H., and Asada, K. (2012). Kiloparsec-scale Radio Structures in Narrow-line Seyfert 1 Galaxies. *The Astrophysical Journal*, 760(1):41,11.

Done, C., Davis, S., Jin, C., Blaes, O., and Ward, M. (2012). Intrinsic disc emission and the Soft X-ray Excess in AGN. *Monthly Notices of the Royal Astronomical Society*, 420(3):1848–1860.

Done, C., Jin, C., Middleton, M., and Ward, M. (2013). A new way to measure supermassive black hole spin in accretion disc dominated Active Galaxies. *Monthly Notices of the Royal Astronomical Society*, 434(3):1955–1963.

Done, C. and Nayakshin, S. (2007). Can the soft excess in AGN originate from disc reflection? *Monthly Notices of the Royal Astronomical Society*, 377(3):L59–L63.

Dubois, Y. et al. (2014). Dancing in the dark: galactic properties trace spin swings along the cosmic web. *Monthly Notices of the Royal Astronomical Society*, 444(2):1453–1468.

Dunn, R. J. H. and Fabian, A. C. (2006). Investigating AGN Heating in a Sample of Nearby Clusters. *Monthly Notices of the Royal Astronomical Society*, 373(3):959–971.

Edelson, R., Turner, T. J., Pounds, K., Vaughan, S., Markowitz, A., Marshall, H., Dobbie, P., and Warwick, R. (2002). X-ray Spectral Variability and Rapid Variability of the Soft X-ray Spectrum Seyfert 1 Galaxies Ark 564 and Ton S180. *The Astrophysical Journal*, 568(2):610–626.

Elitzur, M. and Shlosman, I. (2006). The AGN Obscuring Torus – End of the "Doughnut" Paradigm? *The Astrophysical Journal*, 648(2):L101–L104.

Elvis, M. et al. (1994). Atlas of quasar energy distributions. *The Astrophysical Journal Supplement Series*, 95:1.

Emmanoulopoulos, D., Papadakis, I. E., Epitropakis, A., Pecháček, T., Dovčiak, M., and McHardy, I. M. (2016). A search for X-ray reprocessing echoes in the power spectral density functions of AGN. *Monthly Notices of the Royal Astronomical Society, Volume 461, Issue 2, p.1642-1655*, 461:1642–1655.

Fabian, A. C. (2012). Observational Evidence of AGN Feedback. *Annual Review of Astronomy and Astrophysics*, 50:455–489.

Fabian, A. C. et al. (2009). Broad line emission from iron K- and L-shell transitions in the active galaxy 1H 0707-495. *Nature*, 459(7246):540–2.

Fabian, A. C. et al. (2012). 1H0707-495 in 2011: An X-ray source within a gravitational radius of the event horizon. *Monthly Notices of the Royal Astronomical Society*, 419(1):116–123.

Fabian, A. C. et al. (2013). Long XMM observation of the Narrow-Line Seyfert 1 galaxy IRAS13224-3809: rapid variability, high spin and a soft lag. *Monthly Notices of the Royal Astronomical Society*, 429(4):2917–2923.

Fabian, A. C., Lohfink, A., Kara, E., Parker, M. L., Vasudevan, R., and Reynolds, C. S. (2015). Properties of AGN coronae in the NuSTAR era. *Monthly Notices of the Royal Astronomical Society*, 451(4):4375–4383.

Fabian, A. C., Rees, M. J., Stella, L., and White, N. E. (1989). X-ray fluorescence from the inner disc in Cygnus X-1. *Monthly Notices of the Royal Astronomical Society*, 238(3):729–736.

Fedorova, E., Vasylenko, A., Hnatyk, B. I., and Zhdanov, V. I. (2016). The peculiar megamaser AGN NGC 1194: Comparison with the warped disk candidates NGC 1068 and NGC 4258. *Astronomische Nachrichten*, 337(1-2):96–100.

Feigelson, E. D. and Babu, G. J. (1992). Linear regression in astronomy. II. *The Astrophysical Journal*, 397:55.

Foreman-Mackey, D., Hogg, D. W., Lang, D., and Goodman, J. (2013). emcee: The MCMC Hammer. *Publications of the Astronomical Society of Pacific*, 125(925):306.

Furui, S., Fukazawa, Y., Odaka, H., Kawaguchi, T., Ohno, M., and Hayashi, K. (2016). X-ray Spectral Model of Reprocessing by Smooth and Clumpy Molecular Tori in Active Galactic Nuclei with the MONACO framework. *The Astrophysical Journal*, 818(2):164,19.

Gabor, J. M. and Bournaud, F. (2014). AGN-driven outflows without immediate quenching in simulations of high-redshift disk galaxies. *Monthly Notices of the Royal Astronomical Society*, 441(2):1615–1627.

Gallimore, J. F. et al. (2016). High-Velocity Bipolar Molecular Emission from an AGN Torus. *The Astrophysical Journal Letters*, 829(1):L7,5.

Gallo, L. C. (2011). Revealing the Innermost Regions of Active Galaxies. *Journal of the Royal Astronomical Society of Canada*, 105(4):143.

Gallo, L. C., Brandt, W. N., Costantini, E., and Fabian, A. C. (2007). A longer XMM-Newton look at I Zwicky 1: Distinct modes of X-ray spectral variability. *Monthly Notices of the Royal Astronomical Society*, 377(3):1375–1382.

Gallo, L. C. et al. (2013). A blurred reflection interpretation for the intermediate flux state in Mrk 335. *Monthly Notices of the Royal Astronomical Society*, 428(2):1191–1200.

Gallo, L. C. et al. (2015). Suzaku observations of Mrk 335: Confronting partial covering and relativistic reflection. *Monthly Notices of the Royal Astronomical Society*, 446(1):633–650.

Gallo, L. C., Miniutti, G., Miller, J. M., Brenneman, L. W., Fabian, A. C., Guainazzi, M., and Reynolds, C. S. (2011). Multi-epoch X-ray observations of the Seyfert 1.2 galaxy Mrk 79: bulk motion of the illuminating X-ray source. *Monthly Notices of the Royal Astronomical Society*, 411(1):607–619.

Garcia, J., Dauser, T., Reynolds, C. S., Kallman, T. R., McClintock, J. E., Wilms, J., and Eikmann, W. (2013). X-ray reflected spectra from accretion disk models. III. A complete grid of ionized reflection calculations. *The Astrophysical Journal*, 768(2):146,20.

Gebhardt, K. et al. (2000). A Relationship Between Nuclear Black Hole Mass and Galaxy Velocity Dispersion. *The Astrophysical Journal*, 539(1):L13–L16.

Ghisellini, G., Haardt, F., and Matt, G. (2004). Aborted jets and the X-ray emission of radio-quiet AGNs. *Astronomy and Astrophysics*, 413:535–545.

Giacconi, R. et al. (1979). The Einstein HEAO 2 X-ray Observatory. *The Astrophysical Journal*, 230:540.

Giacconi, R., Gursky, H., Paolini, F. R., and Rossi, B. B. (1962). Evidence for X-Rays From Sources Outside the Solar System. *Physical Review Letters*, 9(11):439–443.

Giacconi, R., Kellogg, E., Gorenstein, P., Gursky, H., and Tananbaum, H. (1971). An X-Ray Scan of the Galactic Plane from UHURU. *The Astrophysical Journal*, 165:L27.

Giacconi, R., Reidy, W. P., Vaiana, G. S., Van Speybroeck, L. P., and Zehnpfennig, T. F. (1969). Grazing-incidence telescopes for X-ray astronomy. *Space Science Reviews*, 9(1):3–57.

Giustini, M. et al. (2017). Direct probe of the inner accretion flow around the supermassive black hole in NGC 2617. *Astronomy and Astrophysics*, 597:A66,13.

Gofford, J., Reeves, J. N., McLaughlin, D. E., Braito, V., Turner, T. J., Tombesi, F., and Cappi, M. (2015). The Suzaku view of highly-ionised outflows in AGN: II – Location, energetics and scalings with Bolometric Luminosity. *Monthly Notices of the Royal Astronomical Society*, 451(4):4169–4182.

Gofford, J., Reeves, J. N., Tombesi, F., Braito, V., Turner, T. J., Miller, L., and Cappi, M. (2013). The Suzaku view of highly-ionised outflows in AGN: I - Statistical detection and global absorber properties. *Monthly Notices of the Royal Astronomical Society*, 430(1):60–80.

Gondoin, P., Orr, A., Lumb, D., and Santos-Lleo, M. (2002). XMMNewton observations of the Seyfert 1 galaxy Mrk 335. *Astronomy and Astrophysics*, 388(1):74–87.

Gonzalez, A., Gallo, L. C., and Wilkins, D. R. (2017). No Title. *MNRAS*, page (in review).

Gonzalez-Martin, O. and Vaughan, S. (2012). X-ray variability of 104 active galactic nuclei. XMM-Newton power-spectrum density profiles. *Astronomy and Astrophysics*, 544:A80,57.

Goodman, J. and Weare, J. (2010). No Title. *Comm. App. Math. Comp. Sci.*, 5:65.

Grupe, D. (2004). A Complete Sample of Soft X-ray Selected AGN: II. Statistical Analysis. *The Astronomical Journal*, 127(4):1799–1810.

Grupe, D., Komossa, S., Leighly, K., and Page, K. (2010). The Simultaneous Optical-to-X-Ray Spectral Energy Distribution of Soft X-Ray Selected Active Galactic Nuclei Observed by Swift. *Monthly Notices of the Royal Astronomical Society*, 187(1):64,106.

Grupe, D., Komossa, S., and Saxton, R. (2015). IC 3599 Did It Again: A Second Outburst of the X-Ray Transient Seyfert 1.9 Galaxy. *The Astrophysical Journal Letters*, 803(2):L28,5.

Guainazzi, M. (2003). The history of the iron K-alpha line profile in the Piccinotti AGN ESO198-G24. *Astronomy and Astrophysics*, 401:903–910.

Guainazzi, M., Bianchi, S., and Dovciak, M. (2006). Statistics of relativistically broadened Fe K-alpha lines in AGN. *Astronomische Nachrichten*, 327(10):1032.

Harms, R. J. et al. (1994). HST FOS spectroscopy of M87: Evidence for a disk of ionized gas around a massive black hole. *The Astrophysical Journal*, 435:L35.

Harrison, C. M., Alexander, D. M., Mullaney, J. R., and Swinbank, A. M. (2014). Kiloparsec-scale outflows are prevalent among luminous AGN: outflows and feedback in the context of the overall AGN population. *Monthly Notices of the Royal Astronomical Society*, 441(4):3306–3347.

Harrison, F. A. et al. (2013). The Nuclear Spectroscopic Telescope Array (NuSTAR) Mission. *The Astrophysical Journal*, 770(2):103,19.

Hitomi Collaboration (2017). Hitomi constraints on the 3.5 keV line in the Perseus galaxy cluster. *The Astrophysical Journal Letters*, 837(1):L15,9.

Ho, L. C., Filippenko, A. V., and Sargent, W. L. W. (1997). A Search for "Dwarf" Seyfert Nuclei. V. Demographics of Nuclear Activity in Nearby Galaxies. *The Astrophysical Journal*, 487(2):568–578.

Ho, L. C. and Kim, M. (2015). A Revised Calibration of the Virial Mass Estimator for Black Holes in Active Galaxies Based on Single-epoch H-beta Spectra. *The Astrophysical Journal*, 809(2):123,4.

Hughes, S. A. and Blandford, R. D. (2003). Black hole mass and spin coevolution by mergers. *The Astrophysical Journal*, 585(2):L101–L104.

Hurlburt, S. (2013). *Strong Fe K fluorescent emission in type-1 Seyfert galaxies*. PhD thesis, Saint Mary's University.

Iwasawa, K., Miniutti, G., and Fabian, A. C. (2004). Flux and energy modulation of redshifted iron emission in NGC 3516: implications for the black hole mass. *Monthly Notices of the Royal Astronomical Society*, 355(4):1073–1079.

Järvelä, E., Lähteenmäki, A., and León-Tavares, J. (2015). Statistical multifrequency study of narrow-line Seyfert 1 galaxies. *Astronomy and Astrophysics*, 573:A76,24.

Jiang, Y.-F., Stone, J. M., and Davis, S. W. (2014). A Global Three Dimensional Radiation Magneto-hydrodynamic Simulation of Super-Eddington Accretion Disks. *The Astrophysical Journal*, 796(2):106,14.

Jin, C., Ward, M., and Done, C. (2012). A Combined Optical and X-ray Study of Unobscured Type 1 AGN. II. Relation Between X-ray Emission and Optical Spectra. *Monthly Notices of the Royal Astronomical Society*, 422(4):3268–3284.

Kalberla, P. M. W., Burton, W. B., Hartmann, D., Arnal, E. M., Bajaja, E., Morras, R., and Poppel, W. G. L. (2005). The Leiden/Argentine/Bonn (LAB) Survey of Galactic HI: Final data release of the combined LDS and IAR surveys with improved stray-radiation corrections. *Astronomy and Astrophysics*, 440(2):775–782.

Kara, E., Alston, W. N., Fabian, A. C., Cackett, E. M., Uttley, P., Reynolds, C. S., and Zoghbi, A. (2016). A global look at X-ray time lags in Seyfert galaxies. *Monthly Notices of the Royal Astronomical Society*, 462(1):511–531.

Kaspi, S., Smith, P. S., Netzer, H., Maoz, D., Jannuzi, B. T., and Giveon, U. (2000). Reverberation Measurements for 17 Quasars and the Size-Mass-Luminosity Relations in Active Galactic Nuclei. *The Astrophysical Journal*, 533(2):631–649.

Keck, M. L. et al. (2015). NuSTAR and Suzaku X-ray Spectroscopy of NGC 4151: Evidence for Reflection from the Inner Accretion Disk. *The Astrophysical Journal*, 806(2):149,17.

Kellermann, K. I., Sramek, R., Schmidt, M., Shaffer, D. B., and Green, R. (1989). VLA observations of objects in the Palomar Bright Quasar Survey. *The Astronomical Journal*, 98:1195.

Kerr, R. P. (1963). No Title. *Physical Review Letters*, 11:237.

King, A. (2008). Disc accretion in active galactic nuclei. *New Astronomy Reviews*, 52(6):253–256.

King, A. L., Lohfink, A., and Kara, E. (2017). AGN Coronae Through A Jet Perspective. *The Astrophysical Journal*, 835(2):226,13.

King, A. L., Miller, J. M., Bietenholz, M., Gultekin, K., Reynolds, M., Mioduszewski, A., Rupen, M., and Bartel, N. (2015). The Rate of Gas Accretion onto Black Holes Drives Jet Velocity. *The Astrophysical Journal Letters*, 799(1):L8,5.

King, A. R. (2010). Black Hole Outflows. *Monthly Notices of the Royal Astronomical Society*, 402(3):1516–1522.

King, A. R. and Pringle, J. E. (2006). Growing Supermassive Black Holes by Chaotic Accretion. *Monthly Notices of the Royal Astronomical Society*, 373(1):L90–L92.

King, A. R. and Pringle, J. E. (2007). Fuelling Active Galactic Nuclei. *Monthly Notices of the Royal Astronomical Society*, 377(1):L25–L28.

Koratkar, A. and Blaes, O. (1999). Invited Review: The Ultraviolet and Optical Continuum Emission in Active Galactic Nuclei: The Status of Accretion Disks. *Publications of the Astronomical Society of the Pacific*, 111(755):1–30.

Kormendy, J. and Ho, L. C. (2013). Coevolution (Or Not) of Supermassive Black Holes and Host Galaxies. *Annual Review of Astronomy and Astrophysics*, 51(1):511–653.

Kruper, J. S., Canizares, C. R., and Urry, C. M. (1990). Soft X-ray properties of Seyfert galaxies. I - Spectra. *The Astrophysical Journal Supplement Series*, 74:347.

Laor, A. and Netzer, H. (1989). Massive thin accretion discs - I. Calculated spectra. *Monthly Notices of the Royal Astronomical Society*, 238(3):897–916.

Lee, S. (1962). "Spider-Man!". *Marvel Comics*, page Issue #15.

Li, Y. (2012). *Tian wen xue bao = Acta astronomica Sinica*, volume 53. Ke xue chu ban she.

Li, Y.-R., Wang, J.-M., Ho, L. C., Du, P., and Bai, J.-M. (2013). A Bayesian Approach to Estimate the Size and Structure of the Broad-line Region in Active Galactic Nuclei Using Reverberation Mapping Data. *The Astrophysical Journal*, 779(2):110,17.

Lohfink, A. M. et al. (2013). An X-Ray View of the Jet-Cycle in the Radio Loud AGN 3C120. *The Astrophysical Journal*, 772(2):83,13.

Lohfink, A. M., Reynolds, C. S., Miller, J. M., Brenneman, L. W., Mushotzky, R. F., Nowak, M. A., and Fabian, A. C. (2012). The Black Hole Spin and Soft X-ray Excess of the Luminous Seyfert Galaxy Fairall 9. *The Astrophysical Journal*, 758(1):67,11.

Marinucci, A. et al. (2014). The broad band spectral variability of MCG-6-30-15 observed by NuSTAR and XMM-Newton. *The Astrophysical Journal*, 787(1):83,17.

Markowitz, A., Reeves, J. N., George, I. M., Braito, V., Smith, R., Vaughan, S., Arévalo, P., and Tombesi, F. (2009). A Comprehensive X-ray Spectral Analysis of the Seyfert 1.5 NGC 3227. *The Astrophysical Journal*, 691(2):922–945.

Martizzi, D., Teyssier, R., and Moore, B. (2013). Cusp-core transformations induced by AGN feedback in the progenitors of cluster galaxies. *Monthly Notices of the Royal Astronomical Society*, 432(3):1947–1954.

Mason, K. O. et al. (2001). The XMM-Newton Optical/UV Monitor Telescope. *Astronomy and Astrophysics*, 365:L36–L44.

Mateos, S. et al. (2016). X-ray absorption, nuclear infrared emission and dust covering factors of AGN: testing Unification Schemes. *The Astrophysical Journal*, 819(2):166,12.

Mathur, S., Fields, D., Peterson, B. M., and Grupe, D. (2012). Supermassive black holes, pseudobulges, and the narrow-line Seyfert 1 galaxies. *The Astrophysical Journal*, 754(2):146,9.

McNamara, B. R. and Nulsen, P. E. J. (2007). Heating Hot Atmospheres with Active Galactic Nuclei. *Annual Review of Astronomy and Astrophysics*, 45(1):117–175.

Meidinger, N., Eder, J., Eraerds, T., Nandra, K., Pietschner, D., Plattner, M., Rau, A., and Strecker, R. (2017). The Wide Field Imager Instrument for Athena. *eprint arXiv:1702.01079*.

Mejía-Restrepo, J. E., Trakhtenbrot, B., Lira, P., Netzer, H., and Capellupo, D. M. (2016). Active galactic nuclei at z˜1.5: II. Black Hole Mass estimation by means of broad emission lines. *Monthly Notices of the Royal Astronomical Society*, 460(1):187–211.

Merloni, A. et al. (2013). The incidence of obscuration in active galactic nuclei. *Monthly Notices of the Royal Astronomical Society*, 437(4):3550–3567.

Merloni, A. and Fabian, A. (2001). Thunderclouds and accretion discs: a model for the spectral and temporal variability of Seyfert 1 galaxies. *Monthly Notices of the Royal Astronomical Society*, 328(3):958–968.

Merloni, A., Heinz, S., and Di Matteo, T. (2003). A fundamental plane of black hole activity. *Monthly Notices of the Royal Astronomical Society*, 345(4):1057–1076.

Miller, J. M. (2006). A Short Review of Relativistic Iron Lines from Stellar-Mass Black Holes. *Astronomische Nachrichten*, 327(10):997.

Miller, J. M. (2007). Relativistic X-ray Lines from the Inner Accretion Disks Around Black Holes. *Annual Review of Astronomy and Astrophysics*, 45(1):441–479.

Miller, J. M. and Homan, J. (2005). Evidence for a Link Between Fe K-alpha Emission Line Strength and QPO Phase in a Black Hole. *The Astrophysical Journal*, 618(2):L107–L110.

Miller, L., Turner, T. J., and Reeves, J. N. (2008). An absorption origin for the X-ray spectral variability ofMCG6-30-15. *Astronomy and Astrophysics*, 483(2):437–452.

Miller, L., Turner, T. J., and Reeves, J. N. (2009). The absorption-dominated model for the X-ray spectra of type I active galaxies: MCG-6-30-15. *Monthly Notices of the Royal Astronomical Society*, 399(1):L69–L73.

Miller, L., Turner, T. J., Reeves, J. N., Lobban, A., Kraemer, S. B., and Crenshaw, D. M. (2010). Spectral variability and reverberation time delays in the Suzaku X-ray spectrum of NGC 4051. *Monthly Notices of the Royal Astronomical Society*, 403(1):196–210.

Miller, M. C. and Krolik, J. H. (2013). Alignment of supermassive black hole binary orbits and spins. *The Astrophysical Journal*, 774(1):43,8.

Miniutti, G. and Fabian, A. C. (2004). A light bending model for the X-ray temporal and spectral properties of accreting black holes. *Monthly Notices of the Royal Astronomical Society*, 349(4):1435–1448.

Mohan, P. and Mangalam, A. (2014). X-Ray Variability and the Inner Region in Active Galactic Nuclei. *The Astrophysical Journal*, 791(2):74,15.

Muñoz-Darias, T. et al. (2016). Regulation of black-hole accretion by a disk wind during a violent outburst of V404 Cygni. *Nature*, 534(7605):75–78.

Murdin, P. (2000). Michell, John (1724-93). In *The Encyclopedia of Astronomy and Astrophysics*. IOP Publishing Ltd.

Nandra, K. and Pounds, K. A. (1994). Ginga observations of the X-ray spectra of Seyfert galaxies. *Monthly Notices of the Royal Astronomical Society*, 268(2):405–429.

Nardini, E., Fabian, A. C., Reis, R. C., and Walton, D. J. (2011). A reflection origin for the soft and hard X-ray excess of Ark 120. *Monthly Notices of the Royal Astronomical Society*, 410(2):1251–1261.

Nelson, C. H. (2000). Black Hole Mass, Velocity Dispersion and the Radio Source in AGN. *The Astrophysical Journal*, 544(2):L91–L94.

Nelson, C. H. and Whittle, M. (1996). Stellar and Gaseous Kinematics of Seyfert Galaxies. II. The Role of the Bulge. *The Astrophysical Journal*, 465:96.

Novikov, I. and Thorne, K. (1973). Astrophysics of Black Holes. In DeWitt, C. and DeWitt, B., editors, *Black Holes*, pages 343–450. Gordon and Breach, Paris.

Nowak, M. A., Vaughan, B. A., Wilms, J., Dove, J. B., and Begelman, M. C. (1999). Rossi X-Ray Timing Explorer Observation of Cygnus X-1. II. Timing Analysis. *The Astrophysical Journal*, 510(2):874–891.

Oh, K. et al. (2017). BAT AGN Spectroscopic Survey-III. An observed link between AGN Eddington ratio and narrow emission line ratios. *Monthly Notices of the Royal Astronomical Society*, 464(2):1466–1473.

Papadakis, I., Pechacek, T., Dovciak, M., Epitropakis, A., Emmanoulopoulos, D., and Karas, V. (2016). Signatures of X-ray reverberation in the power spectra of AGN. *Astronomy & Astrophysics, Volume 588, id.A13, 6 pp.*, 588.

Parker, M. L. et al. (2015). Revealing the X-ray Variability of AGN with Principal Component Analysis. *Monthly Notices of the Royal Astronomical Society*, 447(1):72–96.

Parker, M. L., Marinucci, A., Brenneman, L., Fabian, A. C., Kara, E., Matt, G., and Walton, D. J. (2014a). Principal Component Analysis of MCG-6-30-15 with XMM-Newton. *Monthly Notices of the Royal Astronomical Society*, 437(1):721–729.

Parker, M. L., Walton, D. J., Fabian, A. C., and Risaliti, G. (2014b). PCA of PCA: Principal Component Analysis of Partial Covering Absorption in NGC 1365. *Monthly Notices of the Royal Astronomical Society*, 441(2):1817–1824.

Patrick, A. R., Reeves, J. N., Lobban, A. P., Porquet, D., and Markowitz, A. G. (2011a). Assessing black hole spin in deep Suzaku observations of Seyfert 1 AGN. *Monthly Notices of the Royal Astronomical Society*, 416(4):2725–2747.

Patrick, A. R., Reeves, J. N., Porquet, D., Markowitz, A. G., Braito, V., and Lobban, A. P. (2012).

A Suzaku survey of Fe K lines in Seyfert 1 AGN. *Monthly Notices of the Royal Astronomical Society*, 426(3):2522–2565.

Patrick, A. R., Reeves, J. N., Porquet, D., Markowitz, A. G., Lobban, A. P., and Terashima, Y. (2011b). Iron line profiles in Suzaku spectra of bare Seyfert galaxies. *Monthly Notices of the Royal Astronomical Society*, 411(4):2353–2370.

Penna, R. F., Sadowski, A., and McKinney, J. C. (2012). Thin Disk Theory with a Non-Zero Torque Boundary Condition and Comparisons with Simulations. *Monthly Notices of the Royal Astronomical Society*, 420(1):684–698.

Peterson, B. M. and Horne, K. (2004). Reverberation Mapping of Active Galactic Nuclei. *Astronomische Nachrichten*, 325(3):248–251.

Petrucci, P. O. et al. (2002). A rapidly variable narrow X-ray iron line in Mkn 841. *Astronomy and Astrophysics*, 388:L5–L8.

Ponti, G., Cappi, M., Dadina, M., and Malaguti, G. (2004). Mapping the inner regions of MCG-6-30-15 with XMM-Newton. *Astronomy and Astrophysics*, 417:451–459.

Porquet, D. et al. (2007). A 100ks XMM-Newton view of the Seyfert 1.8 ESO113-G010. I. Discovery of large X-ray variability and study of the FeK-alpha line complex. *Astronomy and Astrophysics*, 473(1):67–76.

Porquet, D., Reeves, J. N., Uttley, P., and Turner, T. J. (2004). XMM-Newton observation of the Seyfert 1.8 ESO 113-G010: discovery of a highly redshifted iron line at 5.4 keV. *Astronomy and Astrophysics*, 427:101–105.

Raginski, I. and Laor, A. (2016). AGN Coronal Emission models I. The Predicted Radio Emission. *Monthly Notices of the Royal Astronomical Society*, 459(2):2082–2096.

Reines, A. E., Greene, J. E., and Geha, M. (2013). Dwarf Galaxies with Optical Signatures of Active Massive Black Holes. *The Astrophysical Journal*, 775(2):116,24.

Reynolds, C. S. (2013). Astrophysics: Black holes in a spin. *Nature*, 494(7438):432–433.

Reynolds, C. S. (2014). Measuring Black Hole Spin using X-ray Reflection Spectroscopy. *Space Science Reviews*, 183(1-4):277–294.

Reynolds, C. S. (2016). Unwrapping the X-ray Spectra of Active Galactic Nuclei. *Astronomische Nachrichten*, 337(4-5):404.

Reynolds, C. S., Brenneman, L. W., Lohfink, A. M., Trippe, M. L., Miller, J. M., Fabian, A. C., and Nowak, M. A. (2012). A Monte Carlo Markov Chain based investigation of black hole spin in the active galaxy NGC3783. *The Astrophysical Journal*, 755(2):88,10.

Reynolds, C. S., Garofalo, D., and Begelman, M. C. (2006). Trapping of magnetic flux by the plunge region of a black hole accretion disk. *The Astrophysical Journal*, 651(2):1023–1030.

Reynolds, C. S. and Nowak, M. A. (2003). Fluorescent iron lines as a probe of astrophysical black hole systems. *Physics Reports*, 377(6):389–466.

Reynolds, C. S., Nowak, M. A., Markoff, S., Tueller, J., Wilms, J., and Young, A. J. (2009). Probing the accretion disk and central engine structure of NGC4258 with Suzaku and XMM-Newton observations. *The Astrophysical Journal*, 691(2):1159–1167.

Reynolds, C. S., Ward, M. J., Fabian, A. C., and Celotti, A. (1997). A multi-wavelength study of the Seyfert 1 galaxy MCG-6-30-15. *Monthly Notices of the Royal Astronomical Society*, 291:403.

Reynolds, C. S., Young, A. J., Begelman, M. C., and Fabian, A. C. (1999). X-ray iron line reverberation from black hole accretion disks. *The Astrophysical Journal*, 514:164–179.

Risaliti, G. (2016). Absorption from a multi-layer circumnuclear medium and reflection from the accretion disc in NGC 1365. *Astronomische Nachrichten*, 337(4-5):529–533.

Risaliti, G. et al. (2013). A rapidly spinning supermassive black hole at the centre of NGC 1365. *Nature*, 494(7438):449–451.

Rivers, E. et al. (2015). The Multi-Layer Variable Absorbers in NGC 1365 Revealed by XMM-Newton and NuSTAR. *The Astrophysical Journal*, 804(2):107,11.

Ross, R. R. and Fabian, A. C. (2005). A comprehensive range of X-ray ionized reflection models. *Monthly Notices of the Royal Astronomical Society*, 358(1):211–216.

Rovelli, C. and Vidotto, F. (2014). Planck stars. *International Journal of Modern Physics*, D23(12):1442026.

Rozanska, A., Malzac, J., Belmont, R., Czerny, B., and Petrucci, P. O. (2015). The existence of warm and optically thick dissipative coronae above accretion disks. *Astronomy and Astrophysics*, 580:A77,9.

Ruszkowski, M., Bruggen, M., and Begelman, M. C. (2003). Cluster Heating by Viscous Dissipation of Sound Waves. *The Astrophysical Journal*, 611(1):158–163.

Sandage, A. et al. (1966). On the optical identification of SCO X-1. *The Astrophysical Journal*, 146:316.

Sanfrutos, M., Miniutti, G., Dovčiak, M., and Agís-González, B. (2016). Eclipsing the innermost accretion disc regions in AGN. *Astronomische Nachrichten*, 337(4-5):546–551.

Schaye, J. et al. (2014). The EAGLE project: Simulating the evolution and assembly of galaxies and their environments. *Monthly Notices of the Royal Astronomical Society*, 446(1):521–554.

Seyfert, C. K. (1943). Nuclear Emission in Spiral Nebulae. *The Astrophysical Journal*, 97:28.

Shakura, N. I. and Sunyaev, R. A. (1973). *Astronomy and astrophysics.*, volume 24. EDP Sciences [etc.].

Shapiro, S. L. (2004). Spin, Accretion and the Cosmological Growth of Supermassive Black Holes. *The Astrophysical Journal*, 620(1):59–68.

Skibo, J. G. (1997). Spallation of Iron in Black Hole Accretion Flows. *The Astrophysical Journal*, 478(2):522–526.

Stern, J. and Laor, A. (2013). Type 1 AGN at low z. III. The optical narrow line ratios. *Monthly Notices of the Royal Astronomical Society*, 431(1):836–857.

Strüder, L. (2001). The European Photon Imaging Camera on XMM-Newton: The pn-CCD camera. *Astronomy and Astrophysics*, 365(1):L18–L26.

Sulentic, J. W., Zwitter, T., Marziani, P., and Dultzin-Hacyan, D. (2000). Eigenvector 1: An Optimal Correlation Space for Active Galactic Nuclei. *The Astrophysical Journal*, 536(1):L5,L9.

Takahashi, T. et al. (2014). The ASTRO-H X-ray Astronomy Satellite. *Proceedings of the SPIE*, 9144:24.

Tan, Y., Wang, J., Shu, X., and Zhou, Y. (2012). A possible ultra strong and broad Fe Ka emission line in Seyfert 2 galaxy IRAS 00521-7054. *The Astrophysical Journal Letters*, 747(1):L11,5.

Tanaka, Y. et al. (1995). Gravitationally redshifted emission implying an accretion disk and massive black hole in the active galaxy MCG-6-30-15. *Nature*, 375(6533):659–661.

Taylor, P. and Kobayashi, C. (2015). The Effects of AGN Feedback on Present-Day Galaxy Properties in Cosmological Simulations. *Monthly Notices of the Royal Astronomical Society*, 448(2):1835–1846.

Taylor, R. D., Uttley, P., and McHardy, I. M. (2003). The nature of X-ray spectral variability in Seyfert galaxies. *Monthly Notices of the Royal Astronomical Society*, 342(2):L31,L35.

Thorne, K. S. (1974). Disk-Accretion onto a Black Hole. II. Evolution of the Hole. *The Astrophysical Journal*, 191:507.

Tombesi, F. (2016). Accretion disk winds in active galactic nuclei: X-ray observations, models, and feedback. *Astronomische Nachrichten*, 337(4-5):410.

Tombesi, F., Cappi, M., Reeves, J. N., Palumbo, G. G. C., Yaqoob, T., Braito, V., and Dadina, M. (2010). Evidence for ultra-fast outflows in radio-quiet AGNs: I - detection and statistical incidence of Fe K-shell absorption lines. *Astronomy and Astrophysics*, 521:A57,35.

Turner, A. K., Fabian, A. C., Lee, J. C., and Vaughan, S. (2004). The soft X-ray absorption lines of the Seyfert 1 galaxy MCG–6-30-15. *Monthly Notices of the Royal Astronomical Society*, 353(1):319–328.

Turner, M. J. et al. (2001). The European Photon Imaging Camera on XMM-Newton: The MOS Cameras. *Astronomy and Astrophysics*, 365:L27–L35.

Turner, R. J. and Shabala, S. S. (2015). The Energetics and Lifetimes of Local Radio Active Galactic Nuclei. *The Astrophysical Journal*, 806(1):59,18.

Turner, T. J. and Miller, L. (2009). X-ray Absorption and Reflection in Active Galactic Nuclei. *The Astronomy and Astrophysics Review*, 17(1):47–104.

Turner, T. J. and Miller, L. (2010). Cosmic Ray Spallation in Radio-Quiet Active Galactic Nuclei: A Case Study of NGC 4051. *The Astrophysical Journal*, 709(2):1230–1237.

Uttley, P., Cackett, E. M., Fabian, A. C., Kara, E., and Wilkins, D. R. (2014). X-ray reverberation around accreting black holes. *The Astronomy and Astrophysics Review*, 22:72,66.

Uttley, P., McHardy, I. M., and Vaughan, S. (2005). Non-linear X-ray variability in X-ray binaries and active galaxies. *Monthly Notices of the Royal Astronomical Society*, 359(1):345–362.

Vasudevan, R. V. et al. (2014). The hard X-ray perspective on the soft X-ray excess. *The Astrophysical Journal*, 785(1):30,11.

Vasudevan, R. V., Fabian, A. C., Reynolds, C. S., Aird, J., Dauser, T., and Gallo, L. C. (2016). A selection effect boosting the contribution from rapidly spinning black holes to the Cosmic X-ray Background. *Monthly Notices of the Royal Astronomical Society*, 458(2):2012–2023.

Volonteri, M., Sikora, M., Lasota, J.-P., and Merloni, A. (2013). The evolution of active galactic nuclei and their spins. *The Astrophysical Journal*, 775(2):94,14.

Walton, D. J., Nardini, E., Fabian, A. C., Gallo, L. C., and Reis, R. C. (2013). Suzaku observations of 'bare' active galactic nuclei. *Monthly Notices of the Royal Astronomical Society*, 428(4):2901–2920.

Wang, Y., Ghasemi-Nodehi, M., Guainazzi, M., and Bambi, C. (2017). The Spin of the Supermassive Black Hole in MCG-05-23-16. *eprint arXiv:1703.07182*.

Werner, N. et al. (2013). The origin of cold gas in giant elliptical galaxies and its role in fueling radio-mode AGN feedback. *Monthly Notices of the Royal Astronomical Society*, 439(3):2291–2306.

Wilkes, B. J. and Elvis, M. (1987). Quasar energy distributions. I - Soft X-ray spectra of quasars. *The Astrophysical Journal*, 323:243.

Wilkins, D. R. (2016). Driving extreme variability: Measuring the evolving coronae and evidence for jet launching in AGN. *Astronomische Nachrichten*, 337(4-5):557–562.

Wilkins, D. R., Cackett, E. M., Fabian, A. C., and Reynolds, C. S. (2016). Towards modelling X-ray reverberation in AGN: Piecing together the extended corona. *Monthly Notices of the Royal Astronomical Society*, 458(1):200–225.

Wilkins, D. R. and Fabian, A. C. (2012). Understanding X-ray reflection emissivity profiles in AGN: locating the X-ray source. *Monthly Notices of the Royal Astronomical Society*, 424(2):1284–1296.

Wilkins, D. R. and Gallo, L. C. (2015a). Driving extreme variability: The evolving corona and evidence for jet launching in Markarian 335. *Monthly Notices of the Royal Astronomical Society*, 449(1):129–146.

Wilkins, D. R. and Gallo, L. C. (2015b). The Comptonisation of accretion disc X-ray emission:

Consequences for X-ray reflection and the geometry of AGN coronae. *Monthly Notices of the Royal Astronomical Society*, 448(1):703–712.

Wilkins, D. R., Kara, E., Fabian, A. C., and Gallo, L. C. (2014). Caught in the act: measuring the changes in the corona that cause the extreme variability of 1H 0707-495. *Monthly Notices of the Royal Astronomical Society*, 443(3):2746–2756.

Wu, Q. (2009). The black hole mass, Eddington ratio, and Mbh-sigma [O III] relation in young radio galaxies. *Monthly Notices of the Royal Astronomical Society*, 398(4):1905–1914.

Xu, W., Liu, Z., Gou, L., and Liu, J. (2016). X-ray fluorescent lines from the Compton-thick AGN in M51. *Monthly Notices of the Royal Astronomical Society*, 455(1):L26–L30.

Yaqoob, T., George, I. M., Kallman, T. R., Padmanabhan, U., Weaver, K. A., and Turner, T. J. (2003). Fe XXV and Fe XXVI Diagnostics of the Black Hole and Accretion Disk in Active Galaxies: Chandra Time-Resolved Spectroscopy of NGC 7314. *The Astrophysical Journal*, 596(1):85–104.

Yuan, W., Zhou, H. Y., Komossa, S., Dong, X. B., Wang, T. G., Lu, H. L., and Bai, J. M. (2008). A Population of Radio-loud Narrow Line Seyfert 1 Galaxies with Blazar-like Properties? *The Astrophysical Journal*, 685(2):801–827.

Zoghbi, A. et al. (2014). Observations of MCG-5-23-16 with Suzaku, XMM-Newton and NuSTAR: Disk tomography and Compton hump reverberation. *The Astrophysical Journal*, 789(1):56,8.

Zoghbi, A., Fabian, A. C., Uttley, P., Miniutti, G., Gallo, L. C., Reynolds, C. S., Miller, J. M., and Ponti, G. (2010). Broad iron L line and X-ray reverberation in 1H0707-495. *Monthly Notices of the Royal Astronomical Society*, 401(4):2419–2432.

Zubovas, K. and King, A. (2016). The small observed scale of AGN–driven outflows, and inside–out disc quenching. *Monthly Notices of the Royal Astronomical Society*, 462(4):4055–4066.